Universidade Estadual de Campinas
Instituto de Física "Gleb Wataghin"

Greg de Souza

Liquid Argon Scintillation with Xenon Doping: Light Yield and Waveshape Analysis with the X-ARAPUCA photon collector

Cintilação de Argônio Líquido com dopagem de xenônio: Análise de forma de onda e emissão de luz utilizando o coletor de photons X-ARAPUCA

CAMPINAS
2022

Greg de Souza

Liquid Argon Scintillation with Xenon Doping: Light Yield and Waveshape Analysis with the X-ARAPUCA photon collector

Cintilação de Argônio Líquido com dopagem de xenônio: Análise de forma de onda e emissão de luz utilizando o coletor de photons X-ARAPUCA

Dissertação apresentada ao Instituto de Física "Gleb Wataghin" da Universidade Estadual de Campinas como parte dos requisitos para a obtenção do título de Mestre em Física, na área de Física Aplicada.

Dissertation presented to the "Gleb Wataghin" Institute of Physics of the University of Campinas in partial fulfillment of the requirements for the degree of Master in Physics, in the field of Applied Physics.

Advisor/Orientador: Prof. Dr. Ettore Segreto

Este exemplar corresponde à versão final da Dissertação defendida por Greg de Souza e orientada pelo Prof. Dr. Ettore Segreto.

CAMPINAS
2022

Ficha catalográfica
Universidade Estadual de Campinas
Biblioteca do Instituto de Física Gleb Wataghin
Lucimeire de Oliveira Silva da Rocha - CRB 8/9174

So89L

Souza, Greg de, 1996-
Liquid argon scintillation with xenon doping : light yield and waveshape analysis with the X-ARAPUCA photon collector / Greg de Souza. – Campinas, SP : [s.n.], 2022.

Orientador: Ettore Segreto.
Dissertação (mestrado) – Universidade Estadual de Campinas, Instituto de Física Gleb Wataghin.

1. X-ARAPUCA. 2. Cintilação de elementos nobres. 3. Neutrinos. I. Segreto, Ettore, 1973-. II. Universidade Estadual de Campinas. Instituto de Física Gleb Wataghin. III. Título.

Informações para Biblioteca Digital

Título em outro idioma: Cintilação de argônio líquido com dopagem de xenônio : análise de forma de onda e emissão de luz utilizando o coletor de photons X-ARAPUCA
Palavras-chave em inglês:
X-ARAPUCA
Noble elements scintillation
Neutrinos
Área de concentração: Física Aplicada
Titulação: Mestre em Física
Banca examinadora:
Ettore Segreto [Orientador]
Anderson Campos Fauth
André Fabiano Steklain Lisboa
Data de defesa: 17-03-2022
Programa de Pós-Graduação: Física

Identificação e informações acadêmicas do(a) aluno(a)
- ORCID do autor: https://orcid.org/0000-0001-5446-7704
- Currículo Lattes do autor: http://lattes.cnpq.br/7980816147572388

MEMBROS DA COMISSÃO JULGADORA DA DISSERTAÇÃO DE MESTRADO DO ALUNO GREG DE SOUZA - RA 228220 APRESENTADA E APROVADA AO INSTITUTO DE FÍSICA “GLEB WATAGHIN”, DA UNIVERSIDADE ESTADUAL DE CAMPINAS, EM 17/03/2022.

COMISSÃO JULGADORA:

- Prof. Dr. Ettore Segreto (IFGW/UNICAMP) - Presidente e Orientador

- Prof. Dr. Anderson Campos Fauth (IFGW/UNICAMP)

- Dr. Andre Fabiano Steklain Lisboa (Universidade Tecnológica Federal do Paraná)

OBS.: Ata da defesa com as respectivas assinaturas dos membros encontra-se no SIGA/Sistema de Fluxo de Dissertação/Tese e na Secretaria do Programa da Unidade.

CAMPINAS

2022

Acknowledgements

I must thank the "Ministry of Science, Technology and Innovation" and the “National Council for Scientific and Technological Development – CNPq”.

Resumo

O experimento DUNE é um dos mais importantes na área de física de neutrinos, motivando a pesquisa e desenvolvimento de novas tecnologias como o coletor de luz ARAPUCA e o estudo de cintilação em elementos nobres líquidos (LNE). Esse trabalho avança o estudo da cintilação de argônio líquido (LAr) e a instrumentação para detectá-la mais eficientemente, validando as estimativas da eficiência de detecção de fótons do X-ARAPUCA Single Cell em $3.1 \pm 0.6\%$ usando dados produzidos no Lab Leptons na UNICAMP. Usando os mesmos dados também foi possível avaliar os parâmetros o modelo de cintilação de argônio líquido com quenching proposto por Segreto, 2020 [47], determinando a taxa de quenching para cintilação devido a partículas alfa para os dois mecanismos propostos: pela colisão com dímeros de argônio ionizados ($k^+ = 2.9 \pm 0.5 \times 10^{-4} ns^-1$) e pela colisão com dímeros de argônio excitados ($q = 4.0 \pm 0.5 \times 10^{-4} ns^-1$), os parâmetros foram determinados fitando o modelo proposto com formas de onda média de partículas alfa em (LAr).

O experimento protótipo do DUNE, o protoDUNE, teve um acidente que resultou na contaminação acidental do LAr com Nitrogênio (N_2)) e na degradação do sinal de luz. A dopagem de LAr com Xenônio era uma possibilidade para recuperar o sinal de luz. Esse trabalho apresenta os resultados de um teste preliminar com LAr dopado com Xenônio na Building 182 do CERN para estabelecer quando Xenônio era necessário para recuperar o sinal de luz devido à degradação pela contaminação com N_2. O experimento determinou que $10ppm$ de xenônio era suficiente para recuperar 95% da emissão de luz relativa perdida devido a contaminação de Nitrogênio similares às observadas no protoDUNE. Esse experimento também permitiu a avaliação da conversão entre luz do argônio ($127nm$) e xenônio ($174nm$) como maior que 90% para concentrações de maiores que $10ppm$ de Xenônio, a avaliação foi feita comparando dois setups de coleção de luz, com um que bloqueando a luz do argônio com uma janela de quartzo. O experimento também indicou um possível aumento na emissão de luz quando xenônio é diluído em argônio puro (sem contaminação de nitrogênio). Esses dados também permitiram avaliar a transferência de energia entre Argônio e Xenônio para cintilação de muons cósmicos $k_{Xe} = 6 \pm 2 \times 10^{-4} ns^-1$, baseado no modelo proposto por Segreto, 2020 [47] e determinado fitando a forma de onda média com o modelo para cintilação de Argônio dopado com Xenônio.

Palavras-chave: ARAPUCA; Cintilação de Elementos Nobres; Neutrino

Abstract

DUNE is one of the most important experiments in the field of neutrino physics, motivating research and development of new technologies such as the ARAPUCA photon collector and the study of Liquid Noble Element (LNE) Scintillation. This work pushes forward the study of liquid argon scintillation and of instrumentation to detect it efficiently, validating the estimation of the X-ARAPUCA Single Cell photon detection efficiency at $3.1 \pm 0.6\%$ using the data produced at Lab Leptons at UNICAMP. Using the same data it was also possible to evaluate the parameters of LAr Scintillation model with quenching proposed by Segreto, 2020 [47], determining the quenching rate for scintillation due to alpha particles for both quenching mechanisms proposed: by collision with ionized argon dimmers ($k^+ = 2.9 \pm 0.5 \times 10^{-4} ns^{-1}$) and by collision with excited argon dimmers ($q = 4.0 \pm 0.5 \times 10^{-4} ns^{-1}$), the parameters determined by fitting the proposed model with the average α waveshape in LAr.

The prototype experiment for DUNE, the protoDUNE, had an accident that resulted in accidental Nitrogen (N_2) contamination of LAr and the degradation of the light signal. Doping the contaminated LAr with Xenon was a possibility to recover the light signal. This work presents the results of a preliminary test with Xenon doped LAr at Building 182 at CERN to establish how much Xenon was necessary to recover the light degradation due to the N_2 contamination. The experiment determined that $10 ppm$ of Xenon is enough to recover 95% of the relative light yield lost due to similar levels of Nitrogen contamination seen at protoDUNE. This experiment also allowed for the evaluation of light conversion between Argon ($127 nm$) and Xenon ($174 nm$) light higher than 90% for concentrations of Xenon of $10 pmm$ or higher, this was done by comparing two different light collection set ups with one of them blocking argon light with a quartz window. It also indicated a possible light yield increase when Xenon is doped in pure LAr (no nitrogen contamination). This data also allowed for the evaluation of the energy transfer rate between Argon and Xenon for cosmic muon scintillation, based on the model proposed by Segreto,2020 [47], $k_{Xe} = 6 \pm 2 \times 10^{-4} ns^{-1}$, determined by fitting the model for Xenon doped LAr scintillation with an average waveshape.

Key-words: ARAPUCA; Noble Elements Scintillation; Neutrino Physics

Contents

Chapter 1

Neutrino Research Program

This first chapter will be dedicated to exposing the theoretical, experimental and historical context of the neutrino research program. Starting with a brief history of neutrino physics, and the basic theory behind the main phenomena of current neutrino research: Neutrino Oscillations.

Neutrino oscillations offer a window into beyond standard model physics, motivating both the exploration of new theoretical physics and the development of new experiments and experimental instrumentation.

1.1 A Brief Introduction to Neutrino Physics

The history of the neutrino as a particle starts with a controversial result in the study of beta decay. In 1914 Chadwick determined that the electron emitted in a beta decay has a continuous energy spectrum. The β decay, as proposed originally, had only two particles in the final state, as shown by eq. 1.1, which would imply a monochromatic electron spectrum,

$$ {}^{A}_{Z}X \rightarrow {}^{A}_{Z-1}Y + e. \tag{1.1} $$

The continuous nature of the electron spectrum in the β decay was topic of heated debate because it violated energy conservation. If only three bodies were involved in the decay, the energy of the electron should be determined by the energy of the nuclei before (m_1) and after (m_2) the decay (eq. 1.2):

$$ E = (\frac{m_1^2 - m_2^2 + m_e^2}{2m_1})c^2, \tag{1.2} $$

m_e is the electron mass and c is the speed of light.

Some physicists (like Bohr) did propose dropping the conservation of energy as a fundamental law in Quantum Mechanics. But the solution that actually proved itself was the proposal of a new neutral particle by Pauli in 1930[1]. This particle was eventually called the Neutrino (ν), and it was a third particle in the final state of the beta decay,

that could be written as eq. 1.3,

$$ {}^{A}_{Z}X \rightarrow {}^{A}_{Z-1}Y + e + \nu, \tag{1.3} $$

together with the work regarding the Weak Nuclear Force by Fermi, the existence of the neutrino in the beta decay was sufficient to explain the continuous electron energy spectrum seen in the *beta* decay.

In 1934, Bethe and Peierls made the first estimation of the cross section for the now called inverse beta decay (Eq. 1.4). With a very small cross section ($10^{-43} cm^2$ for a 1 MeV antineutrino), at the time there was little hope of detecting a neutrino,

$$ \bar{\nu} + p \rightarrow e^{+} + n. \tag{1.4} $$

During the following decades the understanding of particle physics changed drastically. Regarding Neutrino Physics, it's notable the discovery of the muon (μ) in 1937, that eventually resulted in the proposal of the muonic neutrino (ν_μ) as a different particle than the electronic neutrino seen in beta decay (ν_e).

Later in the twentieth century, a third neutrino flavor would be proposed, associated with the third lepton, the tau (τ), and it's associated neutrino, the tauonic neutrino (ν_τ), thus concluding the three families of leptons we see today in the Standard Model (SM) of Particles.

In 1938 the theory of stellar thermonuclear synthesis implied the production of neutrinos in stars, and the existence of a neutrino flux from the Sun of about $6.5 \cdot 10^{10}$ neutrinos per cm^2 per second.

The better understanding of neutrino physics and their production in nuclear reactors eventually led to the 1955 Reines and Cowan experiment, and the first (anti)neutrino detection [2], the schematic for the experiment is shown in figure 1.1.

The experiment used inverse beta decay to detect antineutrinos (eq. 1.4). Due to the small cross section for the interaction, a large antineutrino source was necessary, with that in mind the experiment used a nuclear reactor as the antineutrino source. A flux of $5 \times 10^{13} \bar{\nu_e}/cm^2 s$ was detected in the experiment.

The experiment used two tanks with 200L of water each as the target volume for the neutrinos to interact with. Cadmium was added to the water to scintillate when interacting with neutrons from the inverse beta decay.

When a reactor antineutrino interacted with an atom in the water tanks, the inverse beta decay produced a positron and a neutron. The positron annihilated with an electron producing a characteristic 0.5 MeV signal within $0.2 \mu sec$ from the interaction.

The neutron would be captured by the cadmium within $10 \mu sec$ of the interaction, the cadmium would than scintillate according to Eq. 1.5. The coincidence between the positron annihilation signal and the neutron capture signal was enough to establish the detection of an antineutrino through inverse beta decay,

$$ n + {}^{108}Cd \rightarrow {}^{109m}Cd \rightarrow {}^{109}Cd + \gamma. \tag{1.5} $$

While the theoretical understanding of the neutrino advanced with particle physics, the

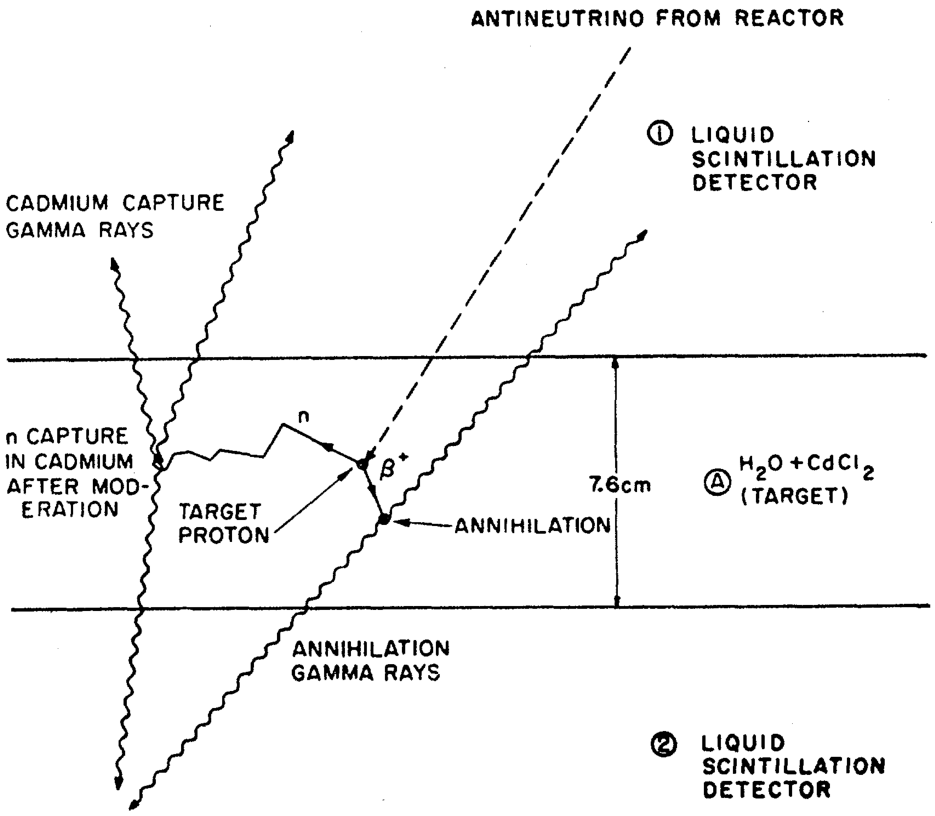

Figure 1.1: Schematic Diagram of the Reines and Cowan Antineutrino Experiment with the two coincidence signals (annihilation and n capture) [2]

next big step comes with the Homestake Solar Neutrino Experiment, headed by Raymond David and John Bacall. The detection method was based on capturing a neutrino through inverse beta decay with chloride, which would produce argon atoms (Eq. 1.6). The argon atoms could then be extracted from the chloride based active volume and used to estimate the neutrino solar flux [3],

$$\bar{\nu} + {}^{37}Cl(n) \rightarrow {}^{37}Ar(p) + e^{-}. \tag{1.6}$$

The expected neutrino flux from the Sun was 8 ± 4 captures per day in 615 tons of C_2Cl_4, the active volume. The actual rate obtained in 1968 was below 3 captures per day [4].

It's worth noting that the Homesteak experiment had a better resolution for neutrinos produced from the beryllium (^8Be) decay in the Sun, having a lower flux than neutrinos produced in other solar processes, such as p-p chains. This is due to the fact that other than the beryllium neutrinos, no other neutrinos from the sun have energy have enough to cause the inverse beta decay in equation 1.6.

The next detectors capable of looking at solar detectors were the Kamiokande II imaging water Cherenkov detector and two gallium based experiments, designed to observe neutrinos from proton-proton reactions in the Sun [5, 6, 7].

Observations of solar neutrino flux weren't consistent with the standard solar model [8, 9], but the results weren't strong enough to confirm that the anomaly was caused by

the physics of the neutrino.

One of the main explanations based on the actual physics of neutrinos was the neutrino oscillation, proposed years earlier by Pontecorvo[10] in 1957. This idea proposed that neutrinos could change flavor while travelling from the Sun to the earth, which would explain the missing neutrinos in experiments like Homesteak, that could detect only electronic neutrinos.

This would also imply that neutrinos have mass. They would be created in a pure flavor state through weak interaction, and would travel as mass eigenstates that can be written as a mix of flavor states. When detected by an experiment on earth, the flavor detected would vary according to the superposition of flavors in the mass eigenstates. The mass of the neutrino couldn't and still can't be explained by the new standard model of particles (SM), and it's the first signal of beyond SM physics ever detected.

The phenomenon of neutrino flavor conversion was confirmed in solar neutrinos by the SNO experiment [11]. [1] It employed 1kton of salt heavy water (D_2O), allowing the measurement of ν_e and $\nu_{\mu,\tau}$ separately through different interactions. The readout was made by 9456 PMTs in a 12 m radius acrylic sphere shell, at the depth of 6010m of water equivalent. The SNO experiment [11] was sensitive to both charged-current (CC, 1.7), neutral-current (NC, 1.8) and electron elastic scattering (ES, 1.9):

$$\nu_e + d \rightarrow p + p + e^-, \tag{1.7}$$

$$\nu_l + d \rightarrow p + n + \nu_l, \tag{1.8}$$

$$\nu_l + e^- \rightarrow \nu_l + e^-, \tag{1.9}$$

the CC interaction (1.7) is sensitive to only electronic neutrino ν_e flux, while the other two interactions are sensitive to any flavor (written as ν_l), but can't distinguish between them.

The SNO experiment concluded with 5σ evidence of $\nu_{\mu,\tau}$ neutrino appearance from the solar flux. Since the Sun doesn't produce this flavors, this implies $\nu_e \rightarrow \nu_{\mu,\tau}$ conversion. Additionally, the total neutrino flux agrees with the predictions from the Standard Solar Model.

The Superkamiokande II Experiment also found strong evidences of neutrino oscillations in atmospheric neutrinos [12]. The experiment could distinguish between ν_e and ν_μ. The experiment shows a noticeable disappearance of ν_μ events when comparing upward-going and downward-going muon-like events in the detector. This means that muons crossing the Earth from the Sun are missing, suggesting oscillations in the form of $\nu_\mu \rightarrow \nu_\tau$.

Since the discovery and confirmation of neutrino oscillations, it has been a topic of study in neutrino physics due to being the first confirmed beyond the standard model phenomenon observed directly.

[1] It should be noted that this was a confirmation of flavor conversion, just $\nu_e \rightarrow \nu_{\mu,\tau}$, it wasn't the confirmation of neutrino oscillations described in section 1.2.

1.2 Neutrino Oscillation Theory

The basis for our current understanding of neutrinos is the Standard Model of Particles (SM), the three flavors of neutrinos are members of the Lepton family, together with the electron, muon and tau particles. It's notable that the SM can't currently explain the origin of the neutrino mass and neutrino oscillations, what makes neutrinos a window into beyond standard model (BSM) physics

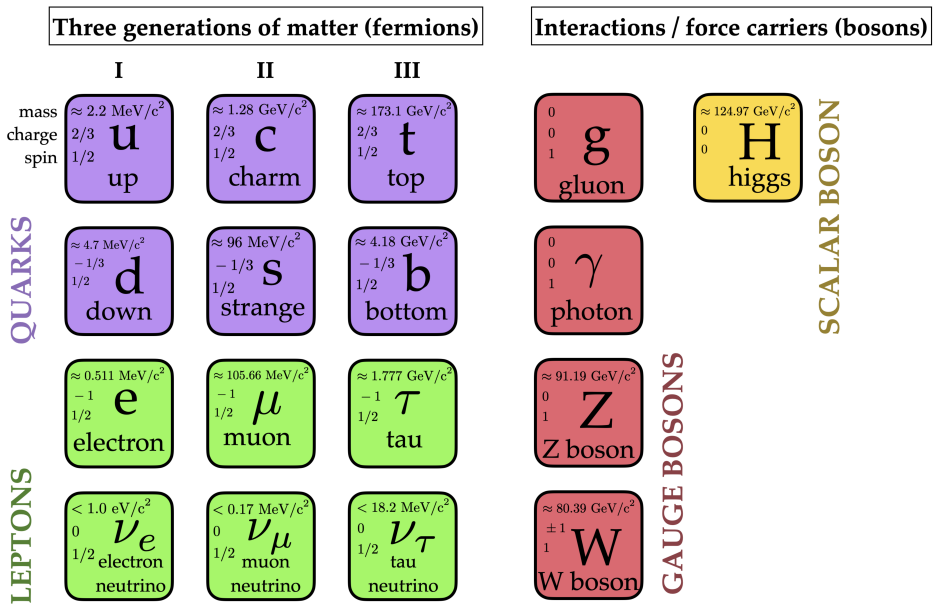

Figure 1.2: Standard Model of Particles [13]

The first scientist to propose neutrino oscillations was Pontecorvo in 1968 [10], and the phenomenon of neutrino oscillation was confirmed around the year 2000 through the observation of anomalies in neutrino flavor detection's by experiments like Superkamiokande.

It is necessary to understand neutrino oscillations to better understand the physics goals of DUNE and the current goals of neutrino research in general.

The evidence for neutrino oscillations implies that neutrinos are massive particles, and this allows for flavor mixing during propagation. Neutrinos have three mass eigenstates for neutrinos (ν_i, $i = 1, 2, 3$) and three flavor states (ν_α, $\alpha = e, \mu, \tau$), associated with the three lepton families: electron, muon and tau [14].

The mass or energy eigenstates are eigenstates for the Hamiltonian, while the three flavor eigenstates are eigenstates of the Weak Interaction. Since both have three states and are complete, the flavor states can be written in terms of the mass states as:

$$|\nu_\alpha\rangle = \sum_{k=1}^{3} U^*_{\alpha k} |\nu_k\rangle \quad (\alpha = e, \mu, \tau), \tag{1.10}$$

where $U_{\alpha k}$ is the Pontecorvo-Maki-Nakagawa-Sakata (PMNS) matrix. It's unitary by

definition:

$$U^{+}U = 1 \quad \longleftrightarrow \quad \sum_{\alpha} U^{*}_{\alpha i} U_{\alpha j} = \delta_{ij}, \tag{1.11}$$

writing the relation between mass and flavor states in matrix representation:

$$\begin{pmatrix} \nu_e \\ \nu_\mu \\ \nu_\tau \end{pmatrix} = \begin{pmatrix} U_{e,1} & U_{e,2} & U_{e,3} \\ U_{\mu,1} & U_{\mu,2} & U_{\mu,3} \\ U_{\tau,1} & U_{\tau,2} & U_{\tau,3} \end{pmatrix} \begin{pmatrix} \nu_1 \\ \nu_2 \\ \nu_3 \end{pmatrix}. \tag{1.12}$$

In order to evaluate the possible mixing of flavors while neutrinos travel, it's necessary to write the time evolution of the flavors states.

Given that mass state $|\nu_k\rangle$ is an energy eigenstates of the Hamiltonian $\mathcal{H}$, $\mathcal{H}\,|\nu_k\rangle = E_k\,|\nu_k\rangle$ where $E_k = \sqrt{(p^2 + m_k^2)}$, $(c = 1)$, is the energy, and m_k the mass of the neutrino. Since the $|\nu_k\rangle$ is an eigenstates of the Hamiltonian, it's easy to write the time evolution of these state:

$$|\nu_k(t)\rangle = e^{-iE_k t}\,|\nu_k\rangle\,, \tag{1.13}$$

the time evolution for the flavor state can be written using Eq. 1.10 in combination with Eq. 1.13:

$$|v_\alpha(t)\rangle = \sum_{k} U^{*}_{\alpha k} e^{-iE_k t}\,|v_k\rangle \quad (\alpha = e, \mu, \tau), \tag{1.14}$$

with E_k still being the energy of the mass state. Our goal is to calculate the transition probability between to flavors during propagation, $P_{\nu_\beta \to \nu_\alpha}(t) = |\,\langle \nu_\alpha(t)|\nu_\beta\rangle\,|^2$, the mass states in eq. 1.14 can be written with flavor states using $|\nu_k\rangle = \Sigma_\beta U_{\beta k}\,|\nu_\beta\rangle$. With that:

$$|\nu_\alpha(t)\rangle = \sum_{\beta = e,\mu,\tau} \Big(\sum_{k} U^{*}_{\alpha k} e^{-iE_k t} U_{\beta k}\Big)\,|v_\beta\rangle\,. \tag{1.15}$$

For $t = 0$ we have $|\nu_\alpha(0)\rangle = |\nu_\alpha\rangle$ through unitarity of the PMNS matrix. The transition amplitude between two arbitrary flavors (α , β) can be written using 1.15:

$$A_{\nu_\alpha \to \nu_\beta}(t) \equiv \langle \nu_\beta | \nu_\alpha(t)\rangle = \sum_{k} U^{*}_{\alpha k} U_{\beta k} e^{-iE_k t}, \tag{1.16}$$

and the transition probability as it's absolute square:

$$P_{\nu_\alpha \to \nu_\beta}(t) \equiv |A_{\nu_\alpha \to \nu_\beta}(t)|^2 = \sum_{kj} U^{*}_{\alpha k} U_{\beta k} U_{\alpha j} U^{*}_{\beta j} e^{-i(E_k - E_j)t}. \tag{1.17}$$

Equation 1.17 gives the probability oscillation between two arbitrary neutrino flavors

relies on the values of the PMNS matrix that are determined experimentally, and the energy difference between eigenstates, thus oscillations can't be use to measure the mass of the neutrino, only their mass differences. And, at last, it depends on the travel time, that is usually rewritten in term of the length travelled.

Eq. 1.17 is usually written in the ultrarelativisc limit, with $t = L/c$, with $c = 1$. In this limit $E \approx p >> m$, resulting in the energy of the neutrino written as:

$$E_k = p\sqrt{1 + \frac{m_k^2}{p^2}} \approx E(1 + \frac{m_k^2}{2E^2}),$$

with that the energy difference can be written in terms of the mass difference:

$$E_i - E_j = E + \frac{m_i^2}{2E^2} - E + \frac{m_j^2}{2E^2} = \frac{\Delta m_{ij}^2}{2E^2}, \tag{1.18}$$

with $\Delta m_{ij}^2 = m_i^2 - m_j^2$. Combining this with eq. 1.17 results in the usual form of the flavor oscillation equation, written in terms of the mass difference and the length travelled:

$$P_{\nu_\alpha \to \nu_\beta}(t) \equiv |A_{\nu_\alpha \to \nu_\beta}(t)|^2 = \sum_{kj} U_{\alpha k}^* U_{\beta k} U_{\alpha j} U_{\beta j}^* e^{-i(\Delta m_{kj}^2)L/2E}. \tag{1.19}$$

The equation 1.19 is the usual form to express the probability transition between neutrinos during their propagation, it can be averaged to account for energy resolution and other experimental factors, and it still applies to any number of neutrinos, it is just necessary to add new flavors and masses accordingly.

1.2.1 Two Flavors Scenarios

While eq. 1.19 is a general equation for the oscillation probability, the computations for three neutrinos can be a bit technical. The two flavors neutrino scenario is a simplified case that gives a simpler but still effective demonstration of how to calculate the probabilities accordingly and using equation 1.19 [15, 14].

So, we'll assume only two massive neutrinos coupled with two flavor eigenstates. In this scenario, the oscillation will only happen between two flavors, say α and β. Each flavor can be written as a superposition of the mass eigenstates ν_1 and ν_2 in similar fashion to eq. 1.12:

$$\begin{pmatrix} \nu_\alpha \\ \nu_\beta \end{pmatrix} = \begin{pmatrix} U_{\alpha,1} & U_{\alpha,2} \\ U_{\beta,1} & U_{\beta,2} \end{pmatrix} \begin{pmatrix} \nu_1 \\ \nu_2 \end{pmatrix} = \begin{pmatrix} cos(\theta) & sin(\theta) \\ -sin(\theta) & cos(\theta) \end{pmatrix} \begin{pmatrix} \nu_1 \\ \nu_2 \end{pmatrix}. \tag{1.20}$$

The unitary PMNS Matrices ($U_{\gamma i}$) was written in terms of the mixing angle θ, where $0 \leq \theta \leq \pi/2$. The unitarity is satisfied $U^+U = cos^2(\theta) + sin^2(\theta) = 1$. Now it's simple compute the oscillation probability according to eq. 1.19. Assuming that ν_1 is the lightest neutrino so that $\Delta m_{21}^2 > 0$. Also, it's easy to see that $\Delta m_{11}^2 = \Delta m_{22}^2 = 0$, so the

exponential terms in when k=j at the summation is 1, the transition probability is:

$$P_{\nu_\alpha \to \nu_\beta}(L,E) = U^*_{\alpha 1}U_{\beta 1}U_{\alpha 1}U^*_{\beta 1}exp(0) + U^*_{\alpha 2}U_{\beta 2}U_{\alpha 1}U^*_{\beta 1}exp(-i\frac{\Delta m^2_{21}L}{2E}) + U^*_{\alpha 1}U_{\beta 1}U_{\alpha 2}U^*_{\beta 2}exp(i\frac{\Delta m^2_{21}L}{2E})) + U^*_{\alpha 2}U_{\beta 2}U_{\alpha 2}U^*_{\beta 2}exp(0), \tag{1.21}$$

simplifying with the fact that the matrix is real case, and both exponential add up to a cosine ($e^{ix} + e^{-ix} = 2cos(x)$):

$$P_{\nu_\alpha \to \nu_\beta}(L,E) = |U_{\alpha 1}|^2|U_{\beta 1}|^2|U_{\alpha 2}|^2|U_{\beta 2}|^2 + 2U_{\alpha 1}U_{\alpha 2}U_{\beta 1}U_{\beta 2}cos(\frac{\Delta m^2_{21}L}{2E}), \tag{1.22}$$

$|U_{\gamma i}|$ is the absolute value of the element γi of the matrix in equation 1.20.Using the expression of the matrix as in equation 1.20:

$$P_{\nu_\alpha \to \nu_\beta}(L,E) = 2cos^2(\theta)sin^2(\theta)(1 - cos(\Delta m^2_{21}\frac{L}{2E})). \tag{1.23}$$

It's common to rewrite this expression using the trigonometrical properties $sin(2x) = 2cos(x)sin(x)$ and $cos(2x) = 1 - sin^2(x)$:

$$P_{\nu_\alpha \to \nu_\beta}(L,E) = sin^2(2\theta)sin^2(\Delta m^2_{21}\frac{L}{4E}) \tag{1.24}$$

or

$$P_{\nu_\alpha \to \nu_\beta}(L,E) = \frac{1}{2}sin^2(2\theta)\left(1 - cos(\Delta m^2_{21}\frac{L}{2E})\right). \tag{1.25}$$

Since we have only two neutrinos, it either oscillate changing flavor, or it survives, so the survival probability is simply:

$$P_{\nu_\alpha \to \nu_\alpha}(L,E) = 1 - P_{\nu_\alpha \to \nu_\beta}(L,E) = 1 - sin^2(2\theta)sin^2(\Delta m^2\frac{L}{4E}). \tag{1.26}$$

1.2.2 Three Flavors Scenario

The three flavor scenario is very similar to the two flavor scenario, and the same ideas are used as the basis. The PMNS matrix can be represented in terms of mixing angles and a global complex phase [15, 14]. For the three flavor scenario the PMNS matrix can

be written as:

$$U = \begin{pmatrix} 1 & 0 & 0 \\ 0 & cos\theta_{23} & sin\theta_{23} \\ 0 & -sin\theta_{23} & cos\theta_{23} \end{pmatrix} \begin{pmatrix} cos\theta_{13} & 0 & sin\theta_{23} \cdot e^{-i\delta} \\ 0 & 1 & 0 \\ -sin\theta_{23} \cdot e^{i\delta} & 0 & cos\theta_{13} \end{pmatrix} \begin{pmatrix} cos\theta_{12} & sin\theta_{12} & 0 \\ -sin\theta_{12} & cos\theta_{12} & 0 \\ 0 & 0 & 1 \end{pmatrix}. \tag{1.27}$$

The matrix can be written as a single matrix instead, for that it's usual to write $cos\theta_{ij} = c_{ij}$ and $sin\theta_{ij} = s_{ij}$:

$$U = \begin{pmatrix} U_{e,1} & U_{e,2} & U_{e,3} \\ U_{\mu,1} & U_{\mu,2} & U_{\mu,3} \\ U_{\tau,1} & U_{\tau,2} & U_{\tau,3} \end{pmatrix} = \begin{pmatrix} c_{12}c_{13} & s_{12}c_{13} & s_{13}e^{-i\delta} \\ -s_{12}c_{23} - c_{12}s_{23}s_{13}e^{i\delta} & c_{12}c_{23} - s_{12}s_{23}s_{13}e^{i\delta} & s_{13}e^{-i\delta} \\ s_{12}s_{23} - c_{12}s_{23}s_{13}e^{i\delta} & -c_{12}s_{23} - s_{12}c_{23}s_{13}e^{i\delta} & c_{23}c_{13} \end{pmatrix}. \tag{1.28}$$

The results of experiments and plots regarding neutrinos are usually expressed in terms of the mixing angles or their sines and cosines. It's also possible to write a oscillation probability in a form similar to equation 1.24 [14]:

$$\begin{aligned} P_{\nu_\alpha \to \nu_\beta}(L,E) =& \delta_{\alpha\beta} - 4 \sum_{k>j,j} Re\{U^*_{\alpha k} U_{\beta k} U_{\alpha k} U^*_{\beta j}\} sin^2(\Delta m^2_{kj} \frac{L}{4E}) \\ &+ 2 \sum_{k>j,j} Re\{U^*_{\alpha k} U_{\beta k} U_{\alpha k} U^*_{\beta j}\} sin(\Delta m^2_{kj} \frac{L}{2E}), \end{aligned} \tag{1.29}$$

with the survival probability as:

$$P_{\nu_\alpha \to \nu_\alpha}(L,E) = 1 - 4 \sum_{k>j,j} |U_{\alpha k}|^2 |U_{\alpha j}|^2 sin^2(\Delta m^2_{kj} \frac{L}{4E}). \tag{1.30}$$

1.3 Current topics in Neutrino and related research

1.3.1 Absolute Mass and Mass Hierarchy

Neutrino research is a important topic in modern particle physics, it presents evidence of beyond SM physics, and many of the fundamental physical properties of the neutrinos aren't yet clear. As an example, the absolute scale of the neutrino mass has not yet been determined, the best we currently have is an upper bound for the neutrino masses as 1.1 eV as determined by the KATRIN experiment [16]. The origin of the neutrino mass is also not currently explained by the Standard Model of Particles.

Another uncertainty regarding the neutrino mass is the neutrino mass ordering, mainly if the mass difference Δm^2_{32} is positive or negative. If $\Delta m^2_{32} > 0$ we have what is called normal mass ordering ($m_3 > m_2 > m_1$), and if $\Delta m^2_{32} < 0$ we have the inverted mass ordering ($m_2 > m_1 > m_3$). The mass ordering can be determined from neutrino oscillations, and the DUNE experiment plans to do so [17].

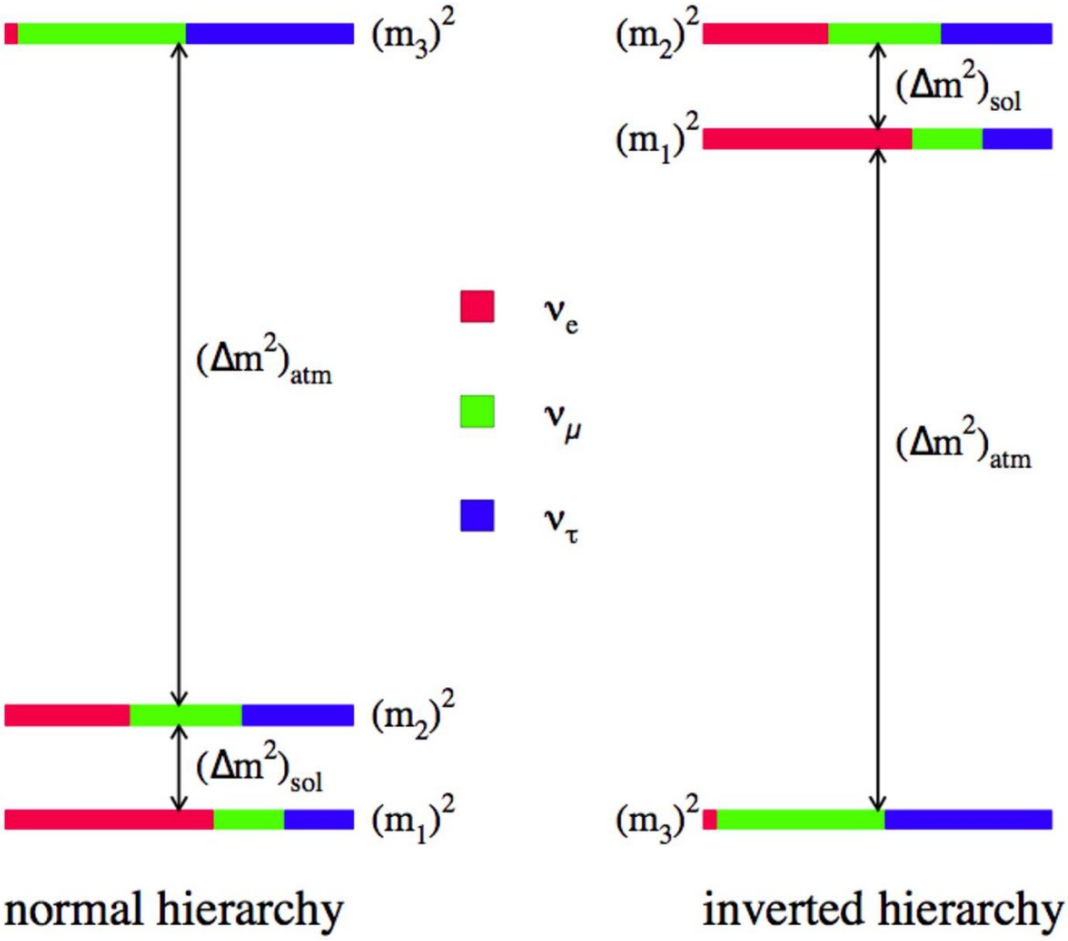

Figure 1.3: The two possible neutrino mass hierarchies. The difference mass difference Δ_{21} was determined from solar neutrinos, and the absolute value of mass difference Δ_{31} was determined with atmospheric neutrinos, the sign of the mass difference Δ_{31} is still undetermined.

1.3.2 CP Violation and Matter Antimatter Asymetry

The oscillation and survival probabilities for antineutrinos can be calculated in a similar way as presented for equations 1.29 and 1.30 for the neutrino. We start from the analogous of Eq. 1.10:

$$|\bar{\nu_\alpha}\rangle = \sum_{k=1}^{3} U^*_{\alpha k} |\bar{\nu_k}\rangle \quad (\alpha = e, \mu, \tau), \tag{1.31}$$

for the antineutrinos. For the two neutrino scenario, the oscillation probability is written as:

$$P_{\bar{\nu_\alpha}\to\bar{\nu_\beta}}(t) = \sum_{kj} U_{\alpha k} U^*_{\beta k} U^*_{\alpha j} U^*_{\beta j} e^{-i(\Delta m^2_{kj})L/2E}. \tag{1.32}$$

And for the three neutrino scenario [14]:

$$\begin{aligned} P_{\bar{\nu_\alpha}\to\bar{\nu_\beta}}(L,E) =& \delta_{\alpha\beta} - 4\sum_{k>j,j} Re\{U^*_{\alpha k}U_{\beta k}U_{\alpha k}U^*_{\beta j}\} sin^2(\Delta m^2_{kj}\frac{L}{4E}) \\ & - 2\sum_{k>j,j} Re\{U^*_{\alpha k}U_{\beta k}U_{\alpha k}U^*_{\beta j}\} sin(\Delta m^2_{kj}\frac{L}{2E}), \end{aligned} \tag{1.33}$$

The only difference between equations 1.29 and 1.33 is the signal on the last term. This means that there is a difference between the transition probability between neutrinos and antineutrinos. This is a violation of the Charge and Parity Transformation (CP), the CP transformation is a inversion of charge and parity of particles, turning particles into antiparticles and antiparticles into particles. A CP symmetry violation implies that the behavior of particles and antiparticles are different.

The phase ($\delta \equiv \delta_{CP}$) in Eq. 1.27 is responsible for that difference, if δ is different than 0, π or 2π. The difference between equations 1.29 and 1.33 can be written as [18]:

$$\Delta P \equiv P(\nu_\alpha \to \nu_\beta) - P(\bar{\nu_\alpha} \to \bar{\nu_\beta}) = -16 J_{\alpha\beta} sin\Delta m^2_{12} sin\Delta m^2_{23} sin\Delta m^2_{31}, \tag{1.34}$$

with $J_{\alpha\beta}$ written as:

$$J_{\alpha\beta} \equiv Im(U_{\alpha 1}U^*_\alpha U^*_{\beta 2}U_{\beta 2}) = \pm J \quad J \equiv s_{12}c_{12}s_{23}c_{23}s_{13}c^2_{13}sin\delta_{CP}. \tag{1.35}$$

Both of these equations (Eq. 1.34 and 1.35) make clear the relation of the complex phase in Eq. 1.27 and the CP violation in neutrino oscillations.

The neutrino oscillation CP violation is an interesting phenomenon that can help explain open questions in other areas of particle physics. Mainly, CP violation in general is interesting for the research regarding matter-antimatter asymmetry.

The current Big Bang Model describes the current structure of the universe based on the state of the universe soon after it's beginning. According to our current understanding of matter and antimatter, they should have annihilated completely, leaving only radiation behind. An universe full of matter such as we see today would be impossible if that were the case.

Something has to have caused the asymmetry between matter and antimatter, favoring the creation of matter (or baryons), this is known as *baryogenesis*. According to A. Sakharov [19], three conditions are necessary to explain the asymmetry:

- Interactions out of thermal equilibrium,
- CP violation, and
- Baryon number violation

This conditions are know as the *Sakharov Conditions*.

Measuring and understanding these conditions is part of the current research program in particle physics, and the neutrino CP violation would be the first evidence of CP violation in the leptonic sector.

Not only that, it's not uncommon for neutrino experiments to be designed to also probe the possibility of proton decay, that would be an example of Baryon number violation. The Super-Kamiokande [20] Experiment has the capability to explore the possibility of proton decay, and so will the DUNE experiment [17].

1.4 Deep Underground Neutrino Experiment

The Deep Underground Neutrino Experiment (DUNE [17, 21, 22, 23]) will be a large Neutrino experiment hosted by Fermilab in the Long-Baseline Neutrino Facility (LBNF), containing the most intense neutrino beam in the world, a near detector 515 meters from the beam source, and far detector with 40kt of active volume in 4 liquid argon time projection chamber (LArTPC). The dedicated neutrino beam will trigger the data collection in the near and far detectors.

The DUNE near detector (DUNE ND)[24] has three primary detector components with a total of 150 ton active volume, the detector components can be moved on and off axis from the beamline. The near detector will provide high statistics characterization of the beam and it's spectrum. The beam, combined with the data collected by the near and far detector, will allow for comprehensive science program (subsection 1.4.1).

The far detector will be installed in the Sanford Underground Research Facility (SURF) in South Dakota, 1300km away from the beam source, at Fermilab. This distance was selected based partly on the material needs for building a large detector, but it's in the scale that will allow for the study of ν_e appearance in ν_μ and $\bar{\nu_\mu}$ beams produced by the dedicated beam at Fermilab. The beam will be calibrated using a near detector in the Fermilab cite.

The DUNE Far Detector consists of four modular 10kt LArTPCs, with a total of 40kt of fiducial mass. Each module will have dimensions of $14m \times 14.1m \times 62m$, and they'll be shoot with a neutrino bean from a 80GeV primary proton beam, with beam power up to 1.2MW.

DUNE is planning on using two different types of time projection chambers for it's four modules (two for each type):

- The single-phase (SP) LArTPC [21] has that name because it uses only argon in liquid form as an active volume. Particle interactions inside the detector will produce light and free charges in the active volume, that will be collect by a Photon Detection (PD system) and an charge readout system. Similar Single-Phase LArTPCs have been used in plenty of others experiments like ICARUS, MicroBooNE, SBND and LArIAT.

- The Vertical Drift TPC [23] is a novelty in LArTPC design, with a design that is easier to assemble than the previous TPCs designs. The TPC chamber will be filled with liquid and gaseous argon. The gaseous phase will occupy the top half of the

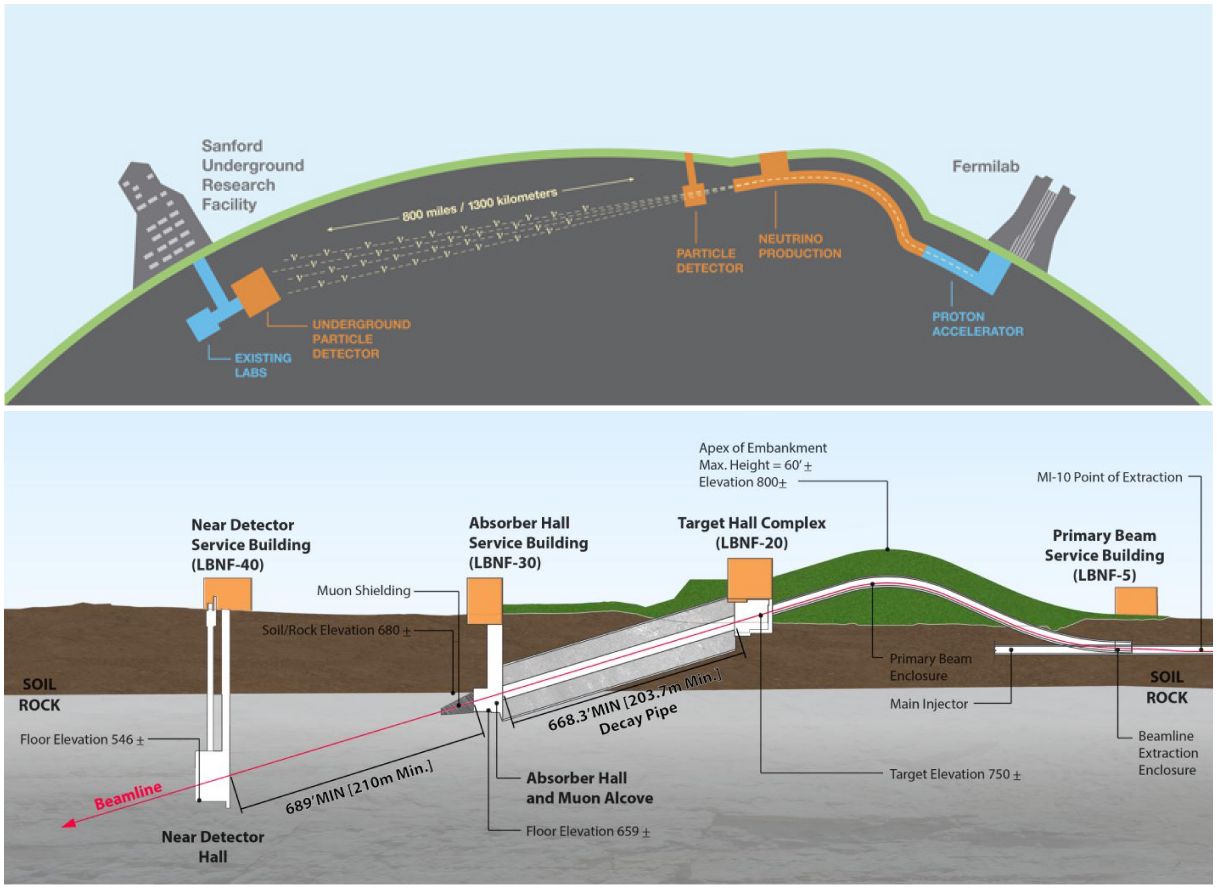

Figure 1.4: (Top) Concept for the neutrino beam directed at the farm detector (Schematic). (Bottom) Working Scheme for DUNE's near detector

chamber, with the liquid phase on the bottom. Both phases will be divided by the Large Electron Multiplier. The electrons produced in the Vertical Drift TPC will drift upwards, crossing the Large Electron Multiplier that will amplify the charge signal when it crosses from the liquid portion to the gaseous portion.

1.4.1 DUNE Scientific Goals

The DUNE scientific program is comprehensive, and will tackle plenty of open questions in modern day particle physics. It's scientific goals are divided into their primary science programs, that addresses key questions in particle physics and direct the DUNE design.

Beyond that, there is also an extensive ancillary program, regarding other scientific research that can be produced from the experiment as a whole.

DUNE's primary science program consists of:

- Determining the charge-parity violating phase δ_{CP} (Eq. 1.34). A value different from 0 or π would represent the discovery of CP violation in the leptonic sector, and help explain matter-antimatter asymmetry in the universe.

- Determine the neutrino mass ordering, that is, measure if the mass difference $\Delta m^2_{31} = m^2_3 - m^2_1$ is negative or positive.

- Precise measurement of the mixing angle θ_{23} and it's octant through studies of muon neutrino disappearance and electron neutrino appearance in both ν_μ and $\bar{\nu_\mu}$ beams.
- Search for important modes of proton decay. This would be ground breaking, and could provide a portal for a Grand Unification Theories.
- Detection and measurement of supernova neutrinos (ν_e flux), if one should occur in our galaxy during the lifetime of the DUNE experiment.

These are the main goals in the DUNE research project, and the main objectives behind the technological needs of the experiment.

There is also an extensive ancillary science program in the DUNE experiment, It includes general accelerator-based neutrino research, in search for beyond standard model (BSM) physics such as non-standard interactions, CPT violation, the search for sterile neutrinos ...

Beyond accelerator neutrinos, the DUNE experiment will also be able to measure and study the oscillation of atmospheric neutrinos, search for signatures of dark matter, and allow for a rich neutrino interaction physics program in the near detector, including measurements of neutrino cross sections and other nuclear effects.

Chapter 2

Time Projection Chamber, Liquid Argon Scintillation and the ARAPUCA Module

The liquid argon time projection chamber (LArTPC) is a detector proposed by Carlo Rubbia in 1977 [25]. It's a detector that combines the high resolution of bubble chambers with massive target volumes.

The DUNE experiment will consist of four time projection chamber (TPC), two single-phase LArTPC using only liquid argon, and two dual-phase TPC, that combines liquid and gaseous argon.

The single-phase LArTPC is the one of interest in this chapter, in which the working principle of the TPC will be explained, as well with the choice of Liquid Argon as active volume.

In the second section the technology behind the Photon Detection System for the two DUNE Single-Phase LArTPCs will be explained, as well as it's light detector, the ARAPUCA light collector (and it's current iteration as the X-ARAPUCA)

2.1 LArTPC Operation Principle

The goal of the LArTPC is to reconstruct a 3D track of an ionizing particle crossing it's active volume. The active medium is high purity liquid argon.

When a charged particle, like a cosmic muon or a positron generated by inverse beta decay, crosses the active volume of liquid argon (LAr) in the TPC, it deposits energy by linear energy transfer (LET), and leaves a track of ionized argon atoms and electrons. This electrons are used to create the shape of the track. That is done by applying a strong and uniform electric field across the LAr volume, separating the electrons from the Ar ions. This electrons are collected by an anode grid composed of multiple wire planes (three in the case of DUNE). A diagram of the LArTPC technology is shown in figure 2.2

The wire planes are angled in different directions, each plane of wire plains can be used to create a 2D reconstruction of the track, with three planes we have up to 3 different 2D reconstructions that can be used to get information about the 3D shape of the track.

Electron ion pairs are not the only result of a particle depositing energy into LAr, liquid argon is an excellent scintillator, emitting vacuum ultraviolet (VUV) light in a $10nm$ band around $127nm$ in wavelength. This emission is the result of de-excitation of argon molecules [26, 27]. This excited particles of Argon are formed when ionizing radiation crosses the LAr volume. The excitation and scintillation can happen in two ways.

The first one is direct excitation, where the energy is deposited by creating an excited argon atom, that combines with another argon atom to form an excited argon dimer, that decays emitting light:

$$Ar + Ar^* \rightarrow Ar_2^* \rightarrow 2Ar + \gamma(127nm). \tag{2.1}$$

The second mechanism for scintillation happens when an ionized argon particle, created by the ionizing radiation crossing the detector, combines with another argon to form a ionized argon dimer, this ionized dimer can recombine with an electron to form an excited argon dimer, that decays emitting light:

$$Ar \rightarrow Ar^+ + e^- \rightarrow Ar_2^+ + e^- \xrightarrow{\text{recomb.}} Ar_2^* \rightarrow 2Ar + \gamma(127nm) \tag{2.2}$$

These are the two signals produced by the LAr active volume in a TPC: the charge signal from ionization and electron drift, and the scintillation that can be produced according to equations 2.1 and 2.2. The values for Scintillation Yield and linear energy deposition (LET) are shown in table 2.1.

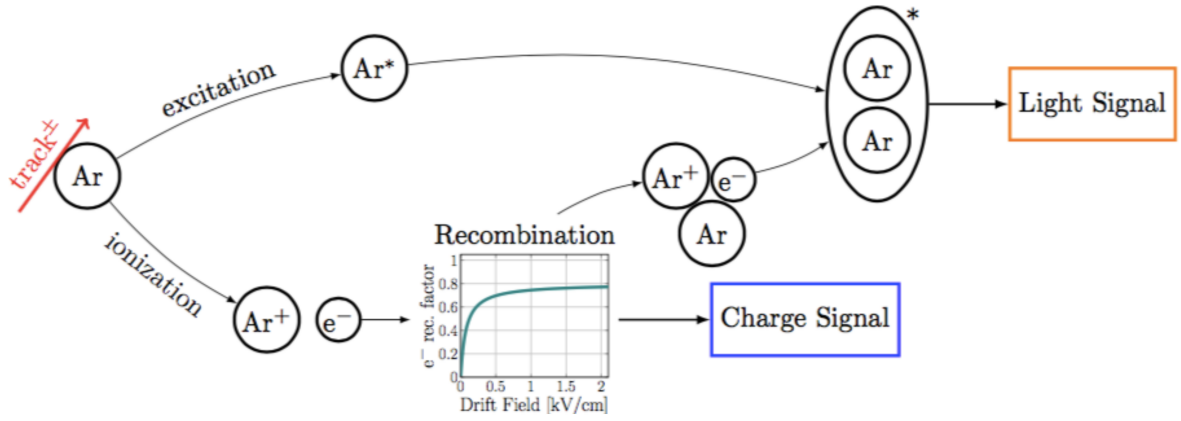

Figure 2.1: Schematic for the electron and light signal in LArTPCs. Notably the light and charge signal compete in the ionization path. Higher electric fields increase the amounts of charge and decrease the light yield by making recombination less likely. [21]

A charge signal from electron drift can take milliseconds to cross the active volume, the radiation length in argon is of $14cm$. The scintillation photons are faster, arriving at the Photon Detection (PD) system in nanoseconds, liquid argon has a refractive index of $n = 1.2$. So it's possible to use the scintillation flash to determine the absolute time scale of an event in the detector. It also allows for reconstruction in the drift direction.

With the combination of the charge and light signal, it's possible to reconstruct the

full 3D geometry of the track, it's initial time (t_0) and position inside the detector, as shown in figure 2.2.

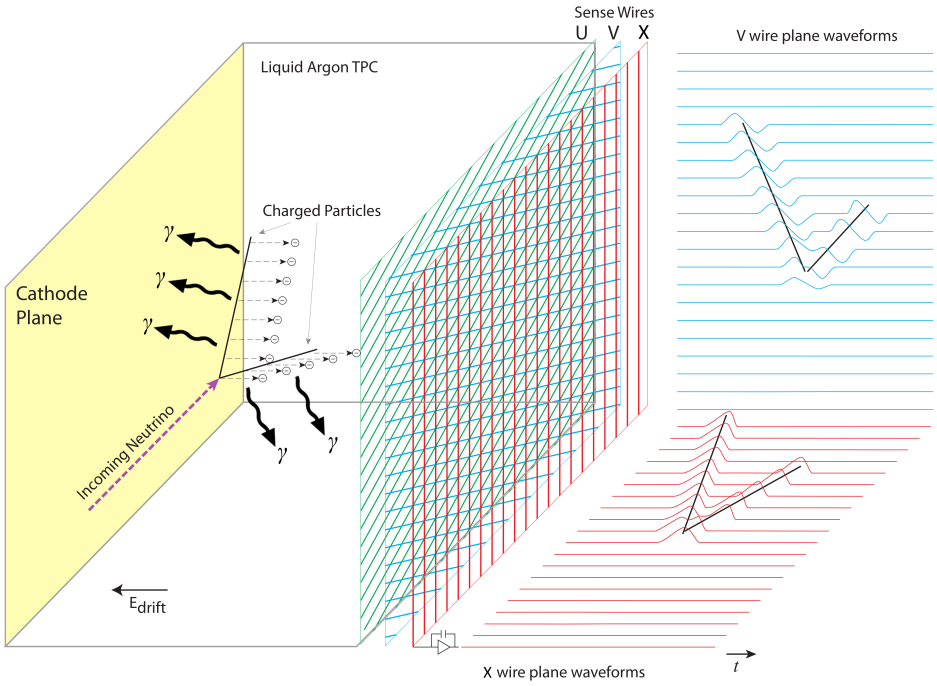

Figure 2.2: Representation of single-phase TPC working principle with both light and electron signals [22]. The wire planes with different orientations make possible to reconstruct the topology of the track, and in combination with the light signal allow for full spacial and temporal reconstruction of the event.

It must be noted that the recombination in the scintillation signal and the electron drift in the charge signal are competing effects, electrons that recombined can't drift. Taking into account the electric field, the stronger the field, less probable is the recombination process. An experimental value of $500V/cm$ has been reached as a compromise between both processes [28].

Another important topic regarding the working principles of a Single Phase LArTPC is understanding why Liquid Argon is the active volume. In the context of neutrino physics, it's important to have enough target mass to increase neutrino interaction probability. So an experiment will need significant amounts of any active medium of choice.

With the goal of collecting electrons created by ionizing radiation in the medium, it is necessary a target volume with high electron mobility, that is electropositive (so that electrons won't be captured), and a high radiation length (electrons won't lose too much energy by bremsstrahlung). Most liquid noble gases have this properties, so they are all candidates for the active mass of a similar detector.

In particular, Helium and Neon have low electron mobility, so the drift distances wouldn't be enough for a large TPC, and their scintillation wavelengths are too small for detection.

Krypton has good properties, but low abundance in nature. Liquid Xenon similarly is a viable candidate, but producing liquid Xenon is significantly more expensive than

Table 2.1: Relevant properties of LNE, water included as reference [29, 30, 31, 32, 33].

	He	Ne	**Ar**	Kr	Xe	Water
Boiling Point (K, 1atm)	4.2	27.1	**87.3**	120.0	165.0	373
Density (g/cm^3)	0.125	1.2	**1.4**	2.4	3.0	1.0
Radiation Length (cm)	755.2	24.0	**14.0**	4.9	2.8	36.1
dE/dx (MeV/cm)	0.24	1.4	**2.1**	3.0	3.8	1.9
Scintillation Yield (γ/MeV)	19000	30 000	**51 300**	25 000	42 000	-
Scintillation λ	80	78	**128**	150	175	-

Liquid Argon.

Liquid argon has a high density, a good radiation length and good scintillation yields, it's also relatively abundant and cheap. Making it a viable candidate for any large TPC endeavour.

Another concern of any large LArTPC experiment is the effect of contamination. Both the amount of charge collected and scintillation yield are highly sensitive to contaminants. Electronegative contaminants such as oxygen or water absorb ionized electrons during the drift, and nitrogen contaminants quench the scintillation of LAr, decreasing the quality of signals. For an experiment like the DUNE far detector, a purity of 100 ppt (parts per trillion) O_2-equivalent is necessary to ensure a electron lifetime greater than 3ms [22].

2.2 Photon Detection in LArTPC

Photon detection will be an essential subsystem of the DUNE Single-Phase TPC, especially for the science objectives that can't be correlated with the timing signal from the neutrino source at Fermilab, such as the search for proton decay, supernova neutrino bursts (SNB), and the ancillary science program regarding atmospheric neutrinos.

The timing information provided by the photon detector (PD) and TPC systems allows for determination of drift time of ionizing particles, that, in turn, allows localization of the events inside the active volume, providing the ability to correct the measured charge for effects associated with drift path length, purity of LAr, or non-uniformity in the detector. This is important for the reconstruction of the energy deposited by an ionizing event.

The DUNE PD system has both scientific and technical requirements for it's design. The performance required to achieve the primary scientific objectives is the detection of sufficient light for timing and measurement of total energy in $> 200MeV$ events, and sufficient light to provide time measurement of $< 200MeV$ events, detect sufficient light from $10MeV$ events to provide a energy measurement with resolution of 10%, and record time and signal amplitude with sufficient precision to achieve key physics parameters [21].

Apart from the scientific requirements, there is a strict size limit due to the fact that the PD system will be placed between the electronic readout system. This exclude the use of traditional large area photo-multiplier tubes (PMT) [22] because their dimensions are too large to fit the DUNE TPC design.

2.2.1 The ARAPUCA Photon Collector

Currently, the main module for Photon Detection in DUNE is the ARAPUCA Photon Collector, there are currently two different designs: the S-ARAPUCA and X-ARAPUCA. Using a new scalable concept, they provide a better performance than alternative approaches given the size constrains in DUNE-like TPCs [22].

The main idea behind the S-ARAPUCA photon-collector is to trap photons inside a box with highly reflective internal surfaces and a Silicon Photo-multiplier (SiPM). This effectively increases the detection are of the SiPM inside the S-ARAPUCA [34]. The inside of the S-ARAPUCA box will be covered of the highly reflective acrylic foil 3M-VIKUITI ESR.

The other important part of the S-ARAPUCA is the use of a short-pass dichroic optical filter that is highly transparent to photons with a tunable cut-off while being almost perfectly reflective to wavelengths above the cut-off.

The two faces of the dichroic filter (S1 and S2 in figure 2.4) are covered with two different wavelength shifters (WLS) with emission wavelengths L1 and L2, such that $L1 < L_{\text{cut-off}} < L_2$, where $L_{\text{cut-off}}$ is the cut-off of the dichroic filter in the middle. The cut-off wavelength is the middle of the region of full transparency ($> 95\%$) and full reflectivity ($> 98\%$).

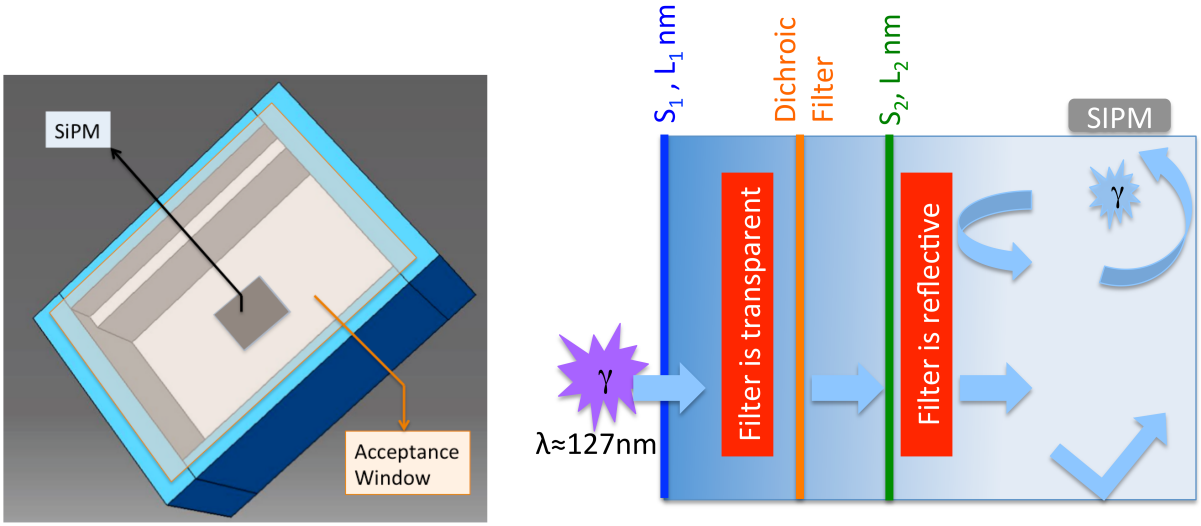

Figure 2.3: Left: graphic representation of the ARAPUCA, with the reflective surfaces in blue, the transparent dichroic window and the SiPM. Right: operating principle with the ARAPUCA [34].

As an example, consider the S-ARAPUCA module looking at a LAr active volume, with emission of VUV light with a $10nm$ band around $127nm$. For the first layer of wavelength shifter, on the outside of the dichroic filter, P-Terphenhyl can be used (emission at $350nm$), and for the inside window TPB (emission at $430nm$) can be used.

Using a dichroic filter with a cut-off around $400nm$ one can trap a LAr scintillation photon inside the ARAPUCA box to be detected by the SiPM. A comparison between the emission of the wavelength shifters and the transmissivity and reflectivity of the dichroic

filter is shown in figure 2.4. Tests with the S-ARAPUCA design concept have measured it's efficiency around $1.15\% \pm 0.15\%$, with an increase of the effective are of the SiPM by 4 times [35]. For reference, the minimum light detection efficiency necessary for the DUNE scientific goals (subsection 1.4.1) is of 1%, and the previous DUNE light collection modules proposed don't achieve this minimum collection efficiency.

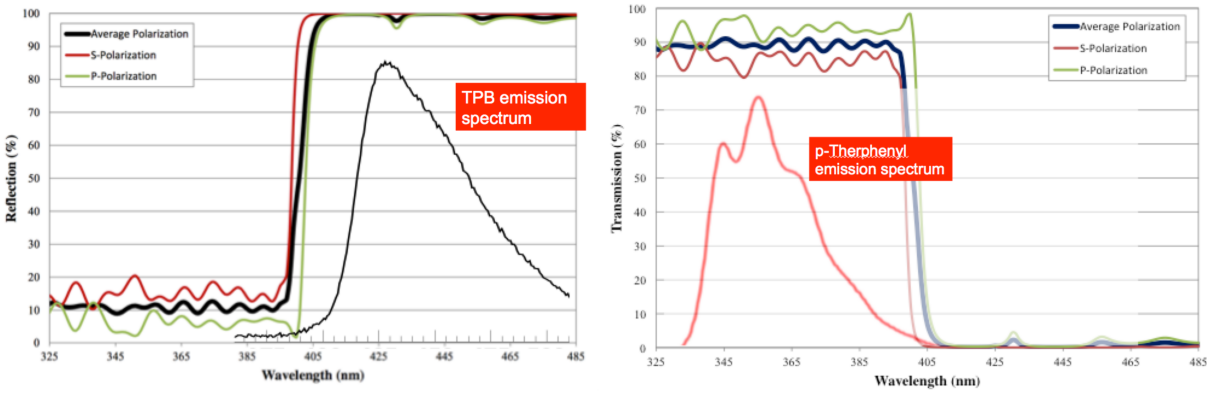

Figure 2.4: Left: TPB emission spectrum over the reflectivity of the short-pass dichroic filter. Right: p-Therphenyl emission spectrum over the transmissivity of the short-pass dichroic filter [34].

The second ARAPUCA concept is the X-ARAPUCA, that combines the S-ARAPUCA design with light guides [36]. It still uses the trapping principle of the S-ARAPUCA box, but the inner wavelength shifter is substituted by an acrylic light guide slab which has the wavelength shifter embedded on it. The active photo-sensors are optically coupled to one or more sides of the slab.

This adds new ways for the photons to be directed to the photon-sensor inside. It can happen in the usual way as in the S-ARAPUCA, where the photon is reflected on the walls until detected, but it can also suffer total reflection in the slab, being guided to the slab that way. The total reflection can happen both inside the slab, or between the slab and the dichroic filter. The efficiency of the X-ARAPUCA design has been measured up to $2.9\% \pm 0.1\%$ [37], depending on the components used. The X-ARAPUCA is a photon collector that fits the size required by the design, has a time resolution of few nanoseconds allowing for precise determination of trigger time, and has a higher photon collection efficiency than required by the DUNE primary scientific goals, making it a suitable photon collector for the DUNE TPCs and similar experiments.

Photon Detection for neutrino research is not the only situation in which the ARAPUCA module could be applied. Other areas of particle physics research are looking to use Liquid Noble Elements (LNE) as active volumes in large experiments (tons of LNE), and as a consequence they need to cover larger areas with photon-detectors. Notably detectors like this are important for dark matter research. The ARAPUCA device could be a way to increase the coverage to detect photons with high efficiency while reducing the number of photo-sensors.

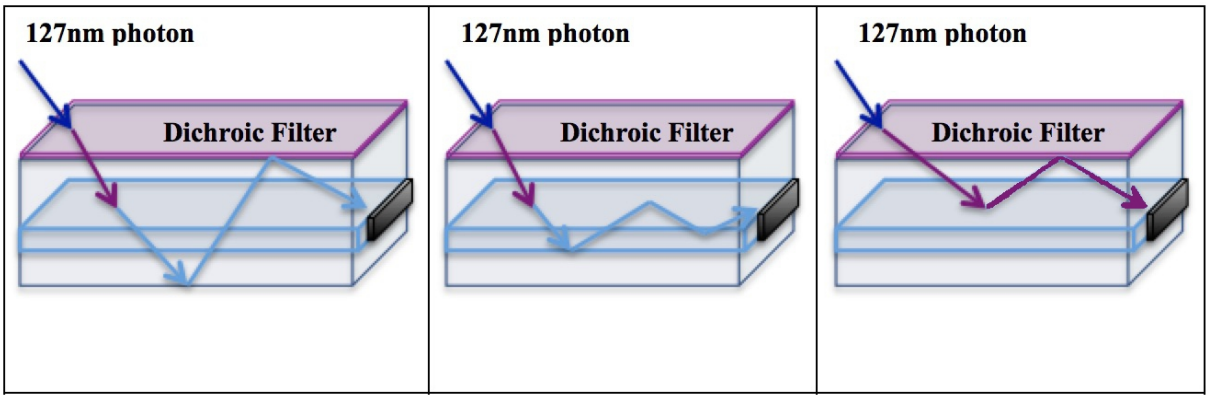

Figure 2.5: Left: Standard S-ARAPUCA Mechanism, the WLS embedded slab is in the center of the ARAPUCA, connected to the active photon-sensor. Center: an example with total internal reflection with the slab. Right: High angle photons can be trapped between the dichroic filter and the slab [36].

2.2.2 Silicon Photomultiplier and Photon Detection Efficiency Definition

The ARAPUCA (and X-ARAPUCA) is a light collector technology, for photon detection the component it uses is the Silicon Photomultiplier (SiPM). Since the effect of the ARAPUCA is to increase the effective area of the SiPM, the same definitions and methods of studying the SiPM also apply to the ARAPUCA. This subsection establishes the main definition regarding the operation and efficiencies of the SiPM and the ARAPUCA photon collector.

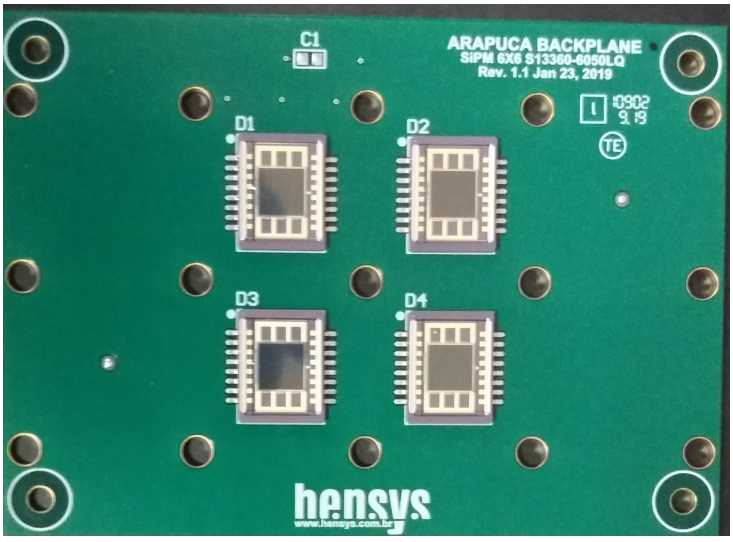

Figure 2.6: SiPM on the ARAPUCA back plane.

The Silicon Photomultiplier is a light detector able to detected single photons. To achieve this, the technology uses a solid-state microcell sensor based on silicon. When a photon hits the sensor, it transfers energy to a bound electron.

When the photon is absorbed by the bound electron, a pair of charge carriers is created, the charge carriers are accelerated by the electric field in the silicon microcell, generating

an avalanche of charge carriers.

Each silicon microcell is one Photon Avalanche Diode (SPAD), and can only detect a single photon at a time. A large array of SPAD microcells are used to allow for the detection of multiple photons at the same time, with each SPAD cell detecting a single photon.

Since the charge generated by a single photon in a SPAD is well defined and in principle a constant quantity, the resulting charge generated by multiple photons is expected to be proportional to the charge of a single photoelectron (SPhE).

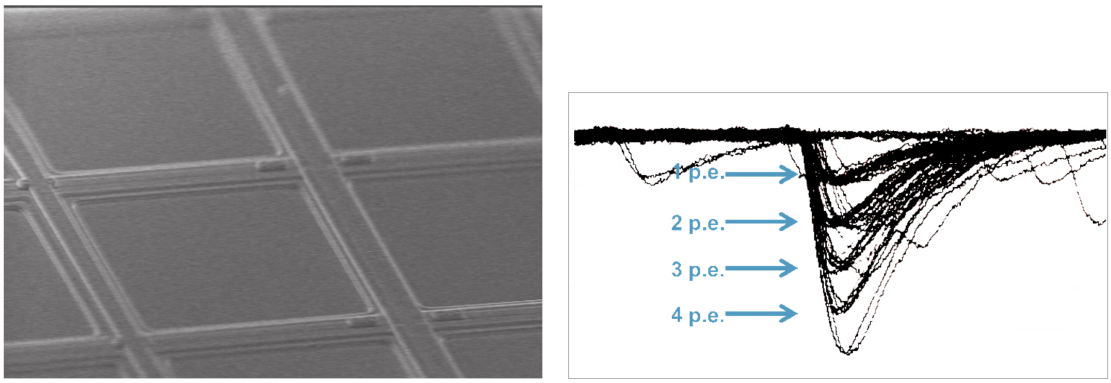

Figure 2.7: Left: Microcell structure of the SiPM, each cell can detected a single photon through a Geiger discharge, an uncontrolled generation of charge inside the microcell that produces a measurable current. Right: Waveshape for multiple due to different numbers of photons detected, the charge of the 4 photon signal is expected to be 4 times the charge for the 1 photon signal

Knowing the amount of the charge produced by a single photon is important information for the calibration of any experiment using SiPM as photon detector [38].

Another useful information from Single Photon Electron signals is their waveshape, shown in the right image of figure 2.7. The waveshape of a single SPhE has the information on how the electronics of the SiPM affect the light signal detected by it. This is called the electronic response of the SiPM, that is, how the SiPM electronics respond to a unitary pulse of signal, that is a single photon for light signals.

The total voltage applied to the SiPM is the Bias Voltage. The breakdown voltage (V_{br}) is the bias point at which the field strength is enough to generate a measurable avalanche of charge carriers, called a Geiger discharge. SiPM sensors usually operate at bias voltage higher than the breakdown voltage. The voltage above the breakdown voltage is the overvoltage, and the probability a discharge will happen after the initial charge carriers are created depends on the overvoltage. The charge generated by single photoelectron (SPhE charge) also depends on the overvoltage.

The Quantum Efficiency (QE) of a SiPM is the likelihood of an incident photon creating an electron-pair hole in the SiPM.

The photon detection efficiency (PDE) on the other hand is the probability that an incident photon will produce an avalanche. It differs from the QE because not all carriers will produce avalanches. Different bias voltages generate different photon detection efficiencies due to different overvoltages.

One of the noise sources in a SiPM based photon-detector is the Dark Count Rate, associated with thermal electrons producing avalanches. Since a thermal electron will be accelerated in the same way as a photon electron, the waveshapes are the same.

The main source of noise is optical crosstalk, that happens when accelerated carriers emit thermal photons during the avalanche, this photons can be detected by the SiPM, resulting in a single photon counting as multiple photons.

The last noise source is the possibility of afterpulsing, that occurs when a carrier becomes trapped by defects in the silicon, an avalanche can be started when the carrier is released, causing a delayed pulse.

The PDE can be calculated by estimating the number of photons hitting the SiPM, comparing with the number of photons actually detected by SiPM [39], and correcting for noise sources.

2.3 Scintillation in Liquid Noble Elements

Liquid argon (and other noble elements) have interesting properties for particle physics research such as high scintillation yields, being capable of being cleaned to high purity, are scalable to large sizes, a time scintillation structure useful for particle discrimination.

There are plenty of applications beyond neutrino physics for Liquid Noble Elements (LNE) such a calorimetry in high energy experiments [40], or the search for rare events such as dark matter [41] and neutrinoless double beta decay [42], and even medical applications[40].

Applications of LNE technology can benefit from a better understanding of the fundamental physics behind LNE (including LAr) scintillation processes, and there are still questions regarding the physics behind the time profile of LAr Scintillation and the effects of doping Liquid Argon with small quantities of Xenon.

This chapter will focus on the consolidated understanding of the physics behind LNE scintillation in the Vacuum Ultraviolet (VUV) light, its physical mechanism, time profile and quenching, as well as explain the current questions regarding LNE scintillation.

The three liquid noble elements with properties useful for detectors are Argon, Xenon and Krypton. Neon and Helium have very low boiling points (lower than liquid nitrogen), making them hard to cool, and their scintillation light is below $90nm$, where no transparent materials are available. For that reason most studies of the scintillation properties of LNE focus on liquid Argon (LAr), Xenon (LXe) and Krypton (Kr)[43, 44, 27].

In LNE scintillation there are two mechanism for producing light, the first one is due to excited molecules produced through the recombination process of molecular ions R_2^+ and free electrons (R denotes an LNE atom), the recombination produces excited dimers that decay emitting light . The other is due to direct formation of excited LNE atoms called excitons (R^*), that combine with other LNE atoms to form the same excited dimers

(R_2^*) as in the recombination process. Both this processes are shown in equation 2.3:

$$\begin{aligned} R^* + R &\rightarrow R_2^* \rightarrow 2R + 1\gamma \\ R_2^+ + e^- &\rightarrow R_2^* \rightarrow 2R + 1\gamma. \end{aligned} \tag{2.3}$$

The excited dimers has two light components of the same wavelength, one with fast emission and one with slow emissions. The fast component is associated with the transition from a singlet excited state back to the ground state (${}^1\Sigma_u^+ \rightarrow {}^1\Sigma_g^+$), and the slow component is associated with the transition from a triplet state (${}^3\Sigma_u^+ \rightarrow {}^1\Sigma_g^+$).

The emission time varies between liquid noble elements. The fast component has a emission time of few nanoseconds for Argon, Krypton and Xenon. The slow component on the other hand varies more, the xenon triplet state has an emission time of $22ns$, with $85ns$ for Krypton, while Argon's slow component has been measured in the range of microseconds (about 1.6 μs) [42].

It also should be noted that the presence of an eletric field hinders the recombination process, resulting in the light yield of LNE decreasing.

2.3.1 Liquid Argon Scintillation Properties

Liquid Argon (LAr) is the most common LNE used in large physics experiments, mainly due to it's availability. It's fast singlet decay time followed by a slow (1.6 μs) triplet decay times allows for pulse shape discrimination between particles in a detector. It's notable that one could theoretically distinguish background nuclear recoil from Dark Matter WIMP events [41].

The scintillation process in argon is the same as in equation 2.3. It can happen either through direct excitation of argon atoms that lead to the formation of excited dimers (Ar_2^*). Or through recombination of ions formed by the energy transfer from ionizing particles.

The energy needed to ionize an atom is it's W value, for Argon $W = 23.6eV$. If the energy absorbed is E, the number of ions formed is $N_i = T/W$, with T being the energy deposited into ionization. The ratio between ionization and excitation has been measured at $N_{ex}/N_i = 0.21$ [45], implying $T = 0.82E$. Only about half the energy deposited by a charged particle in LAr is deposited near the track core, the other half is taken away by the electrons generated by primary ionization (called δ rays) and is deposited in a region further from the core of the ionization track, in a region called the penumbra of the track [45].

After the excitation and formation of the argon excited dimers, they can lose their energy without scintillating by quenching [45].

Quenching is the process in which the excited dimers are de-excited without scintillating. The mechanism for quenching are not fully clarified, but one possible mechanism proposed the de-excitation of an excited dimer by collision with other excited dimmer [47]. The quenching can happen between argon atoms (self-quenching), but it can also happen with contaminants such as N_2 [46]. There is only a short time for the quenching to

happen before the dimer self-traps, after that the de-excitation process will occur leading to scintillation light on the VUV spectrum: $Ar_2^* \rightarrow 2Ar + 1\gamma$ [46].

The ratio of singlet and triplet excited dimers formed depends on the type of ionizing particle and its linear energy transfer (LET). That means that the amount of light released by fast and slow components is different for different particles, allowing for particle discrimination [41]. For example, the ratio between singlet and triplet states A_S/A_T is 1.3 for alpha particles and 3 for nuclear recoils.

The simple model for light emission in liquid argon would be to just take into account the singlet and triplet decay with their relative abundance, this can be written as:

$$l(t - t_0|\tau_s, \tau_t, \alpha_s, \alpha_t) = \frac{\alpha_s}{\tau_s} e^{-\frac{t-t_0}{\tau_s}} + \frac{\alpha_t}{\tau_t} e^{-\frac{t-t_0}{\tau_t}}, \tag{2.4}$$

where $l(t)$ is the probability of light emission at the time t, τ_s and τ_t are the characteristic emission time of the singlet and triplet states respectively, α_s and α_t are the constants related to the relative abundance of each state, and t_0 is the starting time of the signal [41]. The model graph is in figure 2.8.

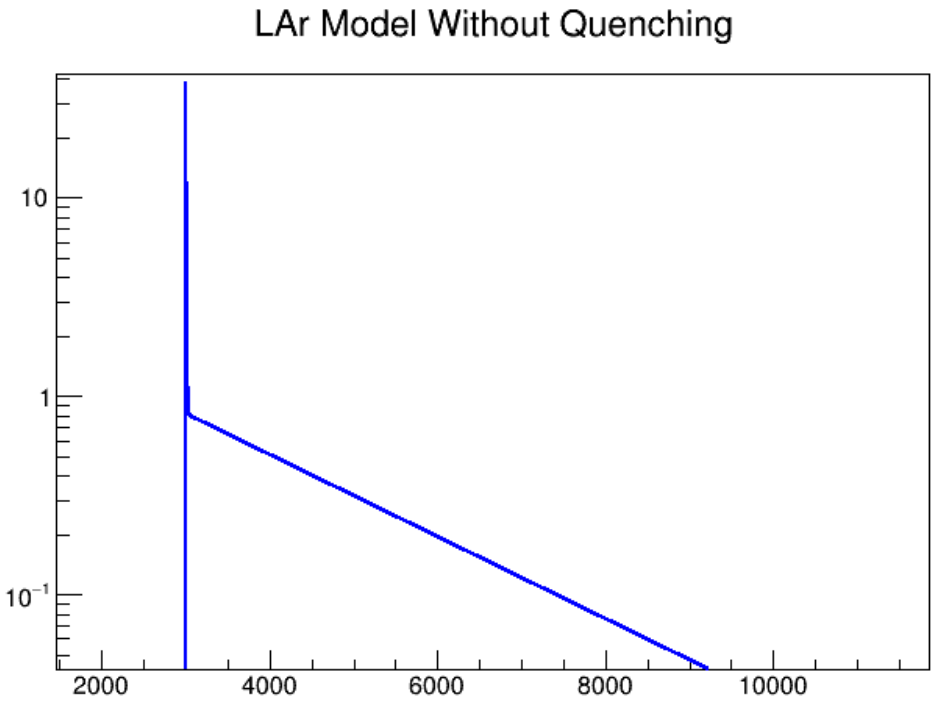

Figure 2.8: Graphic of the model in equation 2.4

The ration between the singlet and triplet states $\frac{\alpha_s}{\alpha_t}$ is associated with the energy deposition and the particle in question. In theory, this ratio could be used to discriminate between different particles, since different ionizing particles produce different amounts of fast and slow scintillation in LAr.

In practice, the actual pulse shape observed in an experiment depends not only on the actual physical shape of the signal, but also on the electronic response of the photon detection system. Fitting a pulse shape to a model is not always easy.

Because of that the usual method for pulse shape discrimination for different particles uses the integral of the pulse shape in question. Since singlet and triplet components have different emission times, the ratio of total light seen early in the signal and the total light seen is associated with the ratio of singlet and triplet components. For this method the pulse shape parameter F_{prompt} is defined as:

$$F_{prompt} = \frac{\int_{t_0}^{t^*+t_0} V(t)dt}{\int_{t_0}^{t_f} V(t)dt}, \tag{2.5}$$

where $V(t)$ is the signal waveshape, t_0 is the initial time, t_f is a time long enough to include the full signal, and t^* is a time chosen to maximize the difference of the F_{prompt} parameter for different particles, it's usually around $100ns$ [41].

2.3.2 Quenching in LAr

This description of LAr Scintillation and it's emission time structure is good, but has some physical limitations. Even though the mechanism behind light emission in LAr is well understood, there are experimental results that aren't well explained.

It is known that part of triplet states are quenched, and the total light emitted does not represent 100% of the excited dimers form due to this quenching effect [45]. Integrating equation 2.4 it's easy to see that this effect is not taken into account:

$$L = \int_{t_0}^{\infty} l(t - t_0)dt = \alpha_s + \alpha_t = 1. \tag{2.6}$$

A model that includes the effects of quenching on effective light yield was proposed by Segreto, 2020 [47], the model also explains other experimentally observed phenonema with LAr Scintillation, such as the dependence of the slow component with electric field, and predicts the pulse shape parameter F_{prompt} for electron and nuclear recoils.

There is no consolidated understanding of the quenching process in LAr and the exact mechanism that leads part of the energy deposited to be quenched. The model proposed by Segreto [47], studied in this thesis, proposes two mechanism for the quenching process: the collision between to excited argon dimers (Eq. 2.7) and the collision between one excited dimmer with one ionized dimmer (Eq. 2.8):

$$Ar_2^* + Ar_2^* \rightarrow Ar_2^* + 2Ar, \tag{2.7}$$

$$Ar_2^* + Ar_2^+ \rightarrow Ar_2^+ + 2Ar. \tag{2.8}$$

These two effects indicate that there is potential for a larger photon yield if the quenching process was not happening, this is consistent with the larger photon yield observed in Xenon doped LAr experiments. Even small amounts of Xenon in LAr have enhanced the total Light Yield beyond what would be expected, this model explains this increase by suggesting that the Xenon can scintillate part of the energy that would be lost in the quenching process.

The model also assumes only triplet state dimmers quench, with that it is possible

to calculate the light emission probability based on the instant variation of triplet states N_3, and the number density of ionized dimers (N^+). Considering the interactions happen along the ionizing particle track, the modified diffusion equation for this two terms are:

$$\frac{dN_3}{dt} = D\nabla^2 N_3 - \lambda_3 N_3 - \sigma^+\nu^+ N^+ N_3 - \sigma_3\nu_3 N_3^2 \tag{2.9}$$

$$\frac{dN^+}{dt} = D^+\nabla^2 N^+, \tag{2.10}$$

where N_3 and N^+ depend on time and position. D and D^+ are the diffusion constants of Ar_2^* an Ar_2^+ respectively, λ_3 is the emission (de-excitation) rate of excited dimers in the triplet ($^3\Sigma_u^+$) state, σ^+ is the cross section for process 2.8, ν^+ is the relative velocity between excited and ionized dimers, and σ_3 is the cross section for process 2.7 with ν_3 being the relative velocity between two excited dimers.

Assuming that the distribution of excited and ionized dimers is uniform around the particle track, and that the diffusion terms can be neglected in the timescale that quenching happens, this implies rewriting the equations with $\nabla^2 N_3 = 0$ and $\nabla^2 N^+ 2 = 0$. For equation 2.10, this results in $dN^+/dt = 0$, assuming $N(t=0) = N_0^+$ as the initial condition. Using this in equation 2.9:

$$\frac{dN_3}{dt} = -\lambda_3 N_3 - \sigma^+\nu^+ N_0^+ N_3 - \sigma_3\nu_3 N_3^2. \tag{2.11}$$

This equation can be rewritten with more convenient terms, assuming the initial condition $N_3(0) = N_0$ and defining $k^+ = \sigma_+\nu_+ N_0^+$, $q = N_0\sigma_3\nu_3$, and $\lambda_q = \lambda_3 + k^+$. Using this definitions, the equation is:

$$\frac{dN_3}{dt} = -\lambda_3 N_3 - k^+ N_3 - \frac{q}{N_0}N_3^2 = -(\lambda_3 + k^+)N3 - \frac{q}{N_0}N_3^2 = \lambda_q N3 - \frac{q}{N_0}N_3^2. \tag{2.12}$$

This is a Bernoulli equation and can be solved by the substitution $N_3 = 1/y$, with $y_0 = y(0) = 1/N_0$, and differentiating $dN_3/dt = -\frac{1}{y^2}\frac{dy}{dt}$. Rewritting equation 2.12 in terms of y:

$$\begin{aligned}
-\frac{1}{y^2}\frac{dy}{dt} &= -\lambda_q - \frac{q}{N_0}\frac{1}{y^2} && |\times -y^2 \\
\frac{dy}{dt} &= \lambda_q y + \frac{q}{N_0} && |\text{Reordering} \\
\frac{dy/dt}{\lambda_q y + \frac{q}{N_0}} &= 1 && |\text{Integrating on } dt \\
\frac{1}{\lambda_q} ln(\lambda_q y + q/N_0) &= t + C_0 && |C_0 \text{ constant} \\
\lambda_q y + \frac{q}{N_0} &= e^{\lambda_q t} C_1 && |C_1 = e^{\lambda_q C_0} \text{ constant.}
\end{aligned} \tag{2.13}$$

Setting $t = 0$ determines $C_1 = \lambda_q y(0) + q/N_0 = (\lambda_q + q)/N_0$. Using that and rewriting

the equation in terms of N_3 again:

$$\begin{aligned} \frac{\lambda_q}{N_3} + \frac{q}{N_0} &= \frac{\lambda_q + q}{N_0} e^{\lambda_q t} && \text{|Reorganizing} \\ \frac{\lambda_q}{N_3} &= \frac{\lambda_q}{N_0} e^{\lambda_q t} + \frac{q}{N_0}(e^{\lambda_q t} - 1) && \text{|Isolating } N_3 \\ N_3 &= \frac{N_0}{\frac{1}{\lambda_q}(\lambda_q e^{\lambda_q t} + q(e^{\lambda_q t} - 1))}. \end{aligned} \tag{2.14}$$

Reorganizing and writing it in term of $e^{-\lambda_q t}$:

$$N_3(t) = N_0 \frac{e^{-\lambda_q t}}{1 + \frac{q}{\lambda_q}(1 - e^{-\lambda_q t})}, \tag{2.15}$$

this represents the number density of triplet excited dimers that can emit light with unquenched characteristic time τ_3, writing $\tau_q = 1/\lambda_q$, and including the singlet emissions, the probability density for light scintillation in LAr is:

$$l(t) = \frac{\alpha_s}{\tau_s} e^{-t/\tau_q} + \frac{\alpha_3}{\tau_3} \frac{e^{-t/\tau_q}}{1 + q\tau_q(1 - e^{-t/\tau_q})}, \tag{2.16}$$

in which α_s and α_3 are the relative abundance of singlet and triplet excited dimers, a graph of this model is shown in figure 2.9, as well as a comparison with the scintillation model without quenching (Eq. 2.4). Integrating $l(t)$ to get the total light emission parameter L:

$$L = L_S + L_3 = \alpha_s + \alpha_3 \frac{ln(1 + q\tau_q)}{q\tau_3}, \tag{2.17}$$

L is proportional to the total light emitted, and since this model includes the quenching effect, $L = \alpha_s + \alpha_3 = 1$ only if $\tau_3 = \tau_q$ and $q = 0$, so no quenching would be happening.

With this model is also possible to write τ_q as a function of the electric field, and to include xenon doping effects that increase the total light yield, the latter will be talked about in chapter 4.

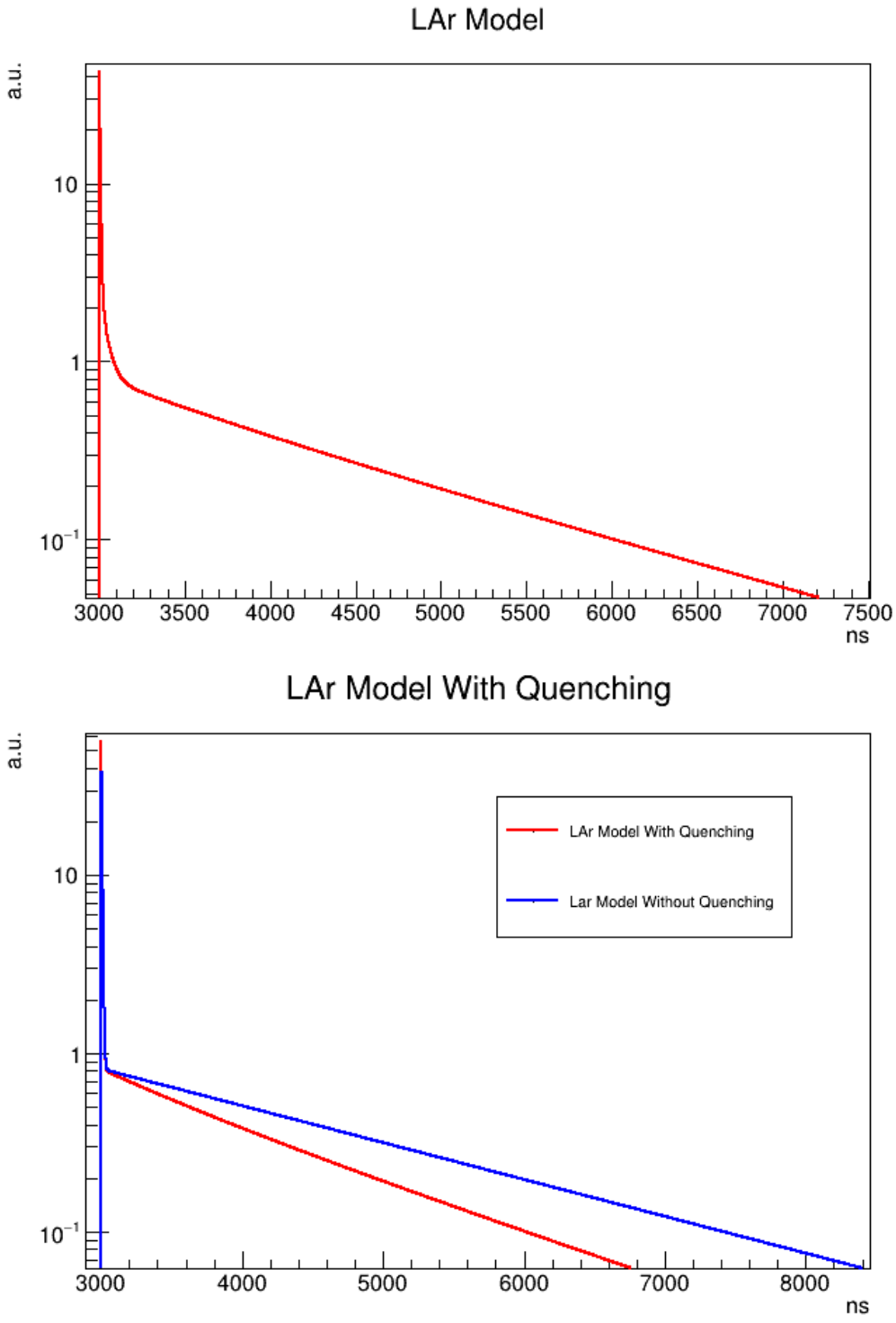

Figure 2.9: Top: Graph of the model in eq. 2.16, including the effects of quenching. Bottom: Comparison between the model in eq. 2.16 and the model in eq. 2.4, the quenching affects the effective triplet emission time.

Chapter 3

ARAPUCA Quantum efficiency and Waveshape Analysis

This chapter is dedicated to the analysis of an experimental test conducted at Lab Leptons, at UNICAMP, during late 2019. This experiments provided data regarding Argon Scintillation as seen by the X-ARAPUCA photon collector.

The data allows for two results, the first is the determination of the quantum efficiency of the X-ARAPUCA module. This was a highly collaborative effort that involved most of the active members of the Lab Leptons group at the time, the analysis was part of the PhD thesis of Souza H.V. [48, 49], and I reproduced his results as a form of reviewing his code and the analysis process, it also served as a didactic effort to learn the tools to conduct and analyze similar experiments.

The second part of this chapter is dedicated to the wave shape analysis of the signals seen in LAr using the model proposed by Segreto,2020 [47], described in the previous chapter, in subsection .

3.1 Experimental Set Up and Data Acquisition

The device under test (DUT) in the experiment and analysis described in this chapter is the X-ARAPUCA prototype[36].

The DUT has external dimensions of 9.6 $cm \times 12.5$ cm with a dichroic filter (from OPTO [50]) with area 8 $cm \times 10$ cm, with 400 nm cutoff in wavelength. The transmissivity below the cutoff is 90% (between $300 - 400$ nm), and the reflectivity above the cutoff is 98% ($400 - 500$ nm). The internal wavelength shifter (WLS) is a 3.5 mm thick Eljen EJ-286 [51], with maximum absorption at 350 nm and emission at 430 nm. This matches the emitted wavelength from the external WLS and the reflectivity band internally, as shown in figure 2.4.

Two arrays of 4 SiPM are installed on the lateral cavity (SiPM model: Hamamatsu S13360-6050VE [52]). The 4 SiPM are passively ganged in parallel, sharing the same voltage. The insides of the module not occupied by the SiPMs are covered with the highly reflective 3M ESR Vikuiti foils [53].

The cryogenic set up assembled for the prototype X-ARAPUCA photon collection

efficiency test is shown in (figure 3.1). The DUT is held vertically inside the inner stainless-steel cylinder (green) by a PVC support that also hosts the α source. An optical fiber inside the cylinder is connected to a LED light source, and the X-ARAPUCAs inside are connected to an amplifier and then to the digitizer. The outer cryostat (in yellow) is filled with liquid argon for the thermal bath.

The steel cylinder in figure 3.2 right is pumped to a pressure of $10^{-6} mbar$ in two steps, the first at room temperature (up to $10^{-4} mbar$) and the second at cryogenic temperature, using the cryostat as a thermal bath, filled with commercial LAr.

When the desired vacuum is achieved, the valve is closed and Gas Argon 6.0 (meaning less than 1ppm contamination) is injected in the internal cylinder, and it liquefies by exchanging heat with the thermal bath.

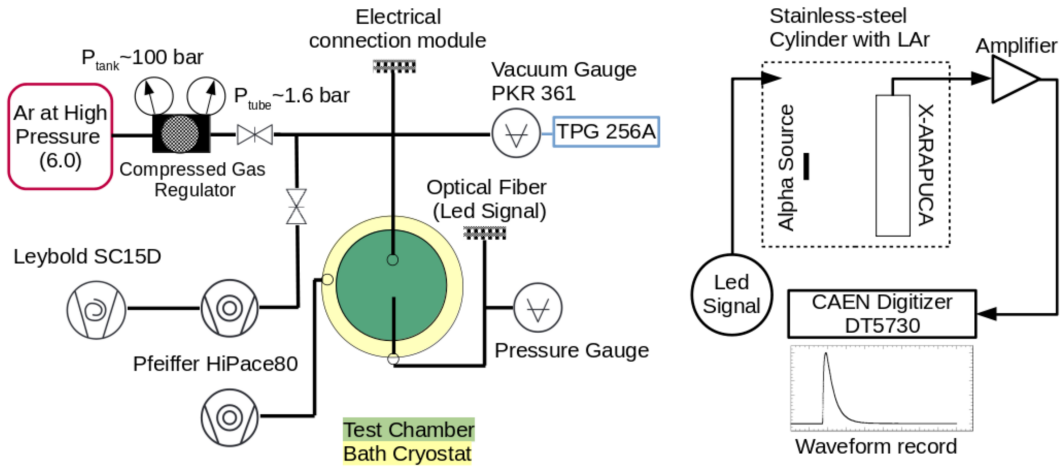

Figure 3.1: Right: Schematic of the cryogenic setup for testing of ARAPUCA modules, the main cryostat is in green, connected to a LED light source through an optical fiber. Gaseous argon is injected in the inner cylinder and liquefied with a thermal bath with liquid argon in the outer cryostat. Left: Schematic diagram of the DAQ. The SiPMs inside are connected to the amplifier and to the CAEN Digitalizer, standing 3cm apart from the α source.

The liquid argon level is measured with a resistor (figure 3.2), when the liquid argon submerges it, the resistance change, and this means that the set up is submerged in LAr.

The structure holding the prototype and the α source facing each other (figure 3.2) is made of PVC (Polyvinyl chloride), The X-ARAPUCA and the α source are facing each other 3 cm apart. Inside the X-ARAPUCA there are a total of 8 SiPM divided into two arrays of 4 SiPM ganged in parallel, each of the two arrays has a readout channel.

The signal is amplified by a pre amplifier from Hensys [54] (gain of 32db, low-noise, two channels). The read-out system is a 14 bit CAEN DT5730 digitizer with frequency of $500 MHz$.

The α source is made of aluminium alloy and natural uranium in the form of a disk $0.14mm$ thick and $1cm$ diameter. The energy and relative intensity of each decay mode of the source is detailed in table 3.1.

The data acquisition (DAQ) is performed through the CAEN digitizer and written into a computer using the *wavedump* software. The readout was performed any time

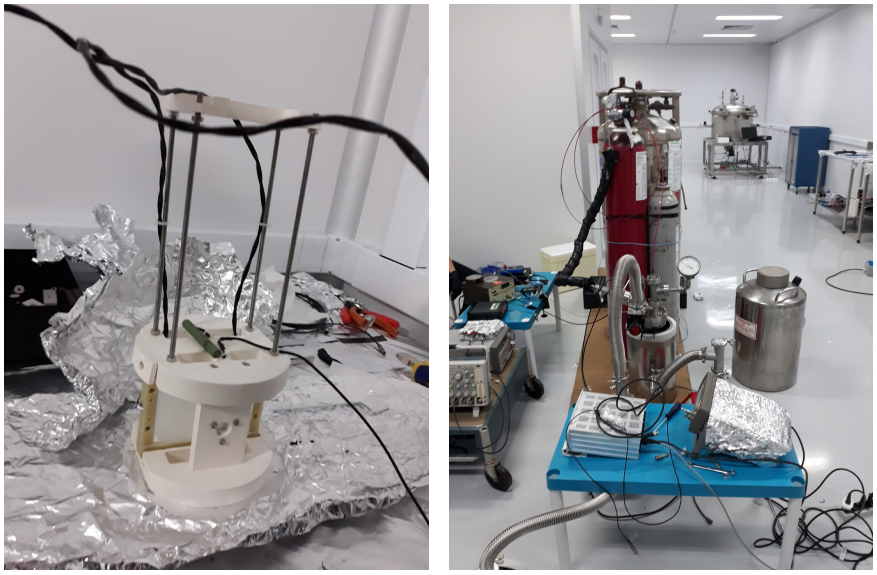

Figure 3.2: Left: X-ARAPUCA prototype with the alpha source in the PVC support. Right: Cryogenic set up.

α energy (MeV)	relative intensity	parent nucleus
4.187	48.9%	^{238}U
4.464	2.2%	^{235}U
4.187	48.9%	^{234}U

Table 3.1: Emission lines of the thick aluminium alloy α source [49].

one X-ARAPUCA array exceeded a threshold corresponding to about 5 photo-electrons, the value of the photoelectron is estimated by looking at the charge histogram generated during the calibration run, as explained in subsection 3.2.1; Each triggered event was sampled 9000 times in intervals of $2ns$, resulting in $18\mu s$ of signal time, with $3.6\mu s$ pre-trigger.

Each time the bias voltage was changed, a calibration run was made. The light of the LED source was used, with the goal of detecting one or few photons at a time to determine SPhE charge and shape. The data acquisition is triggered by the LED pulse, instead of a threshold as in the α source readout. A blue LED was flashed with pulses of $50ns$ duration at $1kHz$ frequency.

3.2 Photon Detection Efficiency Calculation

This sections details the analysis of the data in the determination of the X-ARAPUCA detection efficiency. The SiPMs were operated with bias voltages of 46.5, 47.0, 47.5, 48.0 and $48.5 \pm 0.2\ V$, representing overvoltages of $+3.5V$, +4.0, +4.5, +5.0 and $+5.5V$ above the breakdown voltage, respectively.

There are two main things needed to evaluate the photon detection efficiency: an estimation of the number of photons detected, and an estimation of the number of photons crossing the X-ARAPUCA module window. Correction due to nitrogen contamination

and optical crosstalk from the SiPM (subsection 2.2.2) are also included in the detection efficiency calculation.

3.2.1 Calibration and Average SPhE

The number of photons detected by the X-ARAPUCA in a signal is the total charge of the signal divided by the charge of a single photon (SPhE charge), divided correction factors due to dark noise and optical crosstalk, $\gamma = \frac{\text{Signal Charge}}{\text{SPhE Charge}}/(\text{Correction Factors})$. The correction factor for the dark noise and optical crosstalk, defined in subsection 2.2.2, range from 1.32 to 1.58 depending on bias [49].

To determine the charge generated by a single photon, a low light scenario is created, so each waveform will contain only a few photons. These waveforms are acquired using the LED as external trigger.

The low light signals are then integrated for about $900ns$ after the pre-trigger time ($3600ns$). An histogram is constructed using the integrated values.

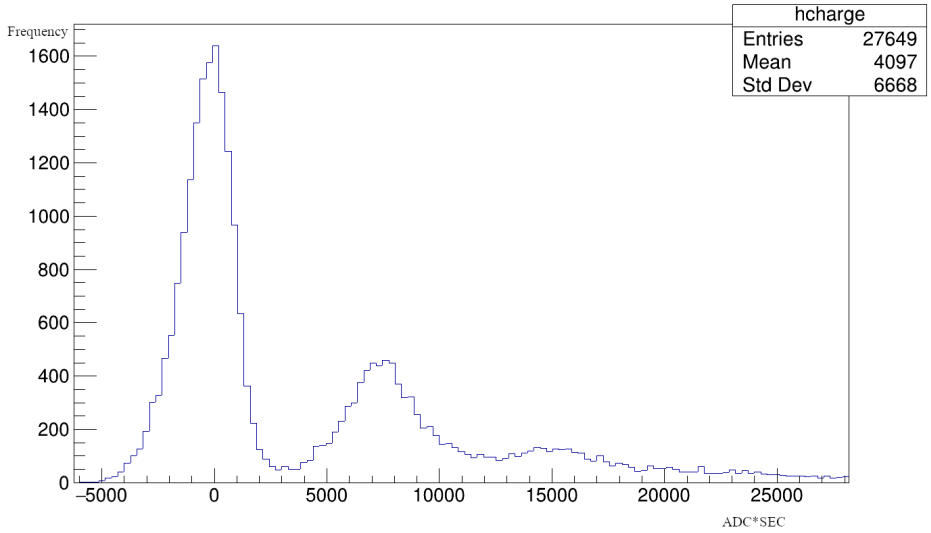

Figure 3.3: Histogram generated from LED signals with few photons. The expected result is a multigaussian distribution, with each Gaussian peak centered at the charge generated by a specific amount of photons.

The expected result is a multigaussian shape, with each peak corresponding to 0, 1, 2... photon electrons of charge $(adc \cdot nsec)$, shown in figure 3.3.

The charge of a single photon is the mean value of the Gaussian peak corresponding to the single photon in the histogram. In order to determine this value, the histogram in figure 3.3 is fitted with the following multigaussian model:

$$F(q) = \sum_{i=0}^{N} A_i exp(-\frac{(q-\mu_i)^2}{2\sigma_i^2}), \tag{3.1}$$

in which $F(q)$ is the frequency of charge q in the histogram, μ_i is the charge generated by i photons, A_i is the relative amplitude and σ_i the standard deviation of the $i-th$

peak, and N is the total number of peaks.

To help the fit work, we also use the following assumptions:

- The charge of the $K-th$ peak should be $K \times \mu_1$, μ_1 being the peak for a single photon.
- The standard deviation of the $K-th$ peak should be $\sigma_k = \sqrt{K} \times \sigma_1$, σ_1 being the standard deviation of a single-photon electron peak. The charge of multiple photons hitting the SiPM is independent since each photon hits a different microcell, generating charge independently from other photons, as explained in subsection 2.2.2. Thus the standard deviation in charge of multiple photons is given by the addition of multiple independent standard deviations of the same value $\sigma_k^2 = K \times \sigma_1$.

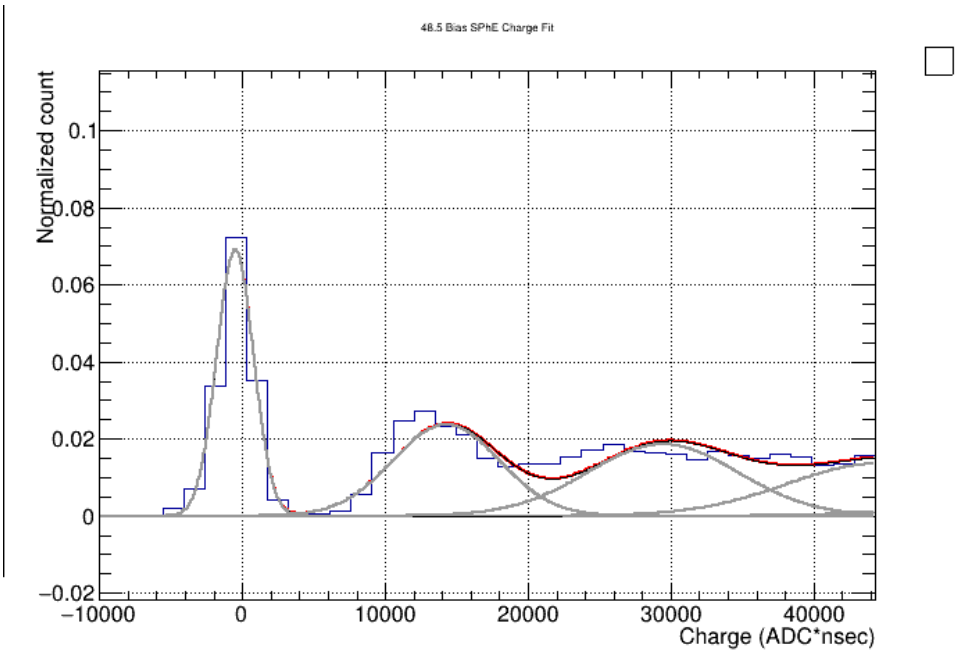

Figure 3.4: Multigaussian fit example (Eq. 3.1) for run with $48.5V$ overvoltage, the run with the voltage bias with the highest efficiency. The fit assumes that the charge of multiple photons is proportional to the charge of a single photon. The mean of the Gaussian of each peak is the charge generated by that amount of photons.

Bias	μ_1	μ_2
46.5 V	9560	18790
47.0 V	10440	21000
47.5 V	11560	23890
48.0 V	12840	26230
48.5 V	14410	29030

Table 3.2: Fit results from Eq. 3.1 for each bias voltage. The mean charge for two photons (μ_2) is proportional to the mean of a single photon (μ_1)

The charge generated by a photon is set as the mean of the Gaussian associated with one photon in the multigaussian distribution, shown in figure 3.4, that is the value μ_1 in equation 3.1.

The result is expressed in charge units of $adc \times nsec$, the charge unit is not relevant, since the charge contained in each waveform is calculated in the same units and then the ratio of the two is taken to derive the number of detected photons. The fit results for values of μ_1 and μ_2 are shown in table 3.2.1.

3.2.2 Optical Crosstalk Estimation

Optical crosstalk is the main noise source in SiPM, it happens when the detection of a photon generates a second photon that is also detected, as explained in subsection 2.2.2. This effect causes an over counting of photons, and is compensated for to determine the efficiency of the X-ARAPUCA.

The nominal crosstalk of a SiPM specified in it's technical information's is determined at room temperature. The crosstalk depends on temperature, and since the experiment is performed at liquid argon temperatures, the nominal crosstalk is not usable, making necessary to determine the crosstalk with the experiment.

The method for estimating crosstalk is described in [55]. It's assumed that the primary light pulses, generated either by argon scintillation or thermal electrons, follows a Poisson distribution with mean $\lambda = L$.

Each primary pulse can generate one or more additional pulses due to crosstalk, each crosstalk pulse has the same probability p of being generated. There is no limit to the number of crosstalk pulses that can be generated, meaning that the first crosstalk pulse can generate a second crosstalk with probability p, and the second pulse can generate a third and so on...

With those assumptions the probability for k photo-electrons pulses due to a primary pulse is:

$$P(k; L, p) = \sum_{i=0}^{k} B_{i,k} \cdot e^{-L} L^i \cdot (1-p)^1 \cdot p^{k-i}, \tag{3.2}$$

with L being the mean value of the Poisson distribution of primary pulses, and p being the crosstalk probability in the binomial distribution of crosstalk pulses, and $B_{i,k} = (k-1)!/i!(i-1)!(k-i)!$ if $i > k$, otherwise $B_{0,0} = 1$ and $B_{0,k>0} = 0$ [55].

With the calibration data we can count the number of events with $k = 1, 2, 3...$ photons and fit to the model in equation 3.2. In the X-ARAPUCA test in late 2019, the result was between $p = 0.4 - 0.6 \pm 10\%$, consistent with other measurements of crosstalk in LAr temperature [49].

3.2.3 Monte Carlo Simulation

The goal of the Monte Carlo Simulation of the experimental set up is to estimate the number of photons crossing the X-ARAPUCA window during the alpha scintillation events. This results in a histogram associated with the number of photons crossing the

light collector that can be compared by the number of photons detected, resulting in a estimation of the X-ARAPUCA detection efficiency. A Geant4 Monte Carlo Simulation was developed by Sarmento, R. [56]. The dimensions of the experimental set up described in section 3.1 were measured and implemented as shown in figure 3.5.

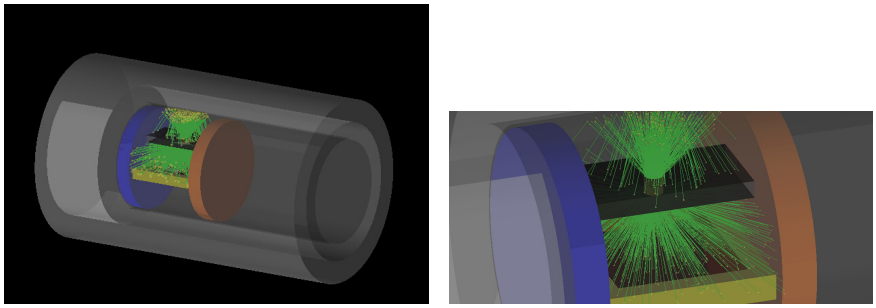

Figure 3.5: Images from the simulation of the experimental setup [56]. The green lines are the photons tracked, the amount of photons crossing the X-ARAPUCA window (in yellow) is counted.

The liquid argon scintillation light yield was set at 51000 photons per MeV (γ/MeV) times the quenching factor (0.71 for α). The emissions of the source was set uniformly and isotropically inside the aluminium disc [48]. The result of the simulation is an histogram of the frequency of the number of photons that cross the X-ARAPUCA window in each event, the histogram is shown in figure 3.6, this histogram is compared with an experimental histogram of the same kind to determine the X-ARAPUCA photon detection efficiency.

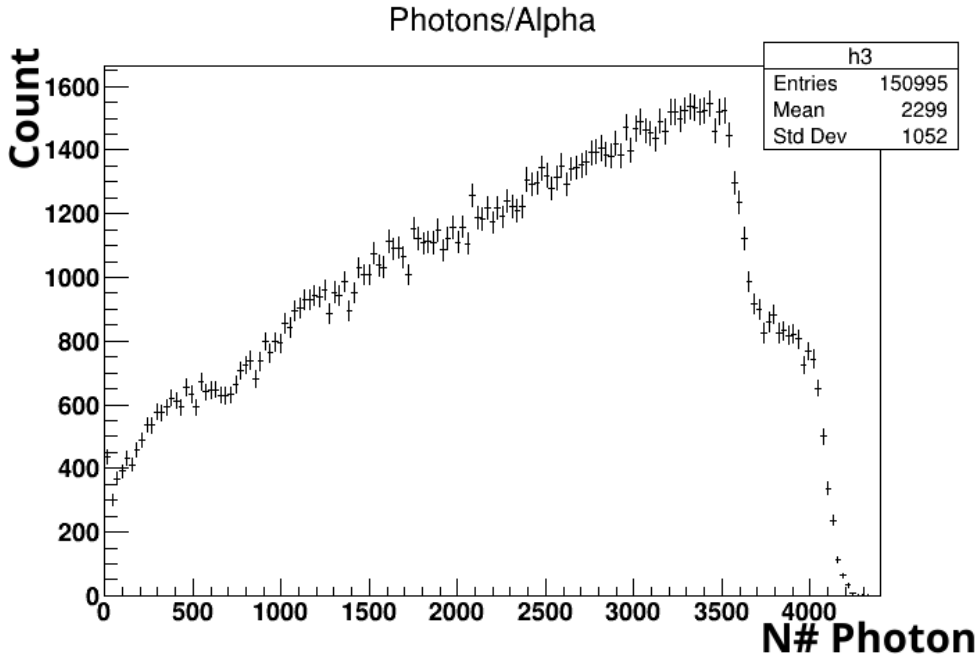

Figure 3.6: Simulated histogram of the number of times a number of photons (x-axis) crossed the detector window in a single event due to an alpha particle event, with the count of that frequency in the y-axis

3.2.4 Photon Detection Efficiency for Alpha Particles

With the simulated distribution of photons crossing the X-ARAPUCA window, the next step is to compare the number of photons in the simulation with the experimental results. The simulation does not take into account all effects occurring in the experiment, it is necessary to add a few factors to the simulation.

- **Exponential Noise** due to very low energy background radiation entering the stainless-steel vessel, this radiation comes from ionizing particles from cosmic ray, or generated by radioactive particles in the soil and atmosphere. This background radiation noise isn't simulated, so an additional exponential decay term is added to the simulated spectrum.
- **Gaussian Smear:** the experimental spectrum is smeared due to the effects of the electronics of the SiPM, to account for that the simulated spectrum goes through a Gaussian smear.
- **Efficiency of the X-ARAPUCA**: The X-ARAPUCA photon collector is not simulated, resulting in the simulation being scaled up in relation to the number of photons in the experimental histogram. This scale factor is the X-ARAPUCA efficiency.

The experimental spectrum is shown in figure 3.7, the number of photons (x-axis) is calculated by integrating the charge of an alpha signal ($t_0 + 300\ ns$ to $t_0 + 15000\ ns$, $t_0 = 3.6\mu s$ pre-trigger time) and dividing the value by the SPhE charge. The value is then multiplied by correction factors due to optical crosstalk and argon purity.

In order to estimate the effects of the Exponential Noise and the Gaussian smear, a preliminary fit is done between the experimental data and a model of the alpha source (table 3.1).

The model for a thick α source used in the experiment consists of three exponential terms associated with the three energy lines from the source as shown in table 3.1, convoluted with a Gaussian distribution to generate the Gaussian smear, plus a exponential decay to include the exponential noise [57].

$$F(E) = \sum_{i=1}^{3} \frac{A_i}{2\tau} exp\left(\frac{E-\mu_i}{\tau} + \frac{\sigma^2}{2\tau^2}\right) erf\left(\frac{1}{\sqrt{2}}\left(\frac{E-\mu_i}{\sigma} + \frac{\sigma}{\tau}\right)\right) + De^{-Ct}, \tag{3.3}$$

in equation 3.3 A_i is the relative intensity, μ_i is the mean energy of emission line i, τ is the slope of the tail on the low energy side and σ is width the emission peaks around their mean energies (μ_i), $i = 1, 2, 3$ are the energy lines in 3.1, C and D are the constants of the exponential decay to model the exponential noise.

Fitting the experimental spectrum with this model results in a value of σ for the Gaussian smear and the parameters for the exponential noise.

With the parameters associated with the Gaussian smear and Exponential Noise determined by the fit, these effects can be included in the simulated histogram of photons.

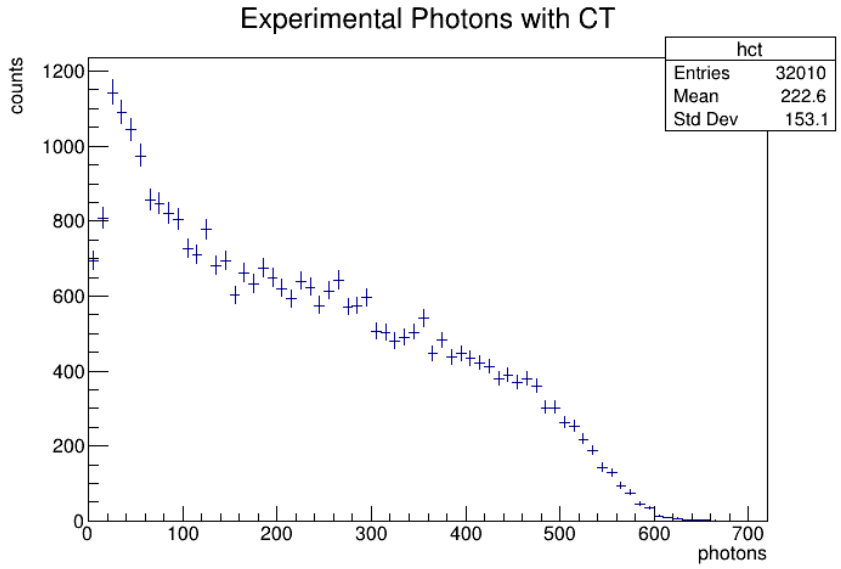

Figure 3.7: Normalized Experimental Histogram of frequency of number of photons detected: the light collected by the X-ARAPUCA single-cell is integrated from $t0 + 300\ ns$ to $t0 + 15000\ ns$ ($t_0 = 3.6\mu s$ pre trigger time), the integral value is corrected for to argon purity and cross-talk, and then divided by the SPhE charge, determined in the Calibration process.

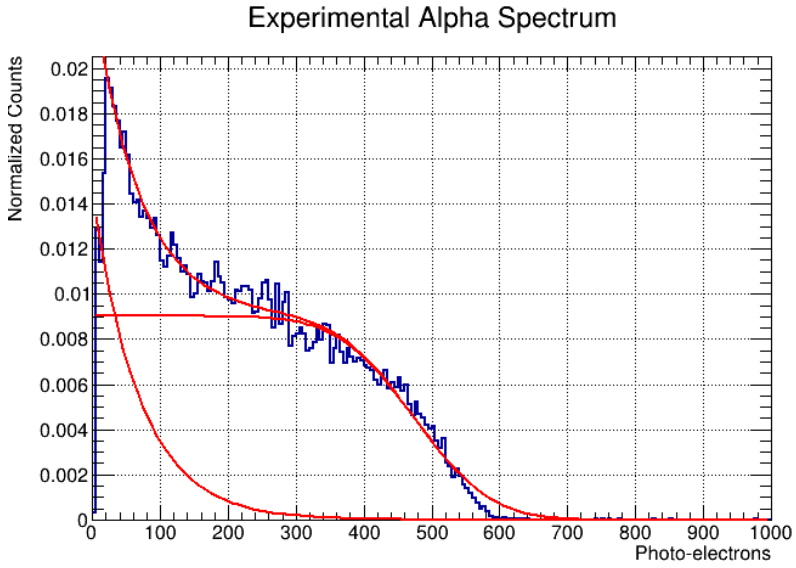

Figure 3.8: Model of fit (3.3) to determine the Gaussian smear and the exponential noise in the experimental data (σ).

The last effect not included is the photon detection efficiency (PDE) of the X-ARAPUCA, that is a scale factor on the number of photons seen.

The final step consists of fitting the updated simulation spectrum to the experimental spectrum with the X-ARAPUCA efficiency as a parameter to fit. For the fit the χ^2 difference between the two spectrum is minimized using the TMinuit class of the ROOT Framework [58].

For the X-ARAPUCA test in late 2019, the best efficiency measured was of 3.01±0.6 %

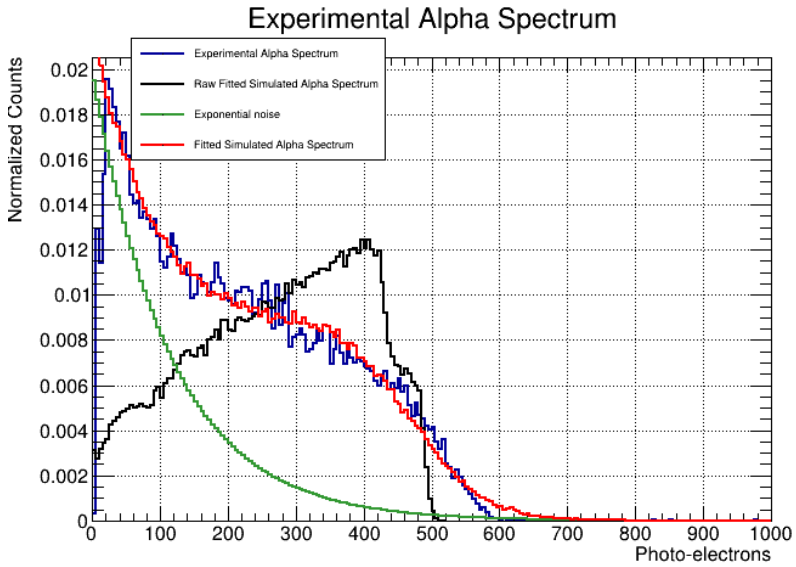

Figure 3.9: Example of fit between the simulated data and the experimental data, adding in the information about exponential noise (in Green) and Gaussian smear. With these factors included, the only difference between the experimental and simulated histograms is a scale factor on the x-axis, this scale factor is the X-ARAPUCA photon detection efficiency

at $48.5V$ of voltage bias [49]. Consistent with the 3.5 ± 0.5 % that was reported on the first X-ARAPUCA test [59]. The smaller efficiency could be due to thermal stresses causing micro-cracks in device under test, micro-cracks on the PTP coating were noticed after the test, shown in figure 3.10

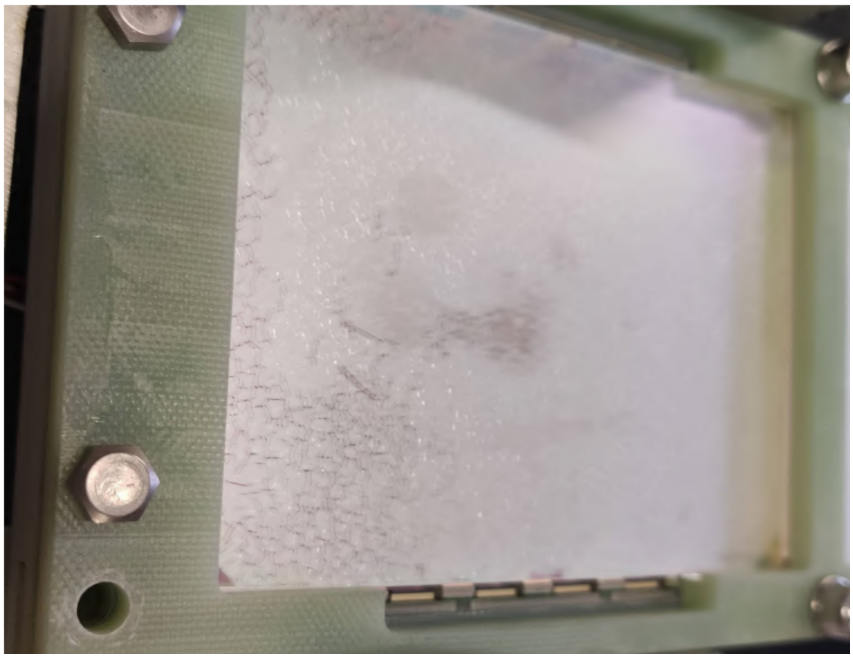

Figure 3.10: Micro-cracks in the PTP wavelength shifter deposition after several thermal cycles.

3.3 Waveshape Analysis

This section describes the waveshape analyzes from the signals generated in the X-ARAPUCA experimental test. The analyzes determines the parameters of equation 2.16 for the LAr scintillation due to alpha particles for the first time.

3.3.1 Signal Response of the X-ARAPUCA

The signal waveshape detected by the experimental set up is not simply the light emission distribution of Liquid Argon (Eq. 2.16). The SiPM inside the X-ARAPUCA affects the final waveshape recorded by the experiment.

According to Signal Processing Theory [60], the signal waveshape detected by the experiment is the convolution of the physical signal with the electronic response of the detector, the SiPM in this case.

To fit the light emission of LAr proposed by Segreto [47], it is necessary to create a full model of the observed signal, taking into account the electronic response of the SiPM inside the X-ARAPUCA, this is represented in equation Eq. 3.4:

$$S_{Obs}(t|\theta_i) = \int S_{phys}(\tau|\theta_i)R(t-\tau)d\tau \equiv (S_{phys} \circledast R)(t) \tag{3.4}$$

S_{Obs} is the observed signal in the experiment, depending on the time t and the model parameters θ_i, S_{phys} is the actual physical signal (Eq. 2.16), and R is the electronic response.

The electronic response of a system can be characterized by evaluating how it responds to a single pulse signal, in the case of light detection, the single pulse scenario is the detection of a single photon.

This means that the electronic response of the SiPM in the X-ARAPUCA is the signal it produces in a Single Photon Electron (SPhE) event.

The models for the electronic response of SiPM are too complicated to be included as a part of another model [61], and effective models using exponential weren't good in preliminary analyzes.

Instead of a model of the shape of a SPhE, the average waveform from multiple Single Photon events was used in the analyzes. The waveshapes were selected by charge from the calibration data, shown in figure 3.11, the acceptance window was between 2 and 3 standard deviations from the charge generated by single photon, depending on the run and the amount of statistics available.

The standard deviations for the charge of a SPhE were determined in the calibration process in subsection 3.2.1. The resulting average waveshape is shown figure 3.12. This will be the waveshape data used in the analyzes.

3.3.2 Waveshape Model

To create a full picture of the detected waveshape it's necessary to include all the effects related to light emission and detection in the system. The computational model for light detection in this experimental set up consists of the liquid argon scintillation light

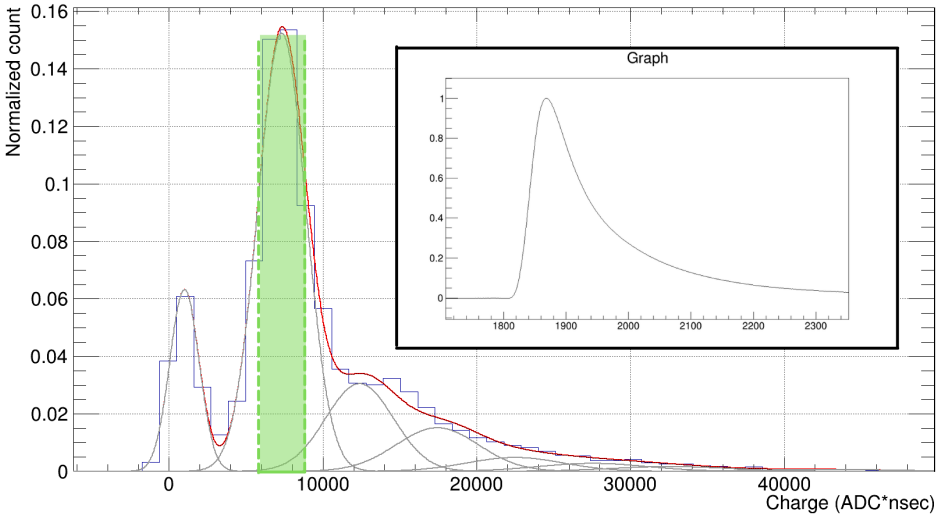

Figure 3.11: Acceptance window for Waveshapes of a single photon electron in green. The region was 2 to 3 standard deviations from the mean charge, depending on the statistics available. The average SPhE waveshape is calculated as the average of the selected signals, the result is shown in the top-right of the image.

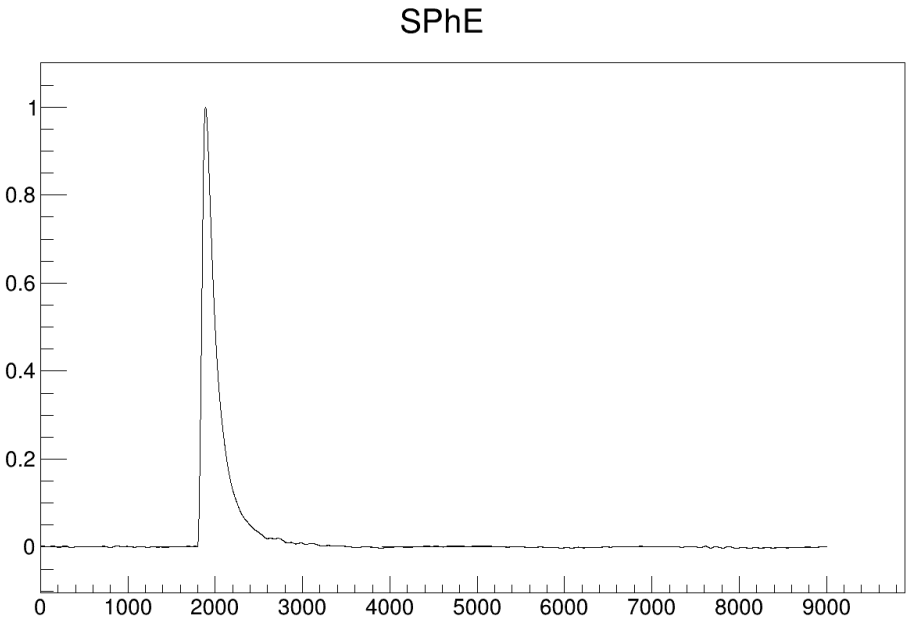

Figure 3.12: Average signal for the single photon electron of a SiPM, representing it's electronic response.

model, the electronic response and an additional term due to the effects of the wavelength shifter.

The liquid argon light model is in equation 2.16, as the electronic response is discussed in the previous subsection (3.3.1).

The last component is the delayed light due to the wavelength shifters in the X-ARAPUCA module, more precisely, the PTP wavelength shifter has two emissions times, a short one (few nanoseconds) and a slower one ($50 - 100\ ns$), called delayed emission.

The delayed emission from PTP wavelength shifter creates ambiguity between the fast and slow components of LAr Scintillation. To compensate for that, a third exponential decay is added to the signal model. The shape of the delayed PTP emission is not an exponential decay, but it's contribution to the total light is small enough (lower than 10%) that it can be approximated as a exponential decay.

The light emission model, including the emission by LAr and the delayed light from the PTP is in equation 3.5:

$$l(t|t_0,\tau_s,\alpha_s,\tau_{ptp},\alpha_{ptp},\tau_3,\alpha_3,k,q) = \frac{\alpha_s}{\tau_s}e^{(t-t_0)/\tau_s}+\frac{\alpha_{ptp}}{\tau_{ptp}}e^{-(t-t_0)/\tau_{ptp}}+\frac{\alpha_3}{\tau_3}\frac{e^{-(t-t_0)/\tau_q}}{1+q\tau_q(1-e^{-(t-t_0)/\tau_q})}, \tag{3.5}$$

the parameters in Eq. 3.5 are the same as in Eq. 2.16 with the addition of t_0 as the starting time for the signal, α_{ptp} and τ_{ptp} for the abundance and characteristic time of the delayed PTP light respectively.

The last effect on the original light signal that must be taken into accord is the effect of nitrogen contamination in LAr. Nitrogen is a common contaminant in Argon (gas or liquid) and can cause de-excitation of excited dimers, reducing the total light yield and slow emission times

The N_2 concentration can be estimated by the value of the slow component, since its presence affects it directly [46], so it must be noted that in the fitting process of the waveshape the values of the parameters associated with the slow time (t_3 and k^+) might be affected by it. The effect of N_2 in the slow time could be modeled, but the final model would be too complicated and have too many parameters, making the fit less reliable.

With all that in mind, the computational model for the observed light signal in the experiment is the discrete convolution of the produced light signal in equation 3.5, and the average SPhE signal generated by the electronic response in figure 3.12. The mathematical model can be written as:

$$\begin{aligned} S(t|\theta_i) = l(t|\theta_i) \circledast R[t] &\approx \sum_{t_i} l(t-t_i)R[t_i] \\ \theta_i &= \{t_0,\tau_s,\alpha_s,\tau_{ptp},\alpha_{ptp},\tau_3,\alpha_3,k^+,q\}, \end{aligned} \tag{3.6}$$

where θ_i represent all the parameters as written, t_i are the sampled times, in this experiment the time step is 2 ns, so $t_i = 2 * i$ ns, $l(t|\theta_i)$ is the computational model for the light signal, with $l(t-t_i)$ being the value of the model at the time $t-t_i$, and $R(t)$ is the electronic response. In the discrete convolution we are using the experimentally measured electronic response, thus we only have its values at sample times $R[t_i]$.

3.3.3 Waveshape Fit and Results

The goal is to estimate the parameters of the model in equation 3.6 by fitting it into the waveshape generated by an alpha signal.

To generate a low noise waveshape, the average waveshape from multiple alpha signals

is taken, following some criteria to ensure the waveshape is representative of a single alpha event:

- The waveshape can't be saturated (some signals generated more charge that can be measured by the ADC). This has no effect in the fit results, since the amount of charge only affects the scale of the signal, not the abundance of fast and slow components or any other parameter related to the waveshape.
- The waveshape has to have a single clear peak with no other comparable peak. This selection happens with the help of the TSpectrum Root Class [58],
- The peak position of the waveshape must be close to the mean peak position in relation to the other selected peaks.

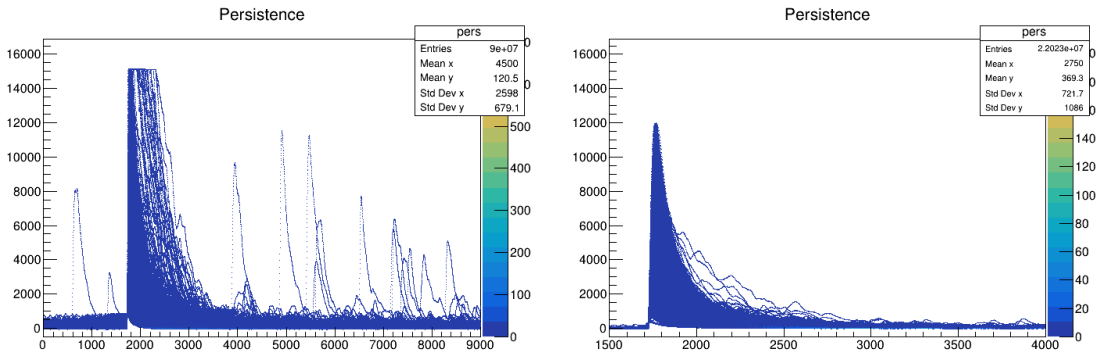

Figure 3.13: Left: Waveshapes before the first to criteria were applied. Right: Waveshapes after the criteria are applied - No more saturated signals, all signals starting at the same time and with a single clear peak.

The results of the selection are shown in figure 3.13. The average is taken after setting the peak value of each waveshape to 1 *a.u.* (arbitrary units).

To determine the parameters of Eq. 3.6, we minimize the χ^2 of the difference between the computational model and the average experimental LAr Signal. One additional scale parameter is added to help the fit:

$$\chi^2(\theta_i) = \sum_{t_i} \left(\frac{(S_{cale} \cdot S(t_i|\theta_i) - D[t_i])^2}{D[t_i]} \right)$$
$$\theta_i = \{t_0, \tau_s, \alpha_s, \tau_{ptp}, \alpha_{ptp}, \tau_3, \alpha_3, k^+, q, S_{cale}\}. \tag{3.7}$$

The χ^2 function in Eq. 3.7 is minimized using the TMinuit class in the ROOT framework [58] resulting in values for the parameters.

Notably our interests lie in the relative abundance of single and triplet states for alpha particles. For alpha particle this value was measured around 71% fast emission in previous experiments [35].

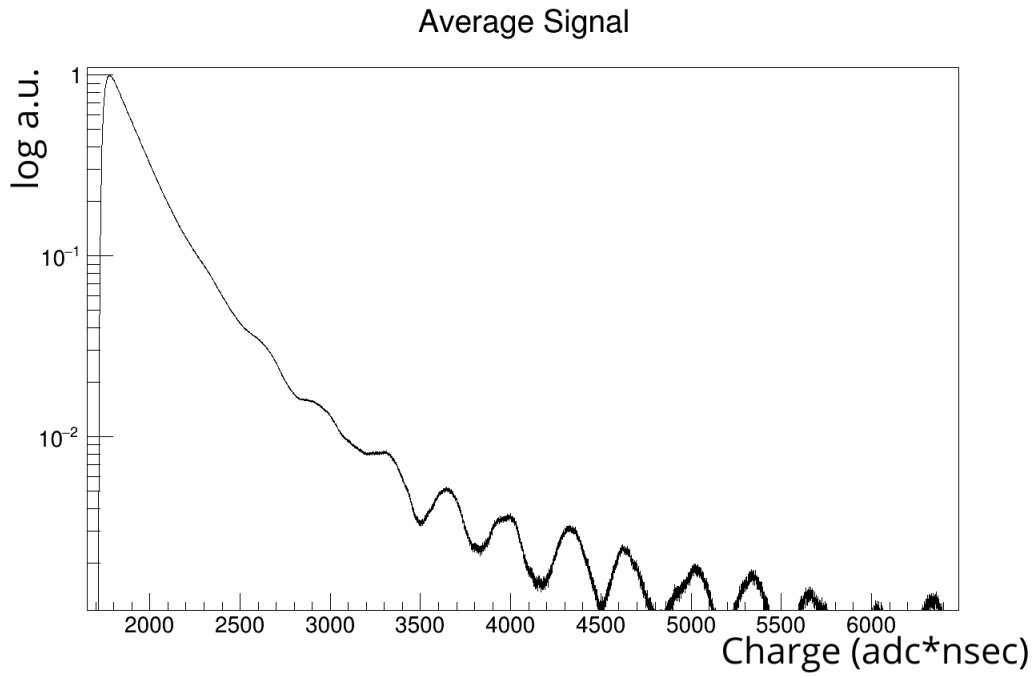

Figure 3.14: Average Signal from LAr Scintillation with the Alpha Source, the averaged signals were the ones selected as shown in figure 3.13. The periodic noise in the tail of the signal was identified as electric interference due to bad wiring in the laboratory and fixed for the future tests.

The fits with the proposed model are consistent with this value, suggesting that the model parameters are representative of the physics behind LAr Scintillation with alpha particles. An example of the fit result is shown in figure 3.15.

The result for the fits for 5 different voltage biases can be seen in table 3.3. The table omits the parameters of the initial time and scale, since they have little physical meaning.

The values for the PTP related parameters are also not representative of any physical property, since the model uses an effective decay time, the contributions of the PTP intermediate component were around $3 - 10\%$ with a decay time around $100 - 200\ ns$.

The value of the fast decay time (singlet component) is also omitted since it's significantly affected by the presence of nitrogen contaminants and the PTP delayed signal, but it's usually fitted between $1 - 20 nsec$.

Bias ($\pm 0.2V$)	46.5	47.0	47.5	48.0	48.5
$\alpha_s(\pm 5\%)$	75%	71%	70%	62%	63%
$\alpha_3(\pm 5\%)$	25%	29%	30%	38%	37%
$\tau_3(\pm 50\ ns)$	900	811	950	820	835
$k^+(\pm 0.5 \times 10^{-4} nsec^{-1})$	1.5×10^{-4}	2.9×10^{-4}	2.1×10^{-3}	1.3×10^{-3}	1.3×10^{-3}
$q(\pm 0.5 \times 10^{-4} nsec^{-1})$	3.6×10^{-4}	4.0×10^{-4}	3.9×10^{-4}	3.9×10^{-4}	3.9×10^{-4}

Table 3.3: Table of fit results for 5 different biases for alpha particles. The relative abundance of triplet and singlet states is consistent with what is expected, this is the first time that the values of the quenching parameters k^+ and q are determined for alpha particles.

The fit is an improvement in relation to models that don't include quenching effects in liquid argon emissions, indicating that the quenching effects are important to the light emissions in LAr.

The results for alpha particles are shown with previous results from neutrons and gammas are shown in the table 3.4.

This is the first time that the parameters in equation 2.16 are determined for alpha particles.

- k^+ associated with the quenching process $Ar_2^* + Ar_2^+ \rightarrow Ar_2^+ + 2Ar$
- q associated with the quenching process $Ar_2^* + Ar_2^* \rightarrow Ar_2^* + 2Ar$

Bias ($\pm 0.2V$)	**alpha**	gamma	neutron
$\alpha_s(\pm 5\%)$	70%	14%	64%
$k^+(\pm 0.5 \times 10^{-4} nsec^{-1})$	2.1×10^{-3}	1.3×10^{-4}	0
$q(\pm 0.5 \times 10^{-4} nsec^{-1})$	3.9×10^{-4}	2.3×10^{-4}	2.3×10^{-3}

Table 3.4: Current results for the parameters of the LAr emission model in Eq. 2.16 for alpha, gamma and neutrons [47].

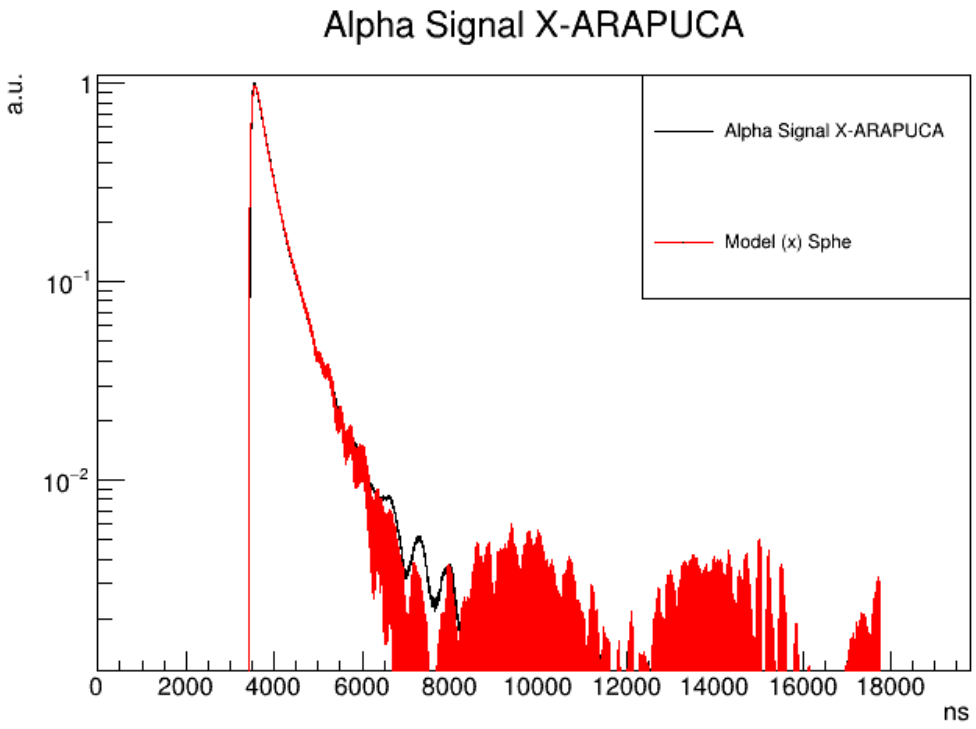

Figure 3.15: Result of the fit (in red) for one of the 48.5V bias run, using equation 3.6 as the model. The noise in the fit is the result of representing the SPhE waveshape with experimental data.

Chapter 4

Light Yield and Waveshape Analysis in Xenon doped Liquid Argon

The first section of the chapter will describe the most relevant properties of Xenon doped LAr and the model for energy transfer and scintillation proposed by Segreto, 2020 [47].

The second section of this chapter is about the results from a study of Xenon Doped Liquid Argon done at Building 182 at CERN in late 2019.

The motivation for the study was twofold. Firstly there are observations of Xenon Doped Argon that aren't well explained, such as the increased light yield and the energy transfer mechanism from LAr to Xenon [47].

Another goal is to be a preliminary experiment for larger tests at the ProtoDUNE. An accident in 2019 resulted in the contamination of the LAr in ProtoDUNE with large quantities of nitrogen, causing the degradation of the light signal [62].

The idea of doping the impure argon with xenon was proposed as a way to recover the light yield lost due to the nitrogen contamination, apart from other physical motivations.

The experiment with xenon doped argon in Building 182 served as a way to evaluate how much xenon was needed to recover the light yield and if a larger scale test in ProtoDUNE was viable.

4.1 Properties do Xenon doped Liquid Argon

Liquid Xenon is a noble gas with two decay components, the fast one around 4 ns and the slow one around 22 ns, significantly faster than the LAr slow decay time. Doping LAr with small quantities of Xenon actually suppresses the long slow component of LAr creating a faster signal, that could be used to have increased counting rate in LAr based experiments [63]. Not only that, the doping actually converts a significant portion of the LAr 127 ns light into the wavelength emitted by Xenon at 174 ns, a longer wavelength, easier to detect.

In high enough concentrations (several parts per million) it's also possible to have better pulse shape discrimination based on the F_{prompt} parameter described in the last chapter [64].

Properties like this make xenon doped LAr an interesting possibility for experiments in neutrino physics.

The reported increase in light yield due to doping and the shift to the 174 ns wavelength will be evaluated in the experiment described and in the later portion of this chapter. Before that this section will deal with the possible mechanism behind it.

4.1.1 Mathematical Model for Scintillation

The light wavelength shift from 127 nm to 174 nm in xenon doped LAr is well established, as well as an almost total suppression of the slow component. An increased light yield has also been reported that can't be explained by the better conversion efficiency of wavelength shifters at the xenon wavelength. This results indicate that a significant portion of the energy deposited by an ionizing particle in LAr is transferred to Xenon, including possibly a fraction of the energy that would be quenched.

The mechanism for that energy transfer proposed by Segreto, 2020 [47] is:

$$Ar_2^* + Xe \rightarrow (ArXe)^* + Ar \tag{4.1}$$

$$(ArXe) + Xe \rightarrow Xe_2^* + Ar. \tag{4.2}$$

The energy transfer chain in equations 4.1 and 4.2 succeed by the decay of the excited dimer of xenon could compete with the quenching of the LAr light described in subsection 3, resulting in a shift of the slow LAr scintillation component to the xenon one and a recovery of some of the light that would be quenched.

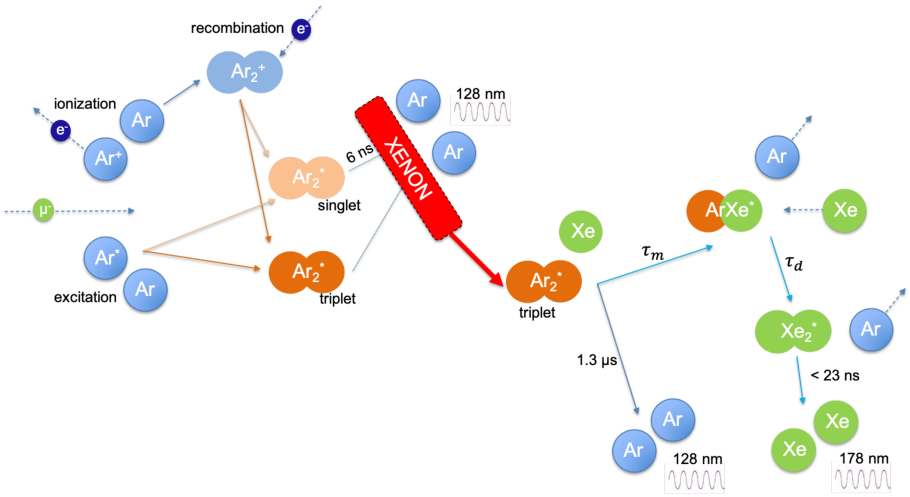

Figure 4.1: Mechanism for energy transfer between argon and xenon. The process occurs in two steps, in the first one the energy is transferred to a mixed dimer ($ArXe^*$), and then to a pure xenon dimer (Xe_2^*), that then decays emitting light.

In order to model this energy transfer and the light emission process, some approximations are in order. For high enough concentrations, it should be possible to neglect second order quenching effects (between $Ar_2^* - Ar_2^*$, $Ar_2^* - (ArXe)^*$, $(ArXe)^* - (ArXe)^*$), it's also

assumed that the energy transfer happens without loss, and the reaction rate in equations 4.1 and 4.2 happen at the same rate k_{Xe}. It's also assumed that diffusion is neglectable. Let $N_3^{Ar}(t)$ be the concentration of argon excited dimers, $N^{Xe}(t)$ the concentration of excited xenon dimers and $N^{ArXe}(t)$ the concentration of mixed dimers:

$$\frac{dN_3^{Ar}}{dt} = -\lambda_3 N_3^{Ar}(t) - k^+ N_3^{Ar}(t) - k_{Xe}[Xe]N_3^{Ar}(t) \tag{4.3}$$

$$\frac{dN^{ArXe}}{dt} = -k_{Xe}[Xe]N^{ArXe}(t) + k_{Xe}[Xe]N_3^{Ar}(t) \tag{4.4}$$

$$\frac{dN^{Xe}}{dt} = -\lambda_{Xe}N^{Xe}(t) + k_{Xe}[Xe]N^{ArXe}(t), \tag{4.5}$$

in which λ_3 is the inverse of the triplet decay time in argon, $[Xe]$ is the xenon concentration and λ_{Xe} is the inverse of the decay time for xenon triplet dimers, k^+ is the factor for quenching if ionized dimers, as in equation 2.10 . With initial conditions of $N^{ArXe}(0) = 0$, it's possible to solve the equations assuming $\lambda_{Xe} >> k_{Xe}[Xe]$. Define:

$$\begin{aligned} \lambda_d &= 1/\tau_d \equiv k_{Xe}[Xe] \\ \lambda_q &= 1/\tau_q \equiv \lambda_3 + k^+ \\ \lambda_r &= 1/\tau_r \equiv \lambda_d + \lambda_q. \end{aligned} \tag{4.6}$$

With this definitions, the equation 4.3 can be written as:

$$\begin{aligned} \frac{N_3^{Ar}}{dt} &= -\lambda_3 N_3^{Ar} - k^+ N_3^{Ar} - \lambda_d N_3^{Ar} \\ \frac{N_3^{Ar}}{dt} &= -(\lambda_3 + k^+\lambda_d)N_3^{Ar} \\ \frac{N_3^{Ar}}{dt} &= -\lambda_r N_3^{Ar} \\ \text{So, } N_3^{Ar}(t) &= N_0 e^{-\lambda_r t}, \end{aligned} \tag{4.7}$$

this can be used in equation 4.4:

$$\frac{dN^{ArXe}}{dt} = -\lambda_d N^{ArXe}(t) + \lambda_d N_3^{Ar}(t). \tag{4.8}$$

Since N_3^{Ar} is an exponential with λ_r, the solution is the sum of the homogenous equation plus N_3^{Ar}, $N^{ArXe}(t) = Ae^{-\lambda_d t} + Be^{-\lambda_r t}$, together with the initial condition

$N^{ArXe}(0) = 0 = A + B$, so $A = -B$. With that one can write equation 4.8 as:

$$\begin{aligned}
\frac{dN^{ArXe}}{dt} + \lambda_d N^{ArXe} &= \lambda_d N_3^{Ar} && \text{|Writting the exponential} \\
-\cancel{\lambda_d A e^{-\lambda_d t}} + \lambda_r A e^{-\lambda_r t} + \lambda_d(\cancel{A e^{-\lambda_d t}} - A e^{-\lambda_r t}) &= \lambda_d N_0 e^{-\lambda_r t} && \text{|Organizing} \\
A(\lambda_r - \lambda_d)\cancel{e^{\lambda_r t}} &= \lambda_d N_0 \cancel{e^{\lambda_r t}} && \text{|}\lambda_r - \lambda_d = \lambda_q \\
A &= \frac{\lambda_d N_0}{\lambda_q}.
\end{aligned} \tag{4.9}$$

Using $B = -A$, N^{ArXe} can be written as:

$$N^{ArXe}(t) = \frac{\lambda_d N_0}{\lambda_q}(e^{-\lambda_d t} - e^{-\lambda_r t}), \tag{4.10}$$

with that, the last equation can be solved, 4.5:

$$\frac{dN^{Xe}(t)}{dt} + \lambda_{Xe} N^{Xe}(t) = \lambda_d N^{ArXe} = N_0 \frac{\lambda_d^2}{\lambda_q}(e^{-\lambda_d t} - e^{-\lambda_r t}). \tag{4.11}$$

The proposed solution for this equation is the homogeneous solution (right side of Eq. 4.11 = 0) plus the exponential terms from N^{ArXe} , so $N^{Xe}(t) = Ae^{-\lambda_{Xe} t} + Be^{-\lambda_d t} + Ce^{-\lambda_r t}$. Similar to Eq. 4.9 the term with the exponential on λ_{Xe} is 0 by construction (it's the solution to the left side of the equation), leaving only:

$$B(-\lambda_d + \lambda_{Xe})e^{-\lambda_d t} + C(-\lambda_r + \lambda_{Xe})e^{-\lambda_r t} = N_0 \frac{\lambda_d^2}{\lambda_q}, \tag{4.12}$$

since the exponentials are independent, it's possible to separate the constants B and C:

$$\begin{aligned}
B(\lambda_{Xe} - \lambda_d) &= N_0 \frac{\lambda_d^2}{\lambda_q} \\
B &= N_0 \frac{\lambda_d^2}{\lambda_q} \frac{1}{\lambda_{Xe} - \lambda_d}.
\end{aligned} \tag{4.13}$$

Using $\lambda_{Xe} >> k_{Xe}[Xe] = \lambda_d$ for the B and C constants:

$$B \approx N_0 \frac{\lambda_d^2}{\lambda_q \lambda_{Xe}} \tag{4.14}$$

$$C \approx -N_0 \frac{\lambda_d^2}{\lambda_q \lambda_{Xe}}. \tag{4.15}$$

With that and $A = N^{Xe}(0) = N_0^{Xe}$ the solutions for equations4.3, 4.4 and 4.5 can be written in terms of characteristic time:

$$N_3^{Ar}(t) = N_0 e^{-t/\tau_r} \tag{4.16}$$

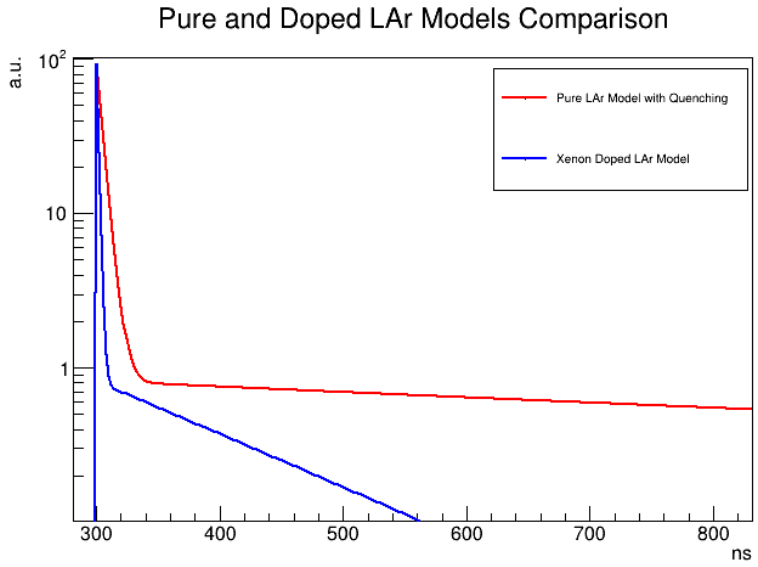

Figure 4.2: Graph of the model for light scintillation for xenon doped liquid argon in comparison with the pure LAr model, both proposed by Ettore [47]. There is a clear shortening of the signal with the Xenon involved.

$$N^{ArXe} = N_0 \frac{\tau_q}{\tau_d}(e^{-t/\tau_d} - e^{-t\tau_r}) \tag{4.17}$$

$$N^{Xe}(t) = N_0^{Xe} e^{-t/\tau_{Xe}} + N_0 \frac{\tau_q \tau_{Xe}}{\tau_d^2}(e^{-t/\tau_d} - e^{-t\tau_r}). \tag{4.18}$$

It's assumed that the dimer $ArXe$ does not scintillate in any relevant way, so only equations 4.16 and 4.18 will contribute to the light emission from triplet states, that is:

$$l(t) = \frac{\alpha_s}{\tau_s} N_s(t) + \frac{\alpha_3}{\tau_3} N_3(t) + \frac{\alpha_3}{\tau_{Xe}} N_3^{Xe}(t), \tag{4.19}$$

with $l(t)$ being the light emission probability at time t, $N_s(t)$ being the number density of singlet states, τ_s being it's characteristic time. Writing each of the terms in Eq. 4.19:

$$l_s(t) = \frac{\alpha_s}{\tau_s} e^{-t/\tau_s} \tag{4.20}$$

$$l_3(t) = \frac{\alpha_3}{\tau_3} e^{-t/\tau_r} \tag{4.21}$$

$$l_{Xe}(t) = \frac{\alpha_3}{\tau_{Xe}} \frac{\tau_q \tau_{Xe}}{\tau_d^2}(e^{-t/\tau_d} - e^{-t/\tau_r}) = \alpha_3 \frac{\tau_q}{\tau_d^2}(e^{-t/\tau_d} - e^{-t/\tau_r}), \tag{4.22}$$

with $1/\tau_d = k_{Xe}[Xe]$. The fast scintillation is assumed not to be affected by the energy transfer to xenon, the signal shape from Eq. 4.19 is shown in figure 4.2. Integrating for the light yield parameter:

$$L = \alpha_s + \alpha_3 (\frac{\tau_r}{\tau_3} + \frac{1/\tau_d}{1/\tau_d + 1/\tau_q}). \tag{4.23}$$

4.2 Relative Light Yield and Scintillation Analysis

4.2.1 Experimental Motivation in the context of ProtoDUNE

ProtoDUNE-SP is a single phase (SP) DUNE Far Detector (Section 1.4) prototype constructed and operated at CERN Neutrino Platform (figure 4.3). The ProtoDUNE is a crucial part of the DUNE effort towards the construction of the $10 - kt$ fiducial mass far detector modules [65]. The goal of the ProtoDUNE is to test the physics, operational capabilities and long term stability in the operation of a large scale LArTPC, in preparation for the larger DUNE LArTPCs.

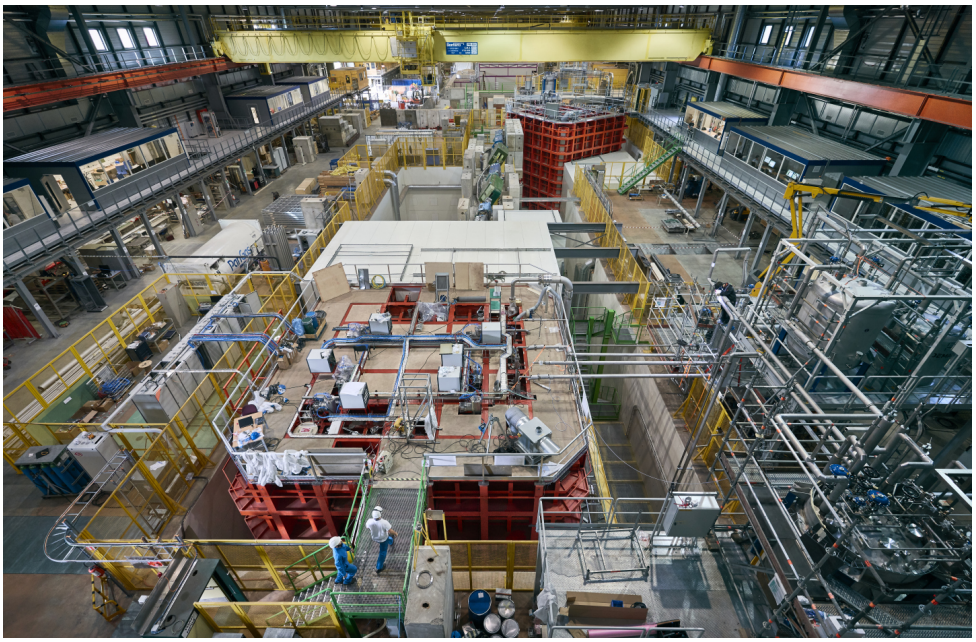

Figure 4.3: ProtoDUNE-SP in the Neutrino Platform at CERN

The ProtoDUNE-SP is a LArTPC with dimensions $6m \times 7m \times 7.2m$ placed inside a cryostat at cryogenic temperatures of 89 K. A dedicated beamline at CERN is used as the source of charged particles to run tests with ProtoDUNE-SP detector.

One of the tests planned for the ProtoDUNE-SP in 2020 was doping the argon in the detector with Xenon. The goal was to study the long term stability and uniformity of the LArTPC with xenon doped LAr. This test would also allow to study the suppression of the slow component of LAr due to xenon doping, as well and the light conversion from the $127nm$ argon light to the $174nm$ Xenon light.

The plans for this test changed in July of 2019, when a gas pump fail injected atmospheric air in the system, the filters exhausted and air mixed with pure LAr. This created a severe contamination of oxygen (O_2) and nitrogen (N_2), causing a degradation of the charge and light signal in the ProtoDUNE-SP detector [62].

The charge signal was recovered after the regenerated filters removed the O_2 from the argon. But nitrogen can't be purified out of argon, the presence of nitrogen causes a reduction in light yield by dexciting the argon dimers (quenching), it also shortens the slow component of LAr.

With the accident in mind, another possible use of xenon doping in LAr was proposed: recovering the light yield in the light signal by adding xenon to the nitrogen contaminated LAr. The idea is that the energy transfer process between Xenon and Argon (Eq. 4.1-4.2) could compete with the quenching due to the presence of nitrogen, resulting in the emission of more light even with the contamination.

At the time of this proposal it was not known how much xenon was needed to recover the light signal, if the xenon concentrations required were too large, the test might not be viable due to the high cost of xenon. To make sure that this new Xenon Doping test at the ProtoDUNE-SP was indeed viable, preliminary tests in a smaller set up were planned.

The test described in the rest of this section is the preliminary xenon doping test at Building 182 at CERN in late 2019 (figure 4.4).

The test at Building 182 had as a goal to establish which Xenon concentrations was needed to recover the light signal in LAr contaminated by nitrogen, and by that establish the viability of a larger scale test at the ProtoDUNE-SP. I took part in running the test, collecting data and doing analyses of the relative light yield due to the doping on xenon and nitrogen in LAr, as well as providing my knowledge of the X-ARAPUCA light detectors used in this test.

4.2.2 Experimental Set Up and Calibration

This subsection describes the experimental set up and calibration process of the preliminary Liquid Argon Doping test for the ProtoDUNE-SP Xenon Doping test in late 2020. The experiment happened at Building 182 at CERN.

The experimental set up is very similar to what is described in subsection 3.1 with a few differences.

There was a setup for controlled injection of nitrogen and xenon. There also was an alpha source available inside the dewar, but most of the data were collected with cosmic muons, as shown in figure 4.6.

The data collection relied on a coincidence from both internal light collectors and cosmic pads outside the dewar. Three cosmic paddles were available (4.6), and a fourth one was added for Run 2.

The digitalization frequency of the light waveforms was of $150Mhz$ resulting in time steps of 6.666... ns.

Inside of the dewar there were 4 X-ARAPUCAs with 2 arrays of SiPM each, totalling 8 channels. The first two X-ARAPUCAs (Channels 0 to 3) were covered with a quartz glass that was opaque to the light emitted by argon (127 nm) but transparent (85% transmissivity) to the light produced by Xenon ($174nm$). The other two X-ARAPUCAs (Channels 8 to 11) had no quartz cover, so they detected both argon and xenon scintillation light, as in figures 4.7 and 4.8. The data from the X-ARAPUCAs waveforms were digitized with a custom SiPM Signal Processor (SSP).

Channel 3 stopped producing data in the first week of the experiment, so the analysis doesn't include information from this channel.

For calibration purpose there was a LED source connected to the dewar with a optical fiber cable. The UV LED source light was about $200nm$ wavelength, and it was powered

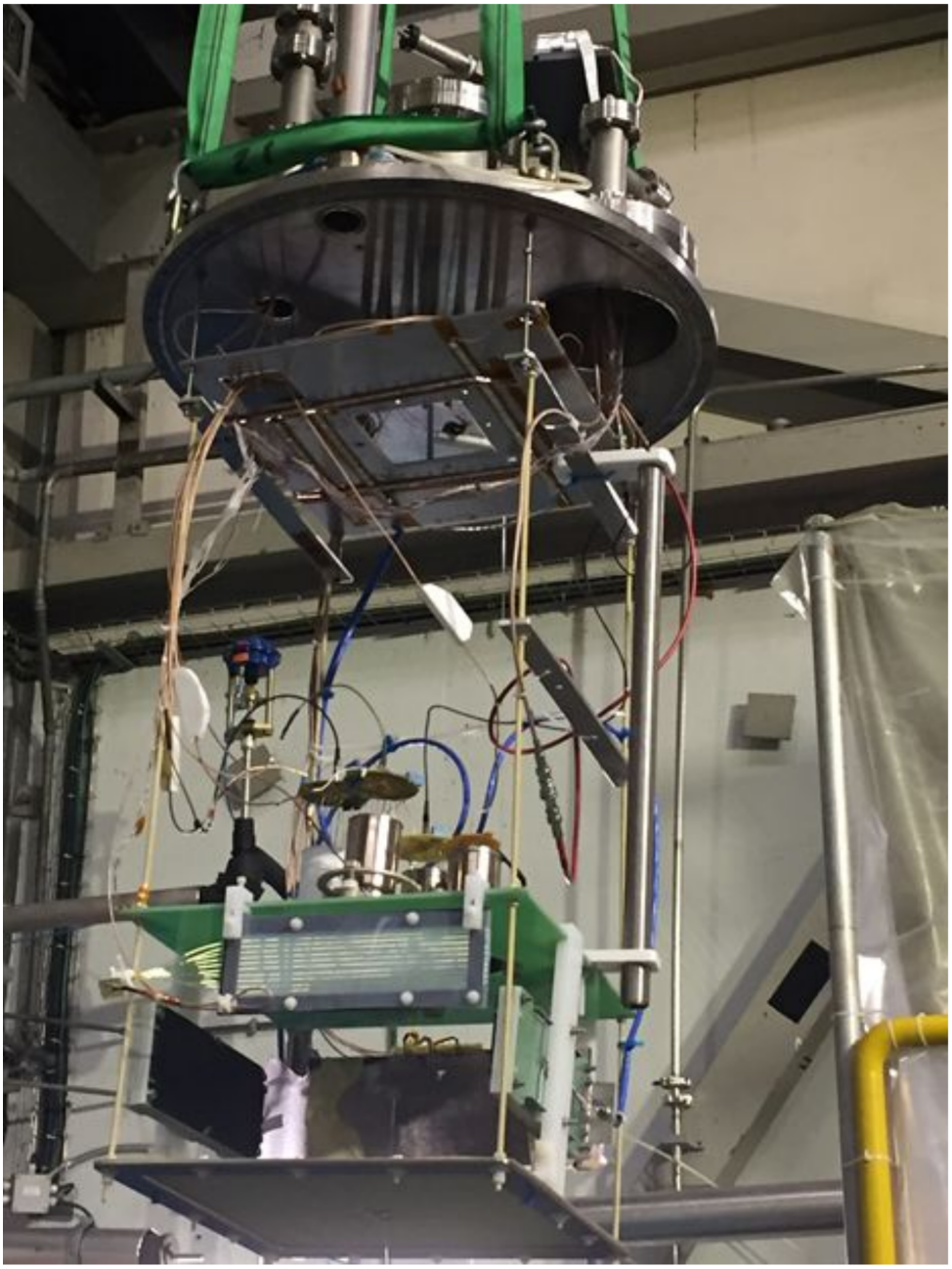

Figure 4.4: Preliminary experiment at Building 182 CERN being set up

with a pulse generator.

The calibration process was identical to that of subsection 3.1 , with the multigaussian fit of the charge distribution from signals with few photons, as in figure 4.9. Each Gaussian peak represents a number of photons, the charge gained by a single photon is the difference between the single photon peak and two photon peak.

The average single photon electron was also constructed in a similar way, taking the average from waveshapes that have the expected charge for a single photon.

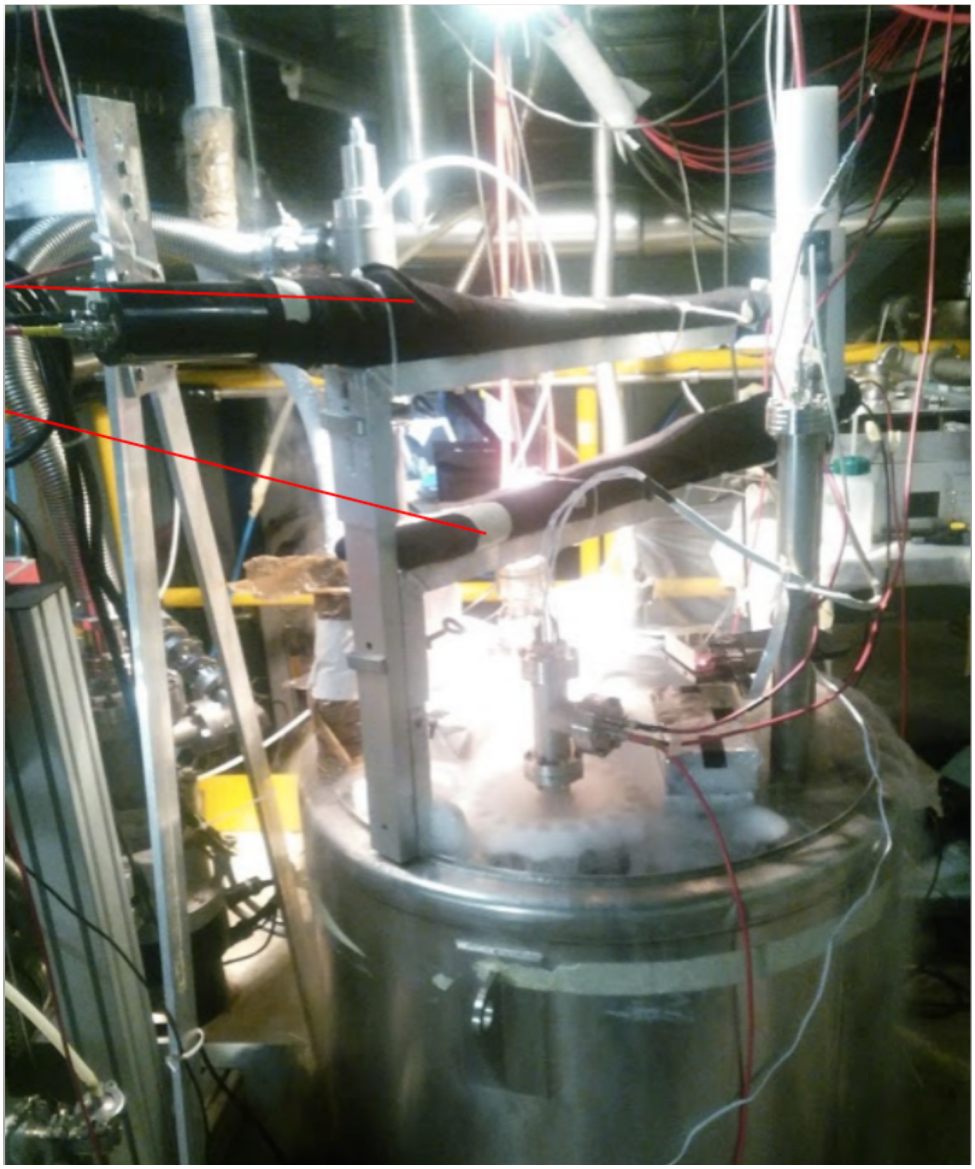

Figure 4.5: Cryogenic dewar in the test at Building 182 at CERN

4.2.3 Doping Schedule and Goals

The experiment set up in Building 182 had two runs with different doping schedules and goals.

Run 1 happened in the last weeks of November 2019, after the experiment was set up and a calibration run using the LED as the source was made. The doping schedule was:

1. Pure LAr cosmic trigger data collection
2. Dope with nitrogen until the light signal degradation looks the same as the Proto-DUNE accidental contamination with nitrogen (subsection 4.2.1), around $5.7 ppm$.
3. Do a cosmic trigger data collection with nitrogen doped liquid argon
4. Three steps of adding 10ppm of xenon and doing a cosmic run

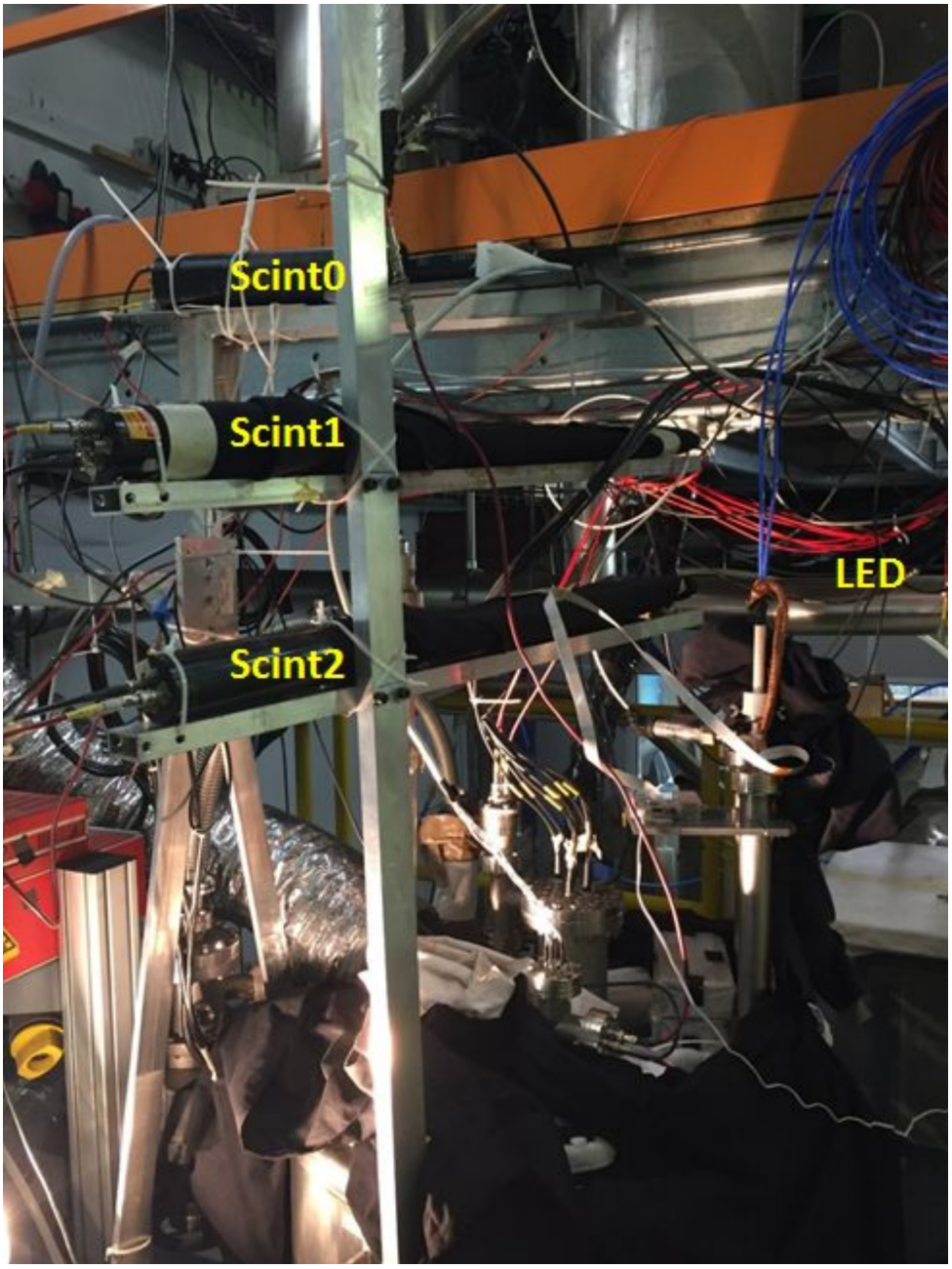

Figure 4.6: Cosmic Paddle Set Up for the experiment

Run 1 resulted in having data from cosmic trigger runs with pure LAr, LAr plus nitrogen, and LAr plus nitrogen plus 10/20/30ppm of Xenon. This data were used to evaluate the relative light yield of pure and contaminated LAr, and how much of the original light yield was recovered by adding xenon. It was also possible to do a first estimation of light conversion due the presence of Xenon in the mix, comparing the relative light yield of the X-ARAPUCAs with and without quartz window.

Run 2 happened in the first couple of weeks of December 2019. The doped LAr was dumped and the dewar was filled with a new batch of pure liquid argon. In the doping schedule of Run 2, the order of Xenon and Nitrogen doping was inverted, the doping schedule was:

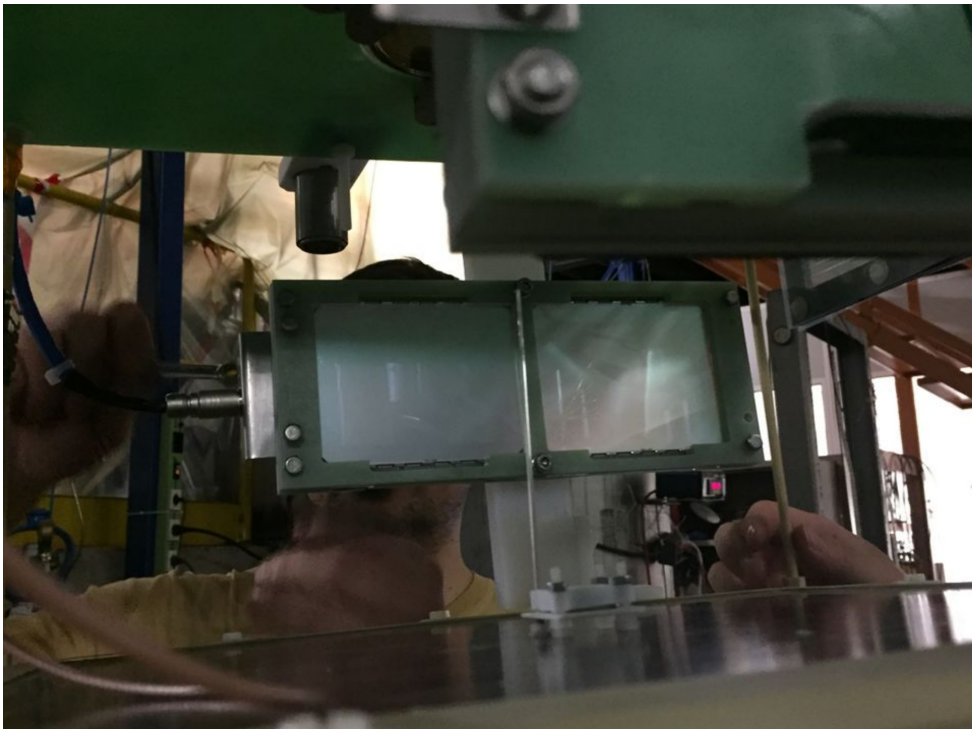

Figure 4.7: Installation of the X-ARAPUCAs in the experimental set up

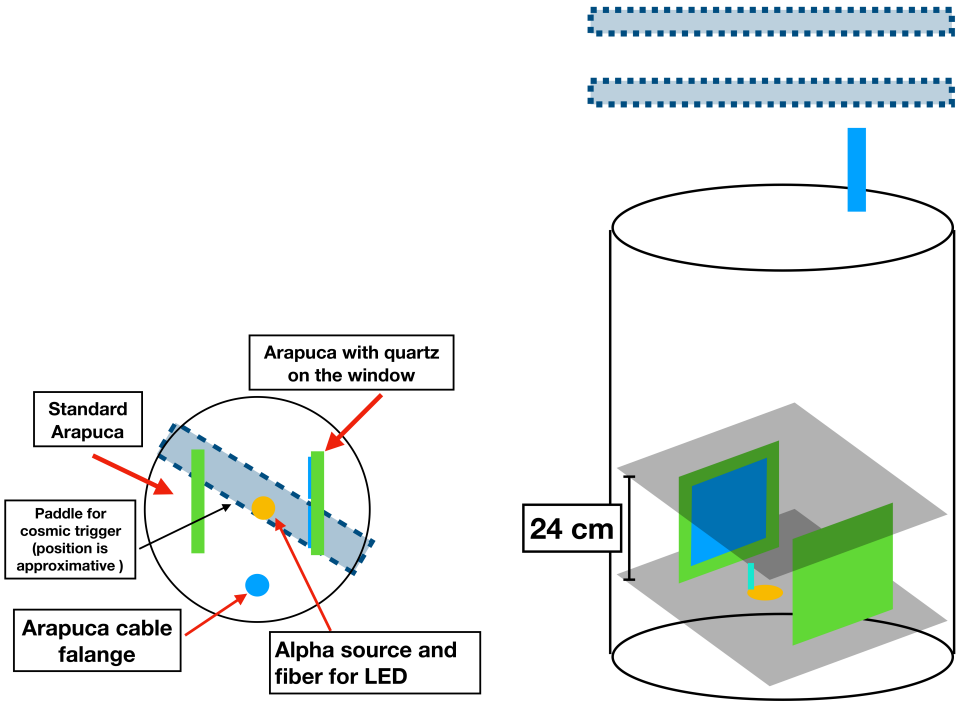

Figure 4.8: Right: Top view of the dewar with cosmic paddles and X-ARAPUCAs, the quartz windows are represented in blue. Left: Side view of the dewar setup with the cosmic paddles above it.

1. Pure LAr cosmic trigger data collection

2. Three steps of adding 10ppm xenon to Lar followed by cosmic trigger runs in each

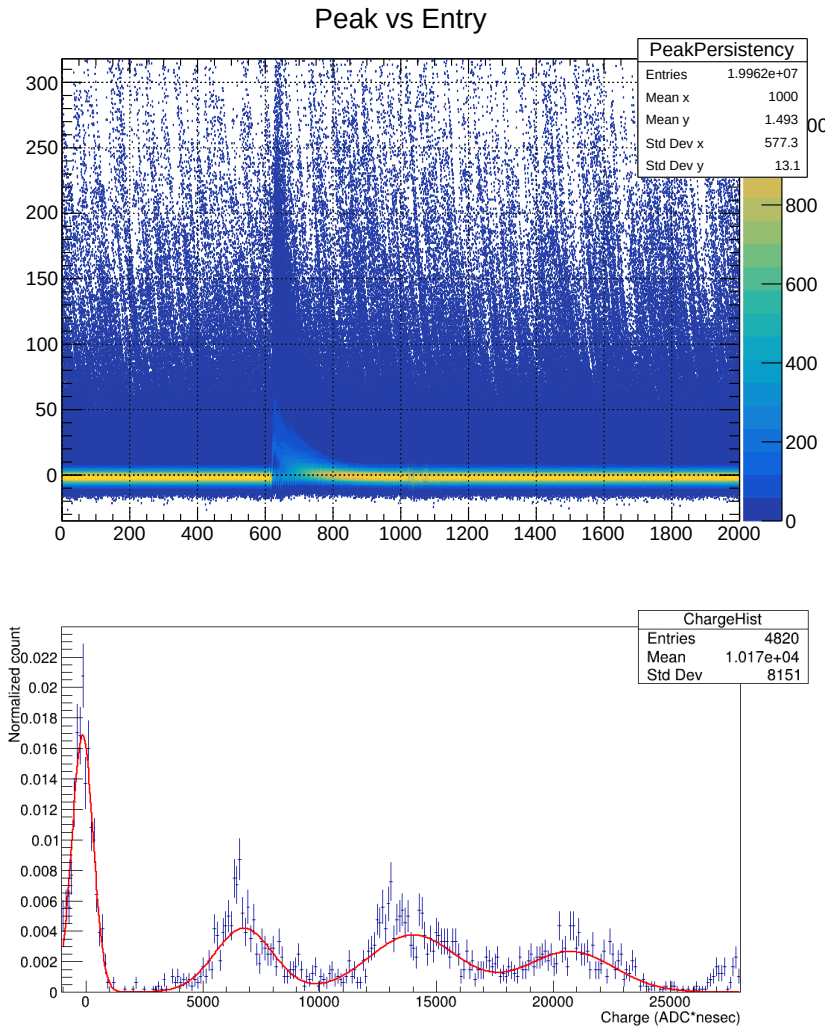

Figure 4.9: Top: persistence of low light signals, the single photon electron is the shape in the lighter blue. Bottom: example of fitted multi Gaussian shape from the charge histogram of low light signals.

step

3. Adding around 5.7*ppm* of N_2 to the Xenon Doped LAr

4. A final cosmic trigger run with the full mixture

The data in run 2 gives the information about a mixture of LAr and Xenon without the contamination of nitrogen, it allowed for the analyses of the possible increase in light yield observed in Xenon doped LAr [47]. It also allowed for a waveshape analyses based on the light emission distribution proposed by Segreto [47] and described in subsection 4.1.1.

4.2.4 Run 1 Analyses - Effects of the Quartz Window, Nitrogen Doping and Xenon Doping

Run 1 produced data for the scintillation of liquid argon with and without nitrogen. Three cosmic paddles were used as trigger and the data is from cosmic muons. The light was collected by two sets of X-ARAPUCA light collector. The first set of X-ARAPUCAs was covered with a quartz glass window opaque to the liquid argon scintillation wavelength ($127nm$).

The effects of the quartz glass window covering are shown in figure 4.10. The comparison is made by evaluating the frequency of the photon yield of cosmic muons events in the two X-ARAPUCA set ups (Quartz covering vs regular X-ARAPUCAs). The two X-ARAPUCAs with cover saw 5 times less light in average than the regular set up. This information will be useful after the doping with xenon, to evaluate how much light is converted from the LAr emission to the Xenon Emission ($174nm$).

Figure 4.10 is the comparison between the histogram of photons detected of the two X-ARAPUCA set ups. The histogram x-axis values are the number of photons detected, each entry is one of the cosmic muon signals. The total charge of the signal is divided by the charge of a single photon electron (SPhE) to obtain the number of photons detected. The value is also correct for the transparency of the quartz window in the relevant channels.

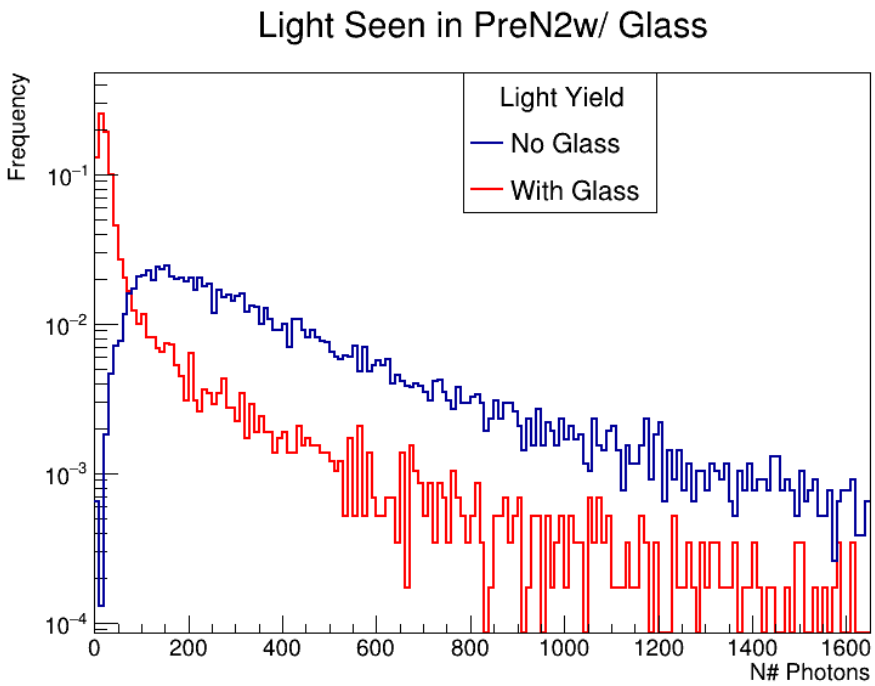

Figure 4.10: The histogram of frequency (y axis) of events with a set number of photons seen (x axis) from run 1, comparing the light seen from the X-ARAPUCAs with and without the quartz glass window (with glass vs no glass). The number of photons in the quartz covered set up is significantly shifted to the left of the graph, with the peak being very close to 0 photons. The histogram of the regular set up has the shape of whats expected from a cosmic muon spectrum.

After the contamination accident in the ProtoDUNE-SP detector, the value for the

argon slow component was measured around $700ns$, suggesting a concentration of $5.7ppm$ of nitrogen. The idea was to reproduce this contamination level in the preliminary test at building 182.

That was done by slowly injecting nitrogen into the dewar with argon, while tracking the value of the argon slow component with short data collections from cosmic muons. This tracking runs used only two cosmic paddles as trigger.

The injection of N_2 lasted almost 3h, after which the value for the slow component of the contaminated LAr was around $600ns$, indicating that more nitrogen was injected than the desired $5.7ppm$. The evolution of the slow component of LAr emissions during nitrogen injection is shown in figure 4.11.

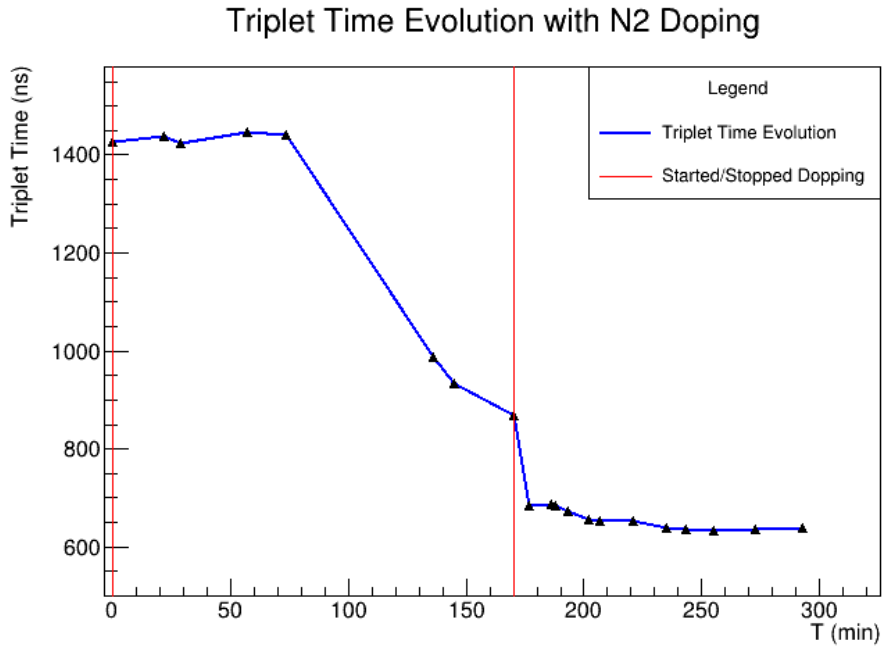

Figure 4.11: Time for the slow component of LAr scintillation during the injection of nitrogen, the vertical red lines indicate starting and ending times for the injection. After the injection was stopped, the triplet decay dropped significantly and resulted in a higher concentration of nitrogen than initially planned.

The effects of nitrogen were also present in the light yield, reducing the average number of photons seen in events by 70% in both X-ARAPUCA set ups (with and without quartz covering). As a result of the nitrogen doping, there was a significant light signal degradation in our set up, as expected.

The next step consisted in doping the contaminated LAr with xenon and evaluating how much of the light yield is recovered, and how much of the argon light ($127nm$) is converted to xenon light ($174nm$) by comparing the set ups with and without quartz cover.

The first step of xenon doping (adding $10ppm$) was also monitored with shorter runs (4.13). The doping lasted 70 minutes, and the first signals of a difference in light yield and waveshape were noticed 30 minutes after the xenon injection was finished. The effects of xenon on the waveshape will be discussed in subsection 4.2.6.

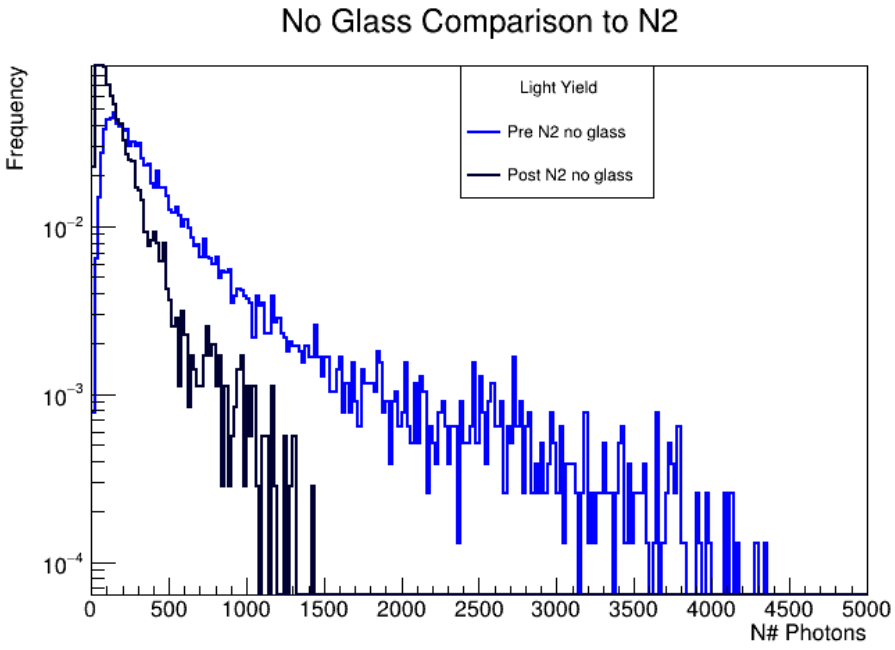

Figure 4.12: Histogram comparing the frequency of light yields in cosmic trigger events for the regular X-ARAPUCA set up (no covering) after the injection of nitrogen. The average amount of photons seen decreased after the addition of nitrogen, and the histogram in black reflects that.

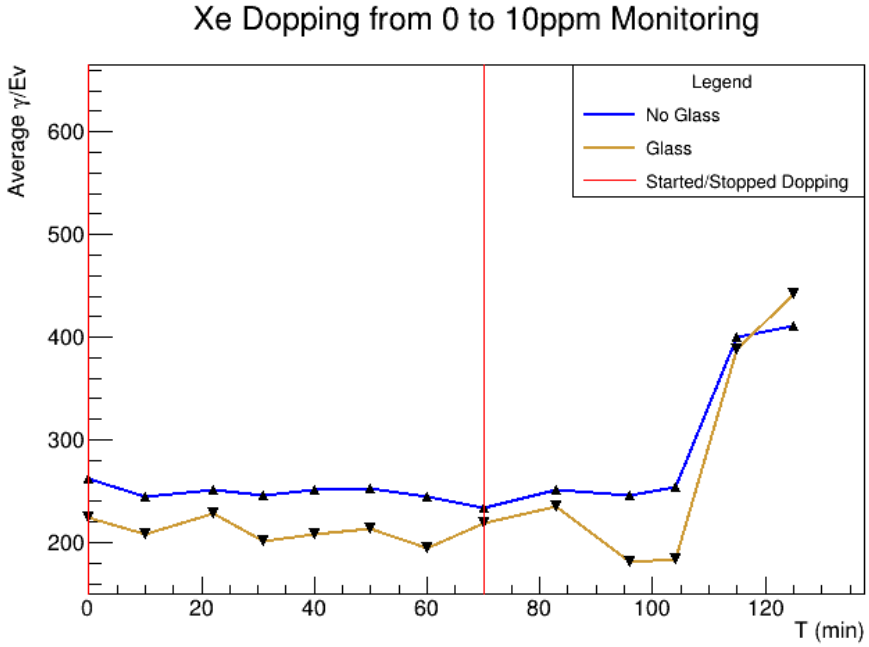

Figure 4.13: Evolution of the average light yield per event during the doping with 10ppm of xenon in Run 1. The vertical red lines indicate when the doping started and ended.

Adding $10ppm$ of xenon had a drastic effect on the relative light yield in relation to the first two tests (With pure LAr and with nitrogen contamination).

In the X-ARAPUCA set up without quartz covering, able to detect both argon and xenon light, adding xenon in the nitrogen contaminated LAr increased the average light

yield by three times. In relation to the first test of Run 1, using pure liquid argon, the relative light yield with Xenon and Nitrogen in the mix was 95% in relation to pure liquid argon, the light yield was almost fully recovered with only 10ppm of Xenon, this is better than expected and suggested that the larger scale test with xenon doping in the ProtoDUNE-SP was viable. By the time of writing of this thesis, the results from the ProtoDUNE-SP test with Xenon doping in 2020 are yet not published.

In the X-ARAPUCA set up with quartz covering, sensible mainly to xenon light, the addition of xenon increased significantly the amount of light detected by, the relative light yield in relation to the regular set up was of 90%, indicating a high conversion rates between argon (127nm) to xenon light (174nm).

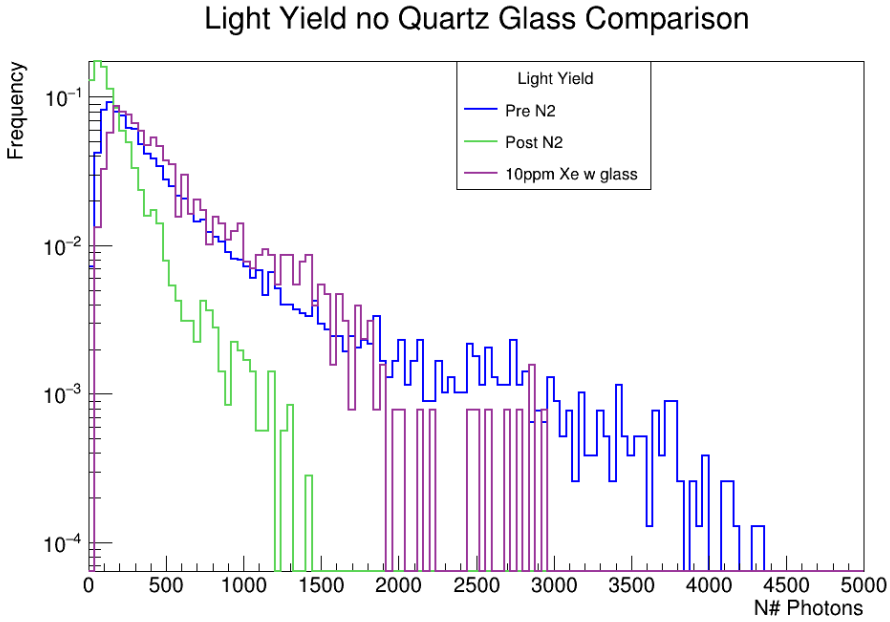

Figure 4.14: Relative light yield comparison between the tests with pure LAr (blue), with N_2 (green), and with N_2 and 10ppm of Xenon doping (purple). Adding Xenon increased the relative light yield to amounts similar to the pure argon data collection.

The tests with 20ppm and 30ppm of Xenon doping showed a small reduction in the average photon yield, this might be due to thermal stresses and damage to the WLS coating of the X-ARAPUCA, some damage to the coating was noticed after they were disassembled from the experiment.

The tests with pure LAr in Run 2 also had lower relative light yields than Run 1 tests with pure LAr, indicating that the damage in the WLS coating affected the light yield.

4.2.5 Run 2 - Effects Xenon doping on pure LAr

Run 2 inverted the doping order, starting with doping pure LAr with 10ppm of xenon. Preliminary tests showed a reduction of light yield with pure LAr with respect to Run 1, probably due to the damage in the WLS coating.

A first pure LAr test was done to establish the baseline for light yield. Adding 10ppm of Xenon to pure LAr resulted in a increase of relative light yield of 34% in relation to pure

LAr. This is increase in light yield is consistent with previous observations [47], and is one of the unexplained aspects of Xenon doped LAr scintillation. A possible explanation is that the Xenon competes with self quenching of LAr (equations 2.7-2.8), causing the emission of light that would otherwise be quenched. The tests with higher concentrations of xenon (20 and 30ppm) don't show any further increase in the light yield (figure 4.15).

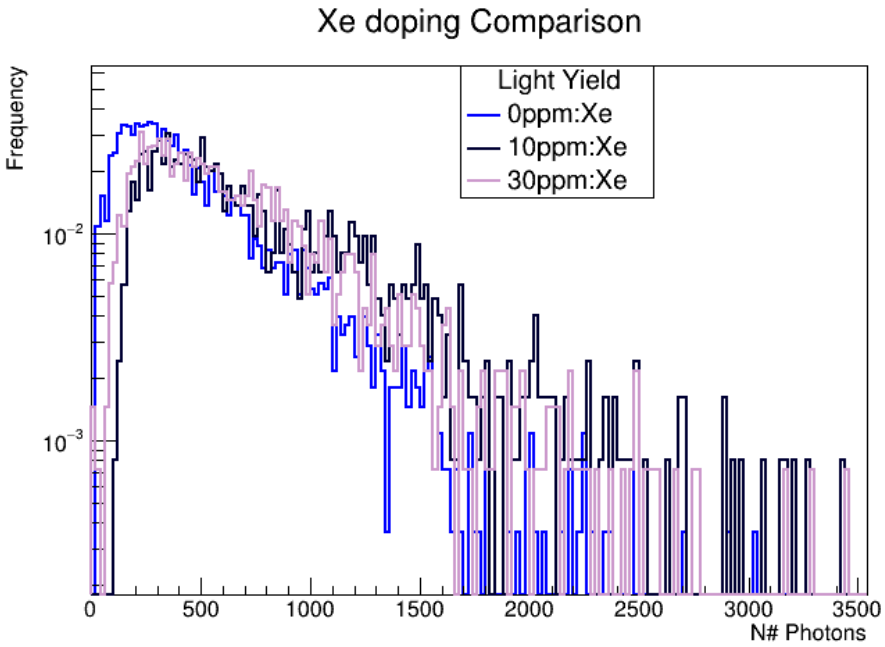

Figure 4.15: Light yield comparison between pure LAr, and xenon doped LAr at 10 and 30ppm. The relative light yield increase with the addition of xenon is of 34% for both concentrations.

It's also possible to evaluate the conversion from argon scintillation light (127nm) to xenon light (174nm) by comparing the relative light yield between the quartz covered X-ARAPUCA set up with the regular set up. In the pure LAr test, the X-ARAPUCAs with quartz covering detected only 17% of the light compared to the regular set up. After adding 10ppm of xenon the average light yield ratio was of 91%, with 20ppm of xenon the ratio was 94%, and with 30ppm the ratio was of 98%, this indicates almost full conversion between argon and xenon light even at relatively low amounts of xenon (figure 4.16).

In the last test nitrogen was added to the mixture of xenon and LAr, and this resulted in a decrease of the average light yield in accordance to the analysis of Run 1.

4.2.6 Waveshape Analysis of Xenon Doped LAr

The light emission waveshape was also evaluated from doped LAr in a similar way to section 3.3. The goal was the fit the parameters of equations 4.19-4.22 to the waveshape seen by the X-ARAPUCAs in the experiment.

The process is the same of the section 3.3, first the waveshape of the electronic response of the X-ARAPUCA is evaluated using the calibration data. Waveshapes with the expected charge for a single photon are selected and used to create the average sin-

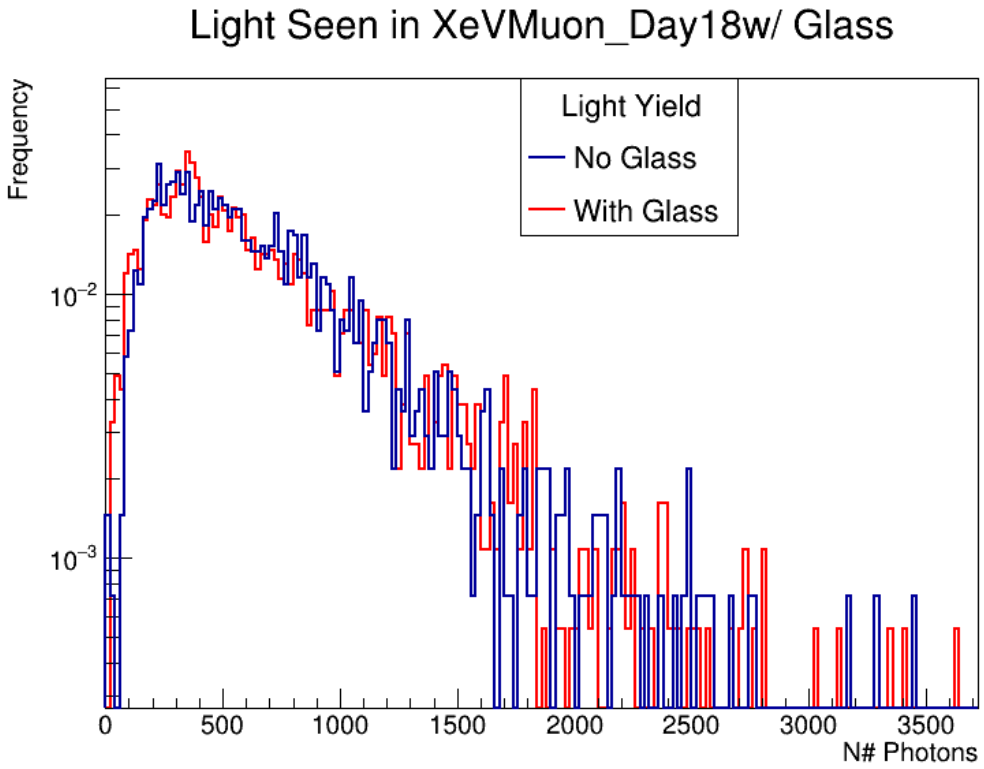

Figure 4.16: Histogram comparison between the two set ups with 30ppm of Xenon, the amount of light detected is effectively the same, and the argon light filtering quartz window has no significant effect.

gle photon waveshape, that represents the electronic response of the X-ARAPUCA light collector (figure 4.17).

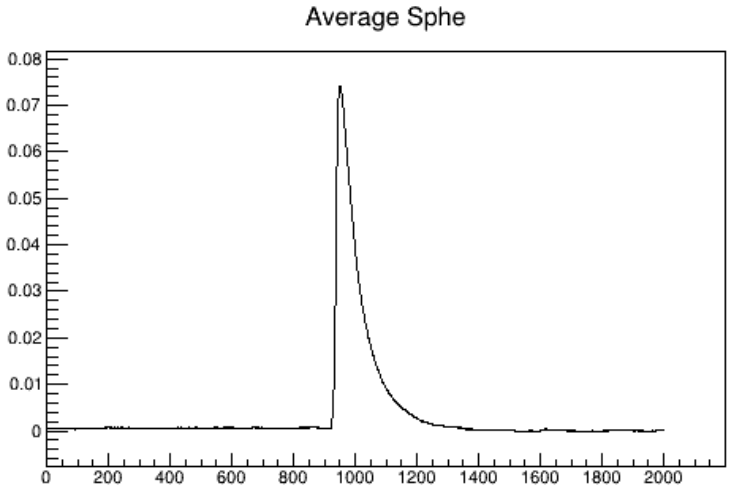

Figure 4.17: Average Single Photon Electron waveshape

The light signal model for xenon doped LAr is:

$$l(t-t_0|\tau_s,\alpha_s,\tau_3,\alpha_3,\tau_d,k^+) = l_s(t-t_0) + l_3(t-t_0) + l_{Xe}(t-t_0). \tag{4.24}$$

With each term according to equations 4.19-4.22. To write a computational model of the detected signal, another exponential term is added to account for the effects of the delayed light due to the PTP wavelength shifter. This model of the light sources is convoluted with the SPhE waveshape to include the electronic response of the SiPM in the X-ARAPUCA in the model:

$$\begin{aligned} S(t|\theta_i) = l(t|\theta_i) \circledast R[t] \approx \sum_{t_i} l(t - t_i) R[t_i] \\ \theta_i = \{t_0, \tau_s, \alpha_s, \tau_{ptp}, \alpha_{ptp}, \tau_3, \alpha_3, \tau_d, q\}, \end{aligned} \tag{4.25}$$

this model was fitted with average waveshapes from both runs. The average waveshape of the experiment is obtained in a similar fashion to subsection 3.3.2, in which the same three criteria are used to select for waveshapes: the signal can't be saturated, the waveshape has a single clear peak, the peak position is close to the expected position. An average waveshape is constructed from the selected waveshapes.

The fit is based on minimizing the χ^2 difference between the computational model in equation 4.25 and the average waveshape, an additional scale parameter is added to ease the fit, specially for the relative scintillation constants:

$$\begin{aligned} \chi^2(\theta_i) = \sum_{t_i} \left(\frac{(S_{cale} \cdot S(t_i|\theta_i) - D[t_i])^2}{D[t_i]} \right) \\ \theta_i = \{t_0, \tau_s, \alpha_s, \tau_{ptp}, \alpha_{ptp}, \tau_3, \alpha_3, \tau_d, k^+, S_{cale}\}. \end{aligned} \tag{4.26}$$

The results for the parameters are similar in both runs, an example of a fit is shown in figure 4.19. It should be noted that in the runs with nitrogen contamination the value of the fast light emission (τ_s) is not reliable due to the effects of nitrogen [46], the values of the PTP related parameters are also effective and don't represent physical processes [66].

One of the main parameters of interest is the relative abundance of singlet and triplet light, for muons the triplet amount should be about 77% , which is consistent with the values obtained by the fit, indicating that the fit parameters are representative of the waveshape of the muon signal.

The k^+ and τ_d values are also important, they have not been determined for muon particles before, and with $\tau_d = 1/[Xe]k_{Xe}$ it's expected that the value of the parameter for 10ppm of xenon should be two times the value for 20ppm, and three times for 30ppm of xenon ($\tau_d([Xe] = 10ppm) = 2 \cdot \tau_d(20ppm) = 3 \cdot \tau_d(30ppm)$). Since the values of xenon concentrations are known, it's also possible to determine the value of k_{Xe}, the interaction rate between argon and xenon dimers.

Comparing the results from run 1 (table 4.1) and run 2 (table 4.2) the values for k_{Xe} are similar, the characteristic time due to xenon concentration τ_d do scale as expected. It's also notable that the values for the triplet time are higher without the presence of Xenon.

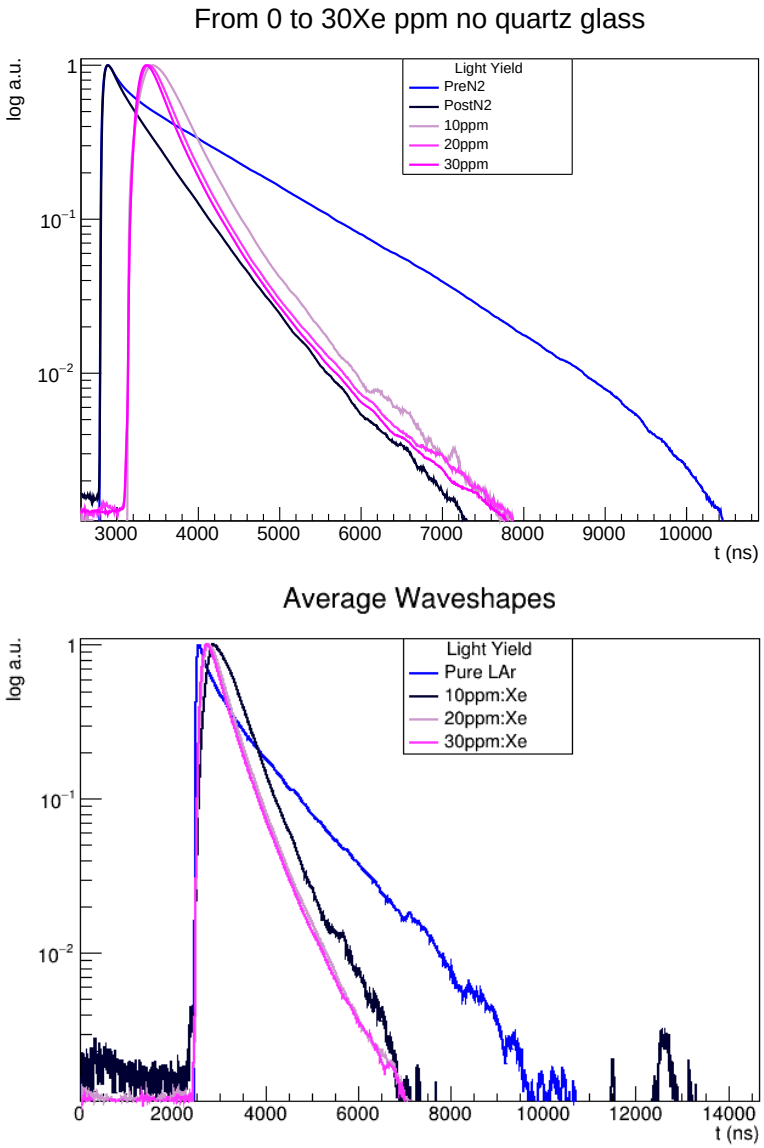

Figure 4.18: Top: Average waveshapes for run 1. Bottom: Average waveshapes for run 2.

Xenon Concentration ($\pm 1ppm$)	$10ppm + N_2$	$20ppm + N_2$	$30ppm + N_2$
$\alpha_s(\pm 5\%)$	22%	31%	20%
$\tau_3(\pm 50\ ns)$	952	1004	910
$\alpha_3(\pm 5\%)$	73%	73%	73%
$\tau_d(\pm 5ns)$	150	75	50
$k^+(\pm 0.005\ ns^{-1})$	0.036	0.059	0.15
$k_{Xe}(\pm 0.0002ns^{-1})$	0.00066	0.00064	0.00065

Table 4.1: Fit results from run 1, all runs contain nitrogen doping as well as xenon doping

4.2.7 Final Discussion

The analyses of both Run 1, Run 2 and the waveshape of xenon doped LAr indicates that even small relatively small amounts of xenon are enough to significantly affect the waveshape, light yield and light emission wavelength in comparison to pure LAr signals.

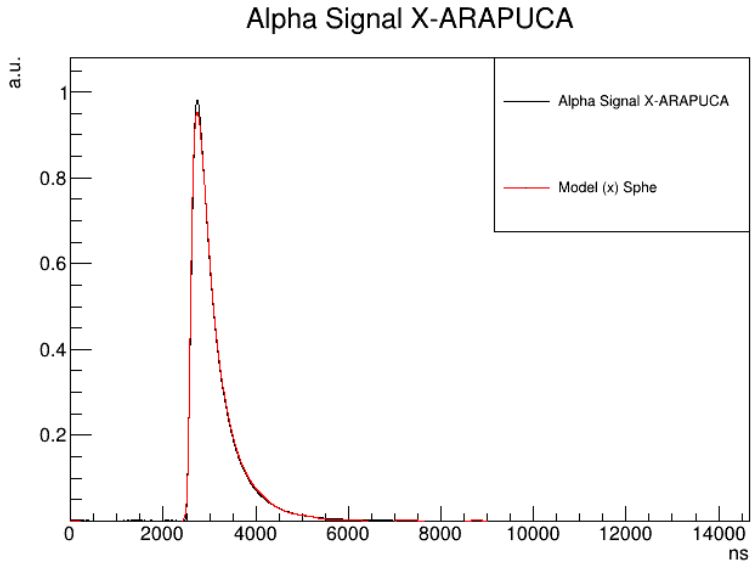

Figure 4.19: Fit example from Run 2 with 30ppm Xenon Dopping and no nitrogen.

Xenon Concentration ($\pm 1ppm$)	$10ppm$	$20ppm$	$30ppm$
$\alpha_s(\pm 5\%)$	24%	22%	22%
$\tau_3(\pm 50\ ns)$	1380	1190	1320
$\alpha_3(\pm 5\%)$	78%	78%	78%
$\tau_d(\pm 5ns)$	158	81	68
$k^+(\pm 0.005\ ns^{-1})$	0.019	0.013	0.56
$k_{Xe}(\pm 0.0002ns^{-1})$	0.00063	0.00061	0.00049

Table 4.2: Fit results from run 2, all runs contain only xenon doping.

With run 1 it's possible to conclude that the tested concentrations of xenon ($10 - 30ppm$) is enough to recover a significant portion of the light signal lost to nitrogen contamination, this conclusion was essential in motivating the larger test with Xenon doping at the ProtoDUNE.

Run 2 indicates an actual increase in light yield from doping pure LAr with xenon. An increase of 34% as observed can't be explained by an increase in wavelength shift conversion efficiency due to xenon light having a higher wavelength, this increase must be related to the physics of xenon doped LAr [47].

The waveshape analyses determined for the first time the interaction rate in the energy transfer process of argon to xenon in the model described in subsection 4.1, as well as the parameter associated with regular argon quenching (k^+).

Chapter 5

Conclusion

The experiments with the X-ARAPUCA photon collector at Lab Leptons (subsection 3.1) allowed for the determination of the X-ARAPUCA photon detection efficiency with the value of $3 \pm 0.6\%$, above the minimum required for the DUNE experiment scientific goals (1%), further establishing the X-ARAPUCA as the best photon collector for the DUNE photon detection system, given size constraints and efficiency required. This result was obtained by the analysis of the light emitted by argon scintillation due to alpha particles from a source with known spectrum, allowing for the development of simulation of the experimental set up and an estimation of the number of photons crossing the X-ARAPUCA window. The simulated photon count could than be compared to the experimental photon count, taking into account the radiation background noise and electronic noises from the light detection by the SiPMs, after these additional effects are taken into account, the last difference between the simulated photon count and the experimental one is a scale factor that is the X-ARAPUCA photon collector efficiency - as detailed in section 3.2.

The data collected with this experiment, produced by pure liquid argon scintillation due to alpha particles, also allowed for a second result: the evaluation of liquid argon scintillation model proposed by Segreto in 2020 [47]. This model proposes mechanisms for the self-quenching in liquid argon. Quenching is the process through which excited argon dimers (Ar_2^*) lose energy without emitting light. The mechanisms behind the quenching model are not fully clarified, with the model under study proposing two collision based de-excitation processes.

With the LAr scintillation model it's possible to construct a light emission model to determine the parameters associated with the proposed quenching mechanism. These parameters weren't determined for alpha particle scintillation before this work. The two parameters in question are the de-excitation rate due to the collision with ionized argon dimmers k^+ and due to the collision with excited argon dimers q. The best fit result for these parameters are $k^+ = 2.9 \pm 0.5 \times 10^{-4} ns^{-1}$ and $q = 4.0 \pm 0.5 \times 10^{-4} ns^{-1}$. To obtain these values a full observed signal model was developed, taking into account all the effects that shape the observed signal, including light sources (Argon Scintillation and Wavelength Shifters) plus the electronic effects of light detection with the SiPM. The full signal model was than fitted with an average liquid argon waveshape using χ^2 minimization, detailed in 3.3

The second part of this work is related to an experimental test using Xenon doped Liquid Argon done at building 182 at CERN. This experiment had the goal of determining if a larger scale test at the ProtoDUNE experiment was viable, this was because the ProtoDUNE had an accident in July 2019 in which atmospheric air mixed with argon, resulting in a significant contamination by Nitrogen in the Argon and a degradation of the light signal. Doping Nitrogen contaminated LAr with Xenon could be a way to recover the damage to the light signal, but the necessary amount of xenon was not known at the time. The tests at building 182 were preliminary tests in order to evaluate how much Xenon would be necessary to recover the light signal at protoDUNE.

Run 1 Xenon Doping Test at Building 182 produced data from cosmic muon scintillation in five different scenarios: pure LAr, nitrogen contaminated LAr (similar levels to protoDUNE), and three data collections with 10, 20 and 30ppm of Xenon in the nitrogen contaminated LAr. Using the data from the five different data collections it was possible to establish the amount of light seen with pure LAr as a baseline, the amount of signal degradation after the contamination with Nitrogen and the amount recovered due to the three different Xenon doping steps. The addition of nitrogen reduced the relative light yield by 70% in relation to pure LAr, and adding only 10ppm of Xenon recovered 95% of the relative light yield in relation to pure LAr - almost total recover with only 10pmm of Xenon, establishing that a larger test at ProtoDUNE was viable. Adding more Xenon had no significant effects on the light yield. At the time of this writing, the results of the Xenon doping Tests at ProtoDUNE have not yet been published.

The light collector used in the experiments at Building 182 were four X-ARAPUCA photon collector, two regular ones, and two covered with quartz windows opaque to argon scintillation (127nm) and transparent to xenon scintillation (174nm). Comparing the amount of light detected by each set up, it was possible to estimate the conversion from argon to xenon light ($127 \rightarrow 174nm$). In Run 1 the difference of the light yield with and without quartz covering was of only 10%, indicating a high conversion rate.

Run 2 at Building 182 collected data from Xenon Doped LAr without any contamination from nitrogen, allowing to further study the light conversion and relative light yield due to Xenon doping. Adding 10ppm of xenon to pure LAr increased the relative light yield by 34% in relation to pure LAr, this result adds to the evidence that xenon might be able to increase the total light yield when diluted in LAr [47]. The difference of light yield between the two X-ARAPUCA set ups was of 9% for 10ppm of Xenon and only 2% for 30ppm, suggesting almost total light conversion with 30ppm of xenon in LAr.

A light emission model for Xenon doped LAr was also proposed by Segreto [47] in the same paper, a full signal model taking into account the light emission and electronic response was developed for this experiment, allowing to determine the energy transfer rate from Argon to Xenon in the studied model $k_{Xe} = 6 \pm 2 \times 10^{-4} ns^{-1}$. The study of Xenon doped LAr at Building 182 is further detailed in Chapter 4.

The results from the experiments at Building 182 established the viability of the Xenon doping test at protoDUNE, indicating the viability of Xenon doping as a mean to recover light signals due to accidental Nitrogen contamination, as well as furthering the body of evidence that there is useful properties in Xenon doped LAr that might be useful to particle physics experiments such as DUNE.

Bibliography

[1] I. V. Anicin, "The Neutrino - Its Past, Present and Future," pp. 1–60, 2005.

[2] F. Reines, C. L. Cowan, F. B. Harrison, A. D. McGuire, and H. W. Kruse, "Detection of the free antineutrino," *Physical Review*, vol. 117, no. 1, pp. 159–173, 1960.

[3] R. Davis, "A review of the homestake solar neutrino experiment," *Progress in Particle and Nuclear Physics*, vol. 32, pp. 13–32, jan 1994.

[4] R. Davis, D. S. Harmer, and K. C. Hoffman, "Search for neutrinos from the sun," *Phys. Rev. Lett.*, vol. 20, pp. 1205–1209, May 1968.

[5] K. S. Hirata, K. Inoue, T. Ishida, T. Kajita, K. Kihara, M. Nakahata, K. Nakamura, S. Ohara, N. Sato, Y. Suzuki, Y. Totsuka, Y. Yaginuma, M. Mori, Y. Oyama, A. Suzuki, K. Takahashi, M. Yamada, M. Koshiba, K. Nishijima, T. Suda, T. Tajima, K. Miyano, H. Miyata, H. Takei, Y. Fukuda, E. Kodera, Y. Nagashima, M. Takita, K. Kaneyuki, T. Tanimori, E. W. Beier, L. R. Feldscher, E. D. Frank, W. Frati, S. B. Kim, A. K. Mann, F. M. Newcomer, R. Van Berg, and W. Zhang, "Real-time, directional measurement of B 8 solar neutrinos in the Kamiokande II detector," *Physical Review D*, vol. 44, pp. 2241–2260, oct 1991.

[6] A. I. Abazov, O. L. Anosov, E. L. Faizov, V. N. Gavrin, A. V. Kalikhov, T. V. Knodel, I. I. Knyshenko, V. N. Kornoukhov, S. A. Mezentseva, I. N. Mirmov, A. V. Ostrinsky, A. M. Pshukov, N. E. Revzin, A. A. Shikhin, P. V. Timofeyev, E. P. Veretenkin, V. M. Vermul, G. T. Zatsepin, T. J. Bowles, B. T. Cleveland, S. R. Elliott, H. A. O'Brien, D. L. Wark, J. F. Wilkerson, R. Davis, K. Lande, M. L. Cherry, and R. T. Kouzes, "Search for neutrinos from the Sun using the reaction Ga71(ν_e, e)71Ge," $Physical Review Letters, vol.$ 67, $pp.$ 3332 − −3335, dec1991.

[7] P. Anselmann, R. Fockenbrock, W. Hampel, G. Heusser, J. Kiko, T. Kirsten, M. Laubenstein, E. Pernicka, S. Pezzoni, U. Rönn, M. Sann, F. Spielker, R. Wink, M. Wójcik, R. v. Ammon, K. H. Ebert, T. Fritsch, D. Heidt, E. Henrich, C. Schlosser, L. Stieglitz, F. Weirich, M. Balata, H. Lalla, E. Bellotti, C. Cattadori, O. Cremonesi, N. Ferrari, E. Fiorini, L. Zanotti, M. Altmann, F. v. Feilitzsch, R. Mößbauer, U. Schanda, G. Berthomieu, E. Schatzman, I. Carmi, I. Dostrovsky, C. Bacci, P. Belli, R. Bernabei, S. D'Angelo, L. Paoluzi, A. Bevilacqua, S. Charbit, M. Cribier, G. Dupont, L. Gosset, J. Rich, M. Spiro, T. Stolarczyk, C. Tao, D. Vignaud,

J. Boger, R. L. Hahn, F. X. Hartmann, J. K. Rowley, R. W. Stoenner, and J. Weneser, "First results from the 51Cr neutrino source experiment with the GALLEX detector," *Physics Letters B*, vol. 342, pp. 440–450, jan 1995.

[8] A. Dar, "Solar Neutrinos and The Standard Solar Model," jul 1997.

[9] S. Turck-Chièze, "The Standard Solar Model and beyond," *Journal of Physics: Conference Series*, vol. 665, no. 1, 2016.

[10] B. PONTECORVO, "Neutrino Experiments and the Question of Leptonic-Charge Conservation," *Old and New Problems in Elementary Particles*, vol. 26, no. 5, pp. 251–261, 1968.

[11] B. Aharmim, Q. R. Ahmad, S. N. Ahmed, R. C. Allen, T. C. Andersen, J. D. Anglin, G. Bühler, J. C. Barton, E. W. Beier, M. Bercovitch, M. Bergevin, J. Bigu, S. D. Biller, R. A. Black, I. Blevis, R. J. Boardman, J. Boger, E. Bonvin, M. G. Boulay, M. G. Bowler, T. J. Bowles, S. J. Brice, M. C. Browne, T. V. Bullard, T. H. Burritt, J. Cameron, Y. D. Chan, H. H. Chen, M. Chen, X. Chen, B. T. Cleveland, J. H. M. Cowan, D. F. Cowen, G. A. Cox, C. A. Currat, X. Dai, F. Dalnoki-Veress, W. F. Davidson, H. Deng, M. DiMarco, P. J. Doe, G. Doucas, M. R. Dragowsky, C. A. Duba, F. A. Duncan, M. Dunford, J. A. Dunmore, E. D. Earle, S. R. Elliott, H. C. Evans, G. T. Ewan, J. Farine, H. Fergani, A. P. Ferraris, F. Fleurot, R. J. Ford, J. A. Formaggio, M. M. Fowler, K. Frame, E. D. Frank, W. Frati, N. Gagnon, J. V. Germani, S. Gil, A. Goldschmidt, J. T. M. Goon, K. Graham, D. R. Grant, E. Guillian, R. L. Hahn, A. L. Hallin, E. D. Hallman, A. S. Hamer, A. A. Hamian, W. B. Handler, R. U. Haq, C. K. Hargrove, P. J. Harvey, R. Hazama, K. M. Heeger, W. J. Heintzelman, J. Heise, R. L. Helmer, R. Henning, J. D. Hepburn, H. Heron, J. Hewett, A. Hime, C. Howard, M. A. Howe, M. Huang, J. G. Hykaway, M. C. P. Isaac, P. Jagam, B. Jamieson, N. A. Jelley, C. Jillings, G. Jonkmans, K. Kazkaz, P. T. Keener, K. Kirch, J. R. Klein, A. B. Knox, R. J. Komar, L. L. Kormos, M. Kos, R. Kouzes, A. Krüger, C. Kraus, C. B. Krauss, T. Kutter, C. C. M. Kyba, H. Labranche, R. Lange, J. Law, I. T. Lawson, M. Lay, H. W. Lee, K. T. Lesko, J. R. Leslie, I. Levine, J. C. Loach, W. Locke, S. Luoma, J. Lyon, R. MacLellan, S. Majerus, H. B. Mak, J. Maneira, A. D. Marino, R. Martin, N. McCauley, A. B. McDonald, D. S. McDonald, K. McFarlane, S. McGee, G. McGregor, R. M. Drees, H. Mes, C. Mifflin, K. K. S. Miknaitis, M. L. Miller, G. Milton, B. A. Moffat, B. Monreal, M. Moorhead, B. Morrissette, C. W. Nally, M. S. Neubauer, F. M. Newcomer, H. S. Ng, B. G. Nickel, A. J. Noble, E. B. Norman, V. M. Novikov, N. S. Oblath, C. E. Okada, H. M. O'Keeffe, R. W. Ollerhead, M. Omori, J. L. Orrell, S. M. Oser, R. Ott, S. J. M. Peeters, A. W. P. Poon, G. Prior, S. D. Reitzner, K. Rielage, A. Roberge, B. C. Robertson, R. G. H. Robertson, S. S. E. Rosendahl, J. K. Rowley, V. L. Rusu, E. Saettler, A. Schülke, M. H. Schwendener, J. A. Secrest, H. Seifert, M. Shatkay, J. J. Simpson, C. J. Sims, D. Sinclair, P. Skensved, A. R. Smith, M. W. E. Smith, N. Starinsky, T. D. Steiger, R. G. Stokstad, L. C. Stonehill, R. S. Storey, B. Sur, R. Tafirout, N. Tagg, Y. Takeuchi, N. W. Tanner, R. K. Taplin, M. Thorman, P. M. Thornewell, N. Tolich, P. T. Trent, Y. I. Tserkovnyak, T. Tsui, C. D. Tunnell, R. V.

Berg, R. G. V. de Water, C. J. Virtue, T. J. Walker, B. L. Wall, C. E. Waltham, H. W. C. Tseung, J.-X. Wang, D. L. Wark, J. Wendland, N. West, J. B. Wilhelmy, J. F. Wilkerson, J. R. Wilson, P. Wittich, J. M. Wouters, A. Wright, M. Yeh, and K. Zuber, "Determination of the ν e and total B 8 solar neutrino fluxes using the Sudbury Neutrino Observatory Phase I data set," *Physical Review C*, vol. 75, p. 045502, apr 2007.

[12] Y. Fukuda, T. Hayakawa, E. Ichihara, K. Inoue, K. Ishihara, H. Ishino, Y. Itow, T. Kajita, J. Kameda, S. Kasuga, K. Kobayashi, Y. Kobayashi, Y. Koshio, M. Miura, M. Nakahata, S. Nakayama, A. Okada, K. Okumura, N. Sakurai, M. Shiozawa, Y. Suzuki, Y. Takeuchi, Y. Totsuka, S. Yamada, M. Earl, A. Habig, E. Kearns, M. D. Messier, K. Scholberg, J. L. Stone, L. R. Sulak, C. W. Walter, M. Goldhaber, T. Barszczxak, D. Casper, W. Gajewski, P. G. Halverson, J. Hsu, W. R. Kropp, L. R. Price, F. Reines, M. Smy, H. W. Sobel, M. R. Vagins, K. S. Ganezer, W. E. Keig, R. W. Ellsworth, S. Tasaka, J. W. Flanagan, A. Kibayashi, J. G. Learned, S. Matsuno, V. J. Stenger, D. Takemori, T. Ishii, J. Kanzaki, T. Kobayashi, S. Mine, K. Nakamura, K. Nishikawa, Y. Oyama, A. Sakai, M. Sakuda, O. Sasaki, S. Echigo, M. Kohama, A. T. Suzuki, T. J. Haines, E. Blaufuss, B. K. Kim, R. Sanford, R. Svoboda, M. L. Chen, Z. Conner, J. A. Goodman, G. W. Sullivan, J. Hill, C. K. Jung, K. Martens, C. Mauger, C. McGrew, E. Sharkey, B. Viren, C. Yanagisawa, W. Doki, K. Miyano, H. Okazawa, C. Saji, M. Takahata, Y. Nagashima, M. Takita, T. Yamaguchi, M. Yoshida, S. B. Kim, M. Etoh, K. Fujita, A. Hasegawa, T. Hasegawa, S. Hatakeyama, T. Iwamoto, M. Koga, T. Maruyama, H. Ogawa, J. Shirai, A. Suzuki, F. Tsushima, M. Koshiba, M. Nemoto, K. Nishijima, T. Futagami, Y. Hayato, Y. Kanaya, K. Kaneyuki, Y. Watanabe, D. Kielczewska, R. A. Doyle, J. S. George, A. L. Stachyra, L. L. Wai, R. J. Wilkes, and K. K. Young, "Evidence for Oscillation of Atmospheric Neutrinos," *Physical Review Letters*, vol. 81, pp. 1562–1567, aug 1998.

[13] P. A. Zyla, R. M. Barnett, J. Beringer, O. Dahl, D. A. Dwyer, D. E. Groom, C. J. Lin, K. S. Lugovsky, E. Pianori, D. J. Robinson, C. G. Wohl, W. M. Yao, K. Agashe, G. Aielli, B. C. Allanach, C. Amsler, M. Antonelli, E. C. Aschenauer, D. M. Asner, H. Baer, S. Banerjee, L. Baudis, C. W. Bauer, J. J. Beatty, V. I. Belousov, S. Bethke, A. Bettini, O. Biebel, K. M. Black, E. Blucher, O. Buchmuller, V. Burkert, M. A. Bychkov, R. N. Cahn, M. Carena, A. Ceccucci, A. Cerri, D. Chakraborty, R. Sekhar Chivukula, G. Cowan, G. D'Ambrosio, T. Damour, D. de Florian, A. de Gouvêa, T. DeGrand, P. de Jong, G. Dissertori, B. A. Dobrescu, M. D'Onofrio, M. Doser, M. Drees, H. K. Dreiner, P. Eerola, U. Egede, S. Eidelman, J. Ellis, J. Erler, V. V. Ezhela, W. Fetscher, B. D. Fields, B. Foster, A. Freitas, H. Gallagher, L. Garren, H. J. Gerber, G. Gerbier, T. Gershon, Y. Gershtein, T. Gherghetta, A. A. Godizov, M. C. Gonzalez-Garcia, M. Goodman, C. Grab, A. V. Gritsan, C. Grojean, M. Grünewald, A. Gurtu, T. Gutsche, H. E. Haber, C. Hanhart, S. Hashimoto, Y. Hayato, A. Hebecker, S. Heinemeyer, B. Heltsley, J. J. Hernández-Rey, K. Hikasa, J. Hisano, A. Höcker, J. Holder, A. Holtkamp, J. Huston, T. Hyodo, K. F. Johnson, M. Kado, M. Karliner, U. F. Katz, M. Kenzie, V. A. Khoze, S. R. Klein, E. Klempt, R. V. Kowalewski, F. Krauss, M. Kreps, B. Krusche, Y. Kwon, O. Lahav, J. Laiho,

L. P. Lellouch, J. Lesgourgues, A. R. Liddle, Z. Ligeti, C. Lippmann, T. M. Liss, L. Littenberg, C. Lourenço, S. B. Lugovsky, A. Lusiani, Y. Makida, F. Maltoni, T. Mannel, A. V. Manohar, W. J. Marciano, A. Masoni, J. Matthews, U. G. Meißner, M. Mikhasenko, D. J. Miller, D. Milstead, R. E. Mitchell, K. Mönig, P. Molaro, F. Moortgat, M. Moskovic, K. Nakamura, M. Narain, P. Nason, S. Navas, M. Neubert, P. Nevski, Y. Nir, K. A. Olive, C. Patrignani, J. A. Peacock, S. T. Petcov, V. A. Petrov, A. Pich, A. Piepke, A. Pomarol, S. Profumo, A. Quadt, K. Rabbertz, J. Rademacker, G. Raffelt, H. Ramani, M. Ramsey-Musolf, B. N. Ratcliff, P. Richardson, A. Ringwald, S. Roesler, S. Rolli, A. Romaniouk, L. J. Rosenberg, J. L. Rosner, G. Rybka, M. Ryskin, R. A. Ryutin, Y. Sakai, G. P. Salam, S. Sarkar, F. Sauli, O. Schneider, K. Scholberg, A. J. Schwartz, J. Schwiening, D. Scott, V. Sharma, S. R. Sharpe, T. Shutt, M. Silari, T. Sjöstrand, P. Skands, T. Skwarnicki, G. F. Smoot, A. Soffer, M. S. Sozzi, S. Spanier, C. Spiering, A. Stahl, S. L. Stone, Y. Sumino, T. Sumiyoshi, M. J. Syphers, F. Takahashi, M. Tanabashi, J. Tanaka, M. Taševský, K. Terashi, J. Terning, U. Thoma, R. S. Thorne, L. Tiator, M. Titov, N. P. Tkachenko, D. R. Tovey, K. Trabelsi, P. Urquijo, G. Valencia, R. van de Water, N. Varelas, G. Venanzoni, L. Verde, M. G. Vincter, P. Vogel, W. Vogelsang, A. Vogt, V. Vorobyev, S. P. Wakely, W. Walkowiak, C. W. Walter, D. Wands, M. O. Wascko, D. H. Weinberg, E. J. Weinberg, M. White, L. R. Wiencke, S. Willocq, C. L. Woody, R. L. Workman, M. Yokoyama, R. Yoshida, G. Zanderighi, G. P. Zeller, O. V. Zenin, R. Y. Zhu, S. L. Zhu, F. Zimmermann, J. Anderson, T. Basaglia, V. S. Lugovsky, P. Schaffner, and W. Zheng, "Review of particle physics," *Progress of Theoretical and Experimental Physics*, vol. 2020, no. 8, pp. 1–2093, 2020.

[14] M. Thomson, *Modern Particle Physics*. No. 3, 2014.

[15] S. M. Bilenky and B. Pontecorvo, "Lepton mixing and neutrino oscillations," *Physics Reports*, vol. 41, pp. 225–261, may 1978.

[16] M. e. a. Aker, "An improved upper limit on the neutrino mass from a direct kinematic method by KATRIN," sep 2019.

[17] D. Collaboration, "The DUNE Far Detector Interim Design Report Volume 1: Physics, Technology and Strategies," 2018.

[18] H. Nunokawa, S. Parke, and J. W. Valle, "CP violation and neutrino oscillations," *Progress in Particle and Nuclear Physics*, vol. 60, pp. 338–402, apr 2008.

[19] A. D. Sakharov, "Violation of CP in variance, C asymmetry, and baryon asymmetry of the universe," *Soviet Physics Uspekhi*, vol. 34, pp. 392–393, may 1991.

[20] M. Miura, "Search for Nucleon Decay in Super-Kamiokande," *Nuclear and Particle Physics Proceedings*, vol. 273-275, pp. 516–521, 2016.

[21] DUNE Collaboration, "The DUNE Far Detector Interim Design Report, Volume 2: Single-Phase Module," vol. 2, 2018.

[22] DUNE Collaboration, "Deep Underground Neutrino Experiment (DUNE), Far Detector Technical Design Report, Volume IV: Far Detector Single-phase Technology," vol. IV, no. January, 2020.

[23] DUNE Collaboration, "The DUNE Far Detector Interim Design Report, Volume 3: Dual-Phase Module," vol. 3, 2018.

[24] DUNE Collaboration, "Deep Underground Neutrino Experiment (DUNE) Near Detector Conceptual Design Report," mar 2021.

[25] C. Rubbia, "The Liquid-Argon Time Projection Chamber: A New Concept for Neutrino Detectors," tech. rep., 1977.

[26] S. Kubota, M. Hishida, M. Suzuki, and J. zhi Ruan, "Liquid and solid argon, krypton and xenon scintillators," *Nuclear Instruments and Methods*, vol. 196, pp. 101–105, may 1982.

[27] T. Ferbel and T. Doke, "Fundamental Properties of Liquid Argon, Krypton and Xenon As Radiation Detector Media," *Experimental Techniques in High-Energy Nuclear and Particle Physics*, vol. 12, pp. 537–577, 1991.

[28] S. Amerio, S. Amoruso, M. Antonello, P. Aprili, M. Armenante, F. Arneodo, A. Badertscher, B. Baiboussinov, M. Baldo Ceolin, G. Battistoni, B. Bekman, P. Benetti, E. Bernardini, M. Bischofberger, A. Borio di Tigliole, R. Brunetti, R. Bruzzese, A. Bueno, E. Calligarich, M. Campanelli, F. Carbonara, C. Carpanese, D. Cavalli, F. Cavanna, P. Cennini, S. Centro, A. Cesana, C. Chen, D. Chen, D. B. Chen, Y. Chen, R. Cid, D. B. Cline, K. Cieślik, A. G. Cocco, D. Corti, Z. Dai, C. de Vecchi, A. Dabrowska, A. di Cicco, R. Dolfini, A. Ereditato, M. Felcini, A. Ferella, A. Ferrari, F. Ferri, G. Fiorillo, S. Galli, D. Garcia Gamez, Y. Ge, D. Gibin, A. Gigli Berzolari, I. Gil-Botella, K. Graczyk, L. Grandi, A. Guglielmi, K. He, J. Holeczek, X. Huang, C. Juszczak, D. Kielczewska, J. Kisiel, T. Kozlowski, H. Kuna-Ciskal, M. Laffranchi, J. Lagoda, Z. Li, B. Lisowski, F. Lu, J. Ma, G. Mangano, G. Mannocchi, M. Markiewicz, A. Martinez de la Ossa, C. Matthey, F. Mauri, D. Mazza, A. J. Melgarejo, A. Menegolli, G. Meng, M. Messina, J. W. Mietelski, C. Montanari, S. Muraro, S. Navas-Concha, M. Nicoletto, J. Nowak, G. Nurzia, C. Osuna, S. Otwinowski, Q. Ouyang, O. Palamara, D. Pascoli, L. Periale, G. Piano Mortari, A. Piazzoli, P. Picchi, F. Pietropaolo, W. Pólchlopek, M. Prata, T. Rancati, A. Rappoldi, G. L. Raselli, J. Rico, E. Rondio, M. Rossella, A. Rubbia, C. Rubbia, P. Sala, R. Santorelli, D. Scannicchio, E. Segreto, Y. Seo, F. Sergiampietri, J. Sobczyk, N. Spinelli, J. Stepaniak, R. Sulej, M. Szeptycka, M. Szarska, M. Terrani, G. Trinchero, R. Velotta, S. Ventura, C. Vignoli, H. Wang, X. Wang, J. Woo, G. Xu, Z. Xu, X. Yang, A. Zalewska, J. Zalipska, C. Zhang, Q. Zhang, S. Zhen, and W. Zipper, "Design, construction and tests of the ICARUS T600 detector," *Nuclear Instruments and Methods in Physics Research Section A: Accelerators, Spectrometers, Detectors and Associated Equipment*, vol. 527, pp. 329–410, jul 2004.

[29] V. Chepel and H. Araújo, "Liquid noble gas detectors for low energy particle physics," *Journal of Instrumentation*, vol. 8, p. R04001, apr 2013.

[30] Y. Sakai, W. F. Schmidt, and A. Khrapak, "High- and low-mobility electrons in liquid neon," *Chemical Physics*, vol. 164, pp. 139–152, jul 1992.

[31] F. Aitken, Z.-L. Li, N. Bonifaci, A. Denat, and K. von Haeften, "Electron mobility in liquid and supercritical helium measured using corona discharges: a new semi-empirical model for cavity formation," *Physical Chemistry Chemical Physics*, vol. 13, pp. 719–724, dec 2010.

[32] L. S. Miller, S. Howe, and W. E. Spear, "Charge Transport in Solid and Liquid Ar, Kr, and Xe," *Physical Review*, vol. 166, p. 871, feb 1968.

[33] Y. Li, T. Tsang, C. Thorn, X. Qian, M. Diwan, J. Joshi, S. Kettell, W. Morse, T. Rao, J. Stewart, W. Tang, and B. Viren, "Measurement of longitudinal electron diffusion in liquid argon," *Nuclear Instruments and Methods in Physics Research Section A: Accelerators, Spectrometers, Detectors and Associated Equipment*, vol. 816, pp. 160–170, apr 2016.

[34] A. A. Machado and E. Segreto, "ARAPUCA a new device for liquid argon scintillation light detection," *Journal of Instrumentation*, vol. 11, no. 2, 2016.

[35] E. Segreto, A. A. Machado, L. Paulucci, F. Marinho, D. Galante, S. Guedes, A. Fauth, V. Teixeira, B. Gelli, M. R. Guzzo, W. Araujo, C. Ambrósio, M. Bissiano, and A. L. Filho, "Liquid argon test of the ARAPUCA device," *Journal of Instrumentation*, vol. 13, no. 8, pp. 1–17, 2018.

[36] A. A. Machado, E. Segreto, D. Warner, A. Fauth, B. Gelli, R. Máximo, A. Pissolatti, L. Paulucci, and F. Marinho, "The X-ARAPUCA: An improvement of the ARAPUCA device," *Journal of Instrumentation*, vol. 13, no. 4, pp. 1–9, 2018.

[37] C. Brizzolari, S. Brovelli, F. Bruni, P. Carniti, C. M. Cattadori, A. Falcone, C. Gotti, A. Machado, F. Meinardi, G. Pessina, E. Segreto, H. V. Souza, M. Spanu, F. Terranova, and M. Torti, "Enhancement of the X-Arapuca photon detection device for the DUNE experiment," apr 2021.

[38] SensL, "Introduction to SiPM An Introduction to the Silicon Photomultiplier Introduction to SiPM," *Technical note*, pp. 1–16, 2011.

[39] A. A. Ghassemi, K. Sato, K. K. E. Y. Ohashi, Y. Enomoto, and Y. Adachi, "MPPC," *Technical note*, 2021.

[40] M. I. Lopes and V. Chepel, "Liquid rare gas detectors: Recent developments and applications," *IEEE International Conference on Conduction and Breakdown in Dielectric Liquids, ICDL*, pp. 405–411, 2002.

[41] W. H. Lippincott, K. J. Coakley, D. Gastler, A. Hime, E. Kearns, D. N. McKinsey, J. A. Nikkel, and L. C. Stonehill, "Scintillation time dependence and pulse shape discrimination in liquid argon," *Physical Review C - Nuclear Physics*, vol. 78, no. 3, pp. 1–13, 2008.

[42] J. A. Nikkel, T. Gozani, C. Brown, J. Kwong, D. N. McKinsey, Y. Shin, S. Kane, C. Gary, and M. Firestone, "Liquefied Noble Gas (LNG) detectors for detection of nuclear materials," *Journal of Instrumentation*, vol. 7, no. 3, 2012.

[43] J. R. S. Kubota, M Hishida, M. Suzuki, S. Kubota, M. Hishida, M. Suzuki, and J. zhi Ruan, "Liquid and Solid Argon, Krypton and Xenon Scintillators," *Nuclear Instruments and Methods*, vol. 196, pp. 101–105, may 1982.

[44] S. Kubota, M. Hishida, and M. Suzuki, "Dynamical behavior of free electrons in the recombination process in liquid argon, krypton, and xenon," *PHYSICAL REVIEWS B*, vol. 20, no. 8, 1979.

[45] A. Hitachi, T. Doke, and A. Mozumder, "Luminescence quenching in liquid argon under charged-particle impact: Relative scintillation yield at different linear energy transfers," *Physical Review B*, vol. 46, pp. 11463–11470, nov 1992.

[46] R. Acciarri, M. Antonello, B. Baibussinov, M. Baldo-Ceolin, P. Benetti, F. Calaprice, E. Calligarich, M. Cambiaghi, N. Canci, F. Carbonara, F. Cavanna, S. Centro, A. G. Cocco, F. Di Pompeo, G. Fiorillo, C. Galbiati, V. Gallo, L. Grandi, G. Meng, I. Modena, C. Montanari, O. Palamara, L. Pandola, F. Pietropaolo, G. L. Raselli, M. Roncadelli, M. Rossella, C. Rubbia, E. Segreto, A. M. Szelc, F. Tortorici, S. Ventura, and C. Vignoli, "Effects of Nitrogen and Oxygen contamination in liquid Argon," *Nuclear Physics B - Proceedings Supplements*, vol. 197, no. 1, pp. 70–73, 2009.

[47] E. Segreto, "Properties of Liquid Argon Scintillation Light Emission," 2020.

[48] H. V. D. SOUZA, "ARAPUCA, LIGHT TRAPPING DEVICE FOR THE DUNE EXPERIMENT," 2021.

[49] H. V. Souza, E. Segreto, A. A. Machado, R. R. Sarmento, M. C. Q. Bazetto, L. Paulucci, F. Marinho, V. L. Pimentel, F. L. Demolin, G. de Souza, A. C. Fauth, and M. A. Ayala-Torres, "Liquid argon characterization of the X-ARAPUCA with alpha particles, gamma rays and cosmic muons," jun 2021.

[50] opto, "opto." https://www.opto.com.br/, 2021. [Online; accessed 25-Out-2021].

[51] ELJEN, "ELJEN Technology." https://eljentechnology.com/, 2021. [Online; accessed 25-Out-2021].

[52] Hamamatsu, "Hamamatsu." https://www.hamamatsu.com/jp/en/index.html, 2021. [Online; accessed 25-Out-2021].

[53] 3m, "Vikuiti Enhanced Specular Reflector (ESR)." https://www.3m.com/, 2021. [Online; accessed 25-Out-2021].

[54] Hensys, "Hensys." https://www.hensys.com.br/, 2021. [Online; accessed 25-Out-2021].

[55] S. Vinogradov, T. Vinogradova, V. Shubin, D. Shushakov, and K. Sitarsky, "Probability distribution and noise factor of solid state photomultiplier signals with cross-talk and afterpulsing," *IEEE Nuclear Science Symposium Conference Record*, pp. 1496–1500, 2009.

[56] R. Sarmento, E. Segreto, A. Machado, H. de Souza, B. Gelli, M. Guzzo, J. Nascimento, and G. Souza, "Test of X–ARAPUCA through Monte Carlo simulation in Brazil," *Revista dos Trabalhos de Iniciação Científica da UNICAMP 1–1 (2019)*, vol. 2, no. 2018, pp. 1–1, 2020.

[57] S. Pommé and B. Caro Marroyo, "Improved peak shape fitting in alpha spectra," *Applied Radiation and Isotopes*, vol. 96, pp. 148–153, feb 2015.

[58] R. Brun and F. Rademakers, "ROOT — An object oriented data analysis framework," *Nuclear Instruments and Methods in Physics Research Section A: Accelerators, Spectrometers, Detectors and Associated Equipment*, vol. 389, pp. 81–86, apr 1997.

[59] E. Segreto, A. Machado, A. Fauth, R. Ramos, H. de Souza, G. de Souza, V. Pimentel, M. Q. Bazetto, and M. Ayala-Torres, "First liquid argon test of the X-ARAPUCA," *Journal of Instrumentation*, vol. 15, pp. C05045–C05045, may 2020.

[60] S. W. Smith, *The Scientist and Engineer's Guide to Digital Signal Processing*, vol. 1 of *1*. San Diego, CA 92150-2407: California Technical Publishing, 2 ed., 1999.

[61] H. T. Van Dam, S. Seifert, R. Vinke, P. Dendooven, H. Löhner, F. J. Beekman, and D. R. Schaart, "Silicon photomultiplier response model," *IEEE Nuclear Science Symposium Conference Record*, no. October, pp. 2362–2364, 2009.

[62] S. A. Review, "NP-04 / ProtoDUNE-SP," tech. rep., 2020.

[63] S. Kubota, M. Hishida, S. Himi, J. Suzuki, and J. Ruan, "The suppression of the slow component in xenon-doped liquid argon scintillation," *Nuclear Inst. and Methods in Physics Research, A*, vol. 327, no. 1, pp. 71–74, 1993.

[64] C. G. Wahl, E. P. Bernard, W. H. Lippincott, J. A. Nikkel, Y. Shin, and D. N. McKinsey, "Pulse-shape discrimination and energy resolution of a liquid-argon scintillator with xenon doping," *Journal of Instrumentation*, vol. 9, pp. P06013–P06013, jun 2014.

[65] DUNE Collaboration, "The Single-Phase ProtoDUNE Technical Design Report," jun 2017.

[66] E. Segreto, "Evidence of delayed light emission of tetraphenyl-butadiene excited by liquid-argon scintillation light," *Physical Review C - Nuclear Physics*, vol. 91, no. 3, pp. 1–9, 2015.